M-ANOMALY ANALYSES AND THEIR IMPLICATIONS

FOR

THE ARCHITECTURE OF THE UPPER OCEANIC CRUST

A Dissertation

by

MASAKO TOMINAGA

Submitted to the Office of Graduate Studies of
Texas A&M University
in partial fulfillment of the requirements for the degree of

DOCTOR OF PHILOSOPHY

May 2009

Major Subject: Oceanography

M-ANOMALY ANALYSES AND THEIR IMPLICATIONS

FOR

THE ARCHITECTURE OF THE UPPER OCEANIC CRUST

A Dissertation

by

MASAKO TOMINAGA

Submitted to the Office of Graduate Studies of
Texas A&M University
in partial fulfillment of the requirements for the degree of

DOCTOR OF PHILOSOPHY

Approved by:

Chair of Committee,	William W. Sager
Committee Members,	Maurice A. Tivey
	Mitch W. Lyle
	Deborah J. Thomas
	P. Jeffrey Fox
Head of Department,	Piers Chapman

May 2009

Major Subject: Oceanography

ABSTRACT

M-Anomaly Analyses and Their Implications for the Architecture of the Upper Oceanic Crust. (May 2009)

Masako Tominaga, B.E., Waseda University; M.S., Texas A&M University

Chair of Advisory Committee: Dr. William W. Sager

My dissertation research consists of two themes: (a) the analysis of Middle Jurassic - Early Cretaceous marine magnetic anomalies (M-anomalies) in order to construct a comprehensive geomagnetic polarity timescale and (b) the investigation of the upper oceanic crustal architecture using downhole geophysical logs. These themes were chosen to better understand how remotely-sensed geophysical signals elucidate the formation and evolution of oceanic crust. This revised Pacific-wide MGPTS model shows significant improvement in its reliability, exhibits global applicability, and highlights changes in the paleo-Pacific spreading regime. By integrating Atlantic M-anomaly analyses with the new MGPTS model and reviewing previous seismic studies, we shed new light on the causes of a ubiquitously distributed 'Atlantic anomaly smooth zone' where little coherency among M5-M15 anomaly sequence is observed. For the second theme, I analyzed the architecture of 15 m.y. old superfast spreading East Pacific Rise crust drilled at Ocean Drilling Program Hole 1256D in the eastern Pacific. An intact upper oceanic crustal section was penetrated at this site to a depth of 1507 mbsf. *In situ* crustal architecture was mapped from resistivity imagery (electrofacies by Formation

MicroScanner®) combined with recovered cores and other logs. Highlights of this research are: (1) most of the extrusive section consists of massive flows and fragmented formations including breccias, which has important implications for the magnetic source layer and pathways of hydrothermal alteration; (2) the dike complex is composed of sheeted-dikes dipping away from the paleo-spreading axis consistent with submersible observations at other sites in the eastern Pacific; (3) the crustal construction processess from ridge axis to abyssal plain during 0-50 kyr time are consistent with previous seismic reflection studies based on the integration of our stratigraphy model with lava flow observations from the southern East Pacific Rise.

To Yayoi, Shozo, Yosuke, and Dish-ko Tominaga

ACKNOWLEDGEMENTS

I would like to thank my committee members and research collaborators who supported my dissertation work.

Special thanks to my supervisor, Dr. William W. Sager at the Department of Oceanography, Texas A&M, who trusted my career development in science, for all his help (particularly, his extreme patience for editing my bad penmanship).

I very much appreciate Dr. Maurice A. Tivey at Woods Hole Oceanographic Institution for his helpful suggestions in magnetic modeling.

I would like to thank to Dr. Saneatsu Saito at JAMSTEC/IFREE for his encouragement to sail on the IODP Expedition 305 and for his great support for Expeditions 309/312 logging data analyses and to Dr. Nobuhisa Eguchi at CDEX (formerly at IODP-MI Sapporo) for his mentorship.

Lastly, I would like to stress that I could not have gotten through these years at the graduate school without your company and cheering, so thank YOU very much Aya Sasahara, Joe Martino, Kazue Tsuchida, Amber Harris, Hiroko Kitajima, and Captain Aubrey Tominaga.

TABLE OF CONTENTS

CHAPTER Page

CHAPTER Page

LIST OF FIGURES

Page

LIST OF TABLES

CHAPTER I

INTRODUCTION

The marine magnetic record is a basis for understanding the nature of the geodynamo, the behavior of the Earth's geomagnetic field, and the regime of plate tectonics. The Vine-Matthews-Morley hypothesis [*Vine and Matthews*, 1963], in which the entire crust was assumed to be the magnetic source layer, first suggested that the magnetic source layer records changes in Earth's geomagnetic field as the crust accretes and moves away from the spreading axis. Marine magnetic anomaly analyses, based on this hypothesis, thus can augment other marine geophysics studies to aid in the interpretation of both regional and global tectonic and crustal construction processes with chronological information.

Sea surface marine magnetic anomalies generated by the spreading oceanic crust form the key data set in the foundation of the geomagnetic polarity reversal timescale (GPTS), which has been used to date much of the ocean basins. The C-anomaly (from Late Cretaceous to present, 84 – 0 Ma) GPTS model was constructed from a compilation of anomalies from the South Atlantic and Pacific, and is well accepted because of its robustness (i.e., it was compiled from many magnetic profiles). In contrast, the M-anomaly (from Middle Jurassic to Early Cretaceous, 160 - 120 Ma) GPTS model relies mainly on a small number of magnetic profiles from a small region, so this model is far less robust and its applicability to other regions could be questioned.

This dissertation follows the style of *Journal of Geophysical Research.*

The actual magnetic architecture of the crust, in which the magnetic anomalies have been preserved, is known to be complicated. Variations in lithologies [*Kent et al.*, 1978], heterogeneity and anisotropy in magnetic properties with depth [*Smith*, 1990], the style of crustal accretion [*Denham and Schouten*, 1979], age progression [*Tivey and Johnson*, 1987; *Johnson and Pariso*, 1993; *Zhou et al.*, 2001], and tectonic settings at fast- and slow-spreading ridges [e.g., *Hooft et al.*, 1996; *Cannat*, 1996; *Williams et al.*, 2005] are all thought to affect the *in situ* magnetic architecture. In its simplest form, however, the prime magnetic source layer is modeled in two dimensions as an infinitely-long profile, 0.5 -1.0 km thick extrusive (seismic layer 2A) layer with homogeneous magnetization and vertical polarity boundaries. In this model, polarity direction is determined in constructing a GPTS model and where the lateral dimensions are given by the amount of seafloor spreading [*Talwani and Heirtzler*, 1964]. Because this simple model has been successfully applied to a wide range of magnetic anomaly analyses, it is commonly accepted. However, the actual architecture of the upper oceanic crust and how it retains the magnetic field record is still somewhat uncertain.

In my research, I identified two major themes that will contribute to our knowledge of the origin and implication of the marine magnetic anomalies. One is the analyses of the M-anomalies that are observed from world's ocean basins, and the second is a detailed investigation of the *in situ* architecture of the intact (from late stage off-axis lava to gabbros) upper oceanic crust that has been explored previously mainly by seismic data. The aims and results on these themes are discussed in following chapters.

Chapter II discusses the construction of a robust compilation of the M-anomaly geomagnetic polarity time scale from a compilation of Pacific M-anomaly profiles. The discussion of the Pacific results was expanded to the global comparison of M-anomaly characters. The Atlantic and Indian M-anomalies were examined in detail. Results suggested that the Pacific compilation of the M-anomaly geomagnetic polarity time scale is representative as a global M-anomaly time scale model.

Chapter III discusses the origin of the Atlantic M-anomaly "smooth zone", for which changes in spreading rates was previously considered as the origin today. By examining geophysical data and new anomaly analyses, we emphasized that the origins of the "smooth zone" are changes in geomagnetic field strength and crustal structure due to changes in spreading regime.

Chapter IV investigated the architecture of the fast-spreading modern East Pacific Rise crust by constructing an igneous stratigraphy model at Ocean Drilling Program Hole 1256D crust using geophysical property wire-line logs. Resulting stratigraphy is imperative to better understand the seawater-rock interaction geochemistry and changes in physical properties at Site 1256 crust. This manuscript has been accepted by *Geochemistry Geophysics Geosystems* (*Tominaga, Teagle, Alt, and Umino*, Determination of the volcanostratigraphy of oceanic crust formed at super-fast spreading ridge: Electrofacies analyses of ODP/IODP Hole 1256D).

Chapter V synthesizes the construction history of the upper oceanic crust at the East Pacific Rise, which was previously suggested only from indirect method (e.g., seismic), based on the volcanostratigraphy from Chapter IV. The upper crust

construction rates suggested from this study confirmed the seismic prediction of the construction rates by *Hooft et al*. (1996).

Chapter VI provides summary and conclusion of studies mentioned above.

CHAPTER II

REVISED PACIFIC M-ANOMALY GEOMAGNETIC POLARITY TIME SCALE

OVERVIEW

The current M-anomaly geomagnetic polarity time scale (GPTS) is mainly based on the Hawaiian magnetic lineations in the Pacific Ocean. Previous M-anomaly GPTS studies have relied on a small number of magnetic profiles, which is not ideal because any one profile contains an uncertain amount of geologic "noise" that perturbs the magnetic field signal. Compiling a polarity sequence from a larger array of magnetic profiles is desirable to provide greater consistency and repeatability. In this article, we present a new compilation of the M-anomaly GPTS constructed from polarity models from magnetic profiles crossing the three lineation sets (Hawaiian, Japanese, and Phoenix) in the western Pacific. Polarity reversal boundaries were estimated with a combination of inverse and forward modeling of the magnetic profiles, and were established for each of the three Pacific lineation sets separately, to allow examination of variability among the different lineation sets, and then combined to give a composite time scale. Owing a paucity of reliable direct dates of the M-anomalies on ocean crust, the composite model has only two age calibration points; one at each end of the sequence. These two dates are 125.0 Ma for the base of M0r and 155.7 Ma for the base of M26r. Relative polarity block widths from the three lineation sets are similar, indicating a consistent Pacific-wide spreading regime. The new GPTS model shows

slightly different spacing of polarity blocks, as compared with previous GPTS, with less variation in block width. It appears that the greater irregularity in older models is mostly an artifact of modeling a small number of magnetic profiles. The greater averaging in polarity chron duration of our model gives a time scale that should be a superior foundation for Late Jurassic- Early Cretaceous chronologic studies.

INTRODUCTION

Marine magnetic anomalies are the foundation of the geomagnetic polarity time scale (GPTS) because they provide a nearly continuous record of polarity intervals in time. Indeed, the continuity and repeatability of marine magnetic profiles was a key factor in the acceptance of the theory of seafloor spreading, which linked these anomalies to the process of oceanic crust formation and geologic time [*Vine and Matthews*, 1963]. The underlying model is simple, yet it has proved effective for GPTS development: changes in geomagnetic polarity are globally synchronous and the magnetization of the oceanic crust is mainly recorded within a thin layer of uppermost oceanic crust and was acquired at any given time within a narrow region close to the ridge axis. With these assumptions, early GPTS models were formulated [*Heirtzler et al.*, 1968; *Larson and Pitman*, 1973] and subsequently improved by the analyses of greater numbers of magnetic profiles or the acquisition of better age constraints [e.g. *Cande and Kent*, 1992a; *Channell et al.*, 1995a]. Seafloor spreading anomaly polarity block models can often be tied to land magnetostratigraphy and geochronology to obtain polarity boundary ages [*Cande and Kent*, 1992a].

Current GPTS models based on seafloor spreading cover the period from present to Middle Jurassic [*Cande and Kent*, 1992a; *Channell et al.*, 1995a; *Gradstein et al*., 2005]. The marine magnetic anomalies are grouped into two sequences: one before and the other after the Cretaceous Normal Superchron. Anomalies of the Late Cretaceous-Cenozoic mixed polarity superchron (i.e., "C-anomalies") stretch from Late Cretaceous to present whereas those of the Jurassic-Cretaceous mixed polarity superchron (i.e., "M-anomalies") span from Middle Jurassic to Early Cretaceous. The currently accepted C-anomaly GPTS was constructed from magnetic profiles from the South Atlantic Ocean and a few profiles from other oceans [*Cande and Kent*, 1992a, 1995]. This GPTS is widely accepted because it was constructed from a large number (n= 5~9) of carefully selected magnetic profiles, it accounted for anomaly skewness (asymmetry) owing to paleolatitude and strike [*Schouten and Cande*, 1976; *Petronotis et al.*, 1992], and its age calibration is derived from a relatively large number (n = 9) of radiometric dates.

In contrast, current M-anomaly GPTS are not as well defined because they are based on a smaller number of magnetic profiles, and are primarily focused on the Hawaiian lineation set in the western Pacific Ocean [*Larson and Hilde*, 1975; *Cande et al.*, 1978; *Channell et al.*, 1995a]. Moreover, M-anomaly GPTS have been difficult to calibrate for age owing to the scarcity of age constraints. The *Larson and Hilde* (1975) GPTS was calibrated using nannofossil zones from basal sediments recovered from Deep Sea Drilling Project (DSDP) cores whereas the time scale by *Channell et al* (1995a) (hereafter CENT95) was calibrated indirectly with a radiometric age from MIT

Guyot in the western Pacific and biostratigraphy and magnetostratigraphy in terrestrial strata.

The reliability of the M-anomaly GPTS can be improved by analyzing a larger set of magnetic records from a wider region. In this study, we report a Pacific-wide M-anomaly model based on large numbers of carefully selected magnetic profiles from the three lineation sets on the Pacific plate. We constructed our GPTS only from Pacific anomalies because the record is longer and more continuous in this region and because seafloor spreading rates in the Pacific were high and the sediment blanket is thin, translating to better spatial and temporal resolution. We restrict our analysis to anomalies from M0 to M29 because pre-M29 anomalies have been investigated only in the Japanese lineation set and the correlations are uncertain due to low amplitude, short wavelength anomalies that have not been widely confirmed [e.g., *Sager et al.*, 1998; *Tominaga et al.*, 2008].

BACKGROUND

Distribution of M-anomalies

M-anomalies are identified in the oldest part of all three of the major ocean basins [e.g., *Klitgord and Schouten*, 1986; *Vogt et al.*, 1971; *Hays and Rabinowitz*, 1975; *Cooper et al.*, 1976; *Verhoef and Scholten*, 1983; *Roest et al.*, 1992; *Sager et al.*, 1992; *Ramana et al.*, 1994; *Rybakov et al.*, 2000; *Roeser et al.*, 2002; *Ramana et al.*, 2001; *Gurevich et al.*, 2006] (Fig. 1A). Most of these M-anomaly lineation groups do not show clear correlatability and repeatability in anomaly character due mainly to slow

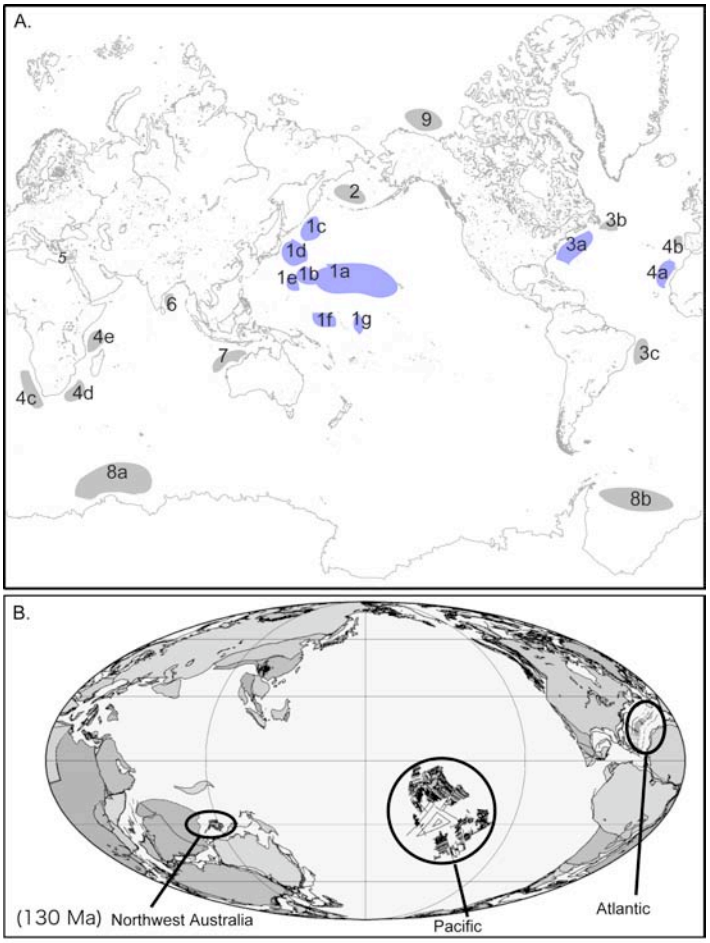

Figure 1. Study Areas. (A) Comprehensive map of M-anomalies in the world's ocean basins. Representative publications related to the regions are as follows: 1a~1g=Pacific lineation set (detailed in Figure 2); 2=Cooper et al. (1976); 3=Vogt and Johnson (1971); Vogt et al. (1971); 4a=Hayes and Rabinowitz (1975); Roest et al. (1992); 4b=Witmarsh et al. (2000); 4c=Milner et al. (1995), Gladczenko et al. (1997); 4d= Plessis and Simpson (1973); 4e=Rabinowitz et al. (1983); 5= Rybakov et al. (2000); 6= Ramana et al. (1994); 7= Larson (1975), Larson (1977), Robb et al. (2005); 8a=Ramana et al. (2001); 8b= Lawver et al. (1985); 9 = Gurevich et al. (2006). (B) The locations of three major M-anomaly groups superimposed on the 130 Ma Earth modified from The PLATES Project by University of Texas Institute for Geophysics.

spreading rates (10 ~ 40 km/m.y. half rate), thick sediments, and tectonic complications associated with fracture zones and continental break-up. The clearest extra-Pacific M-

anomaly sequences occur to the northwest of Australia [*Fullerton et al.*, 1989; *Sager et al.*, 1992; *Robb et al.*, 2005] where part of the sequence is found (M26-M16 and M10-M0), and in the north Atlantic [*Vogt et al.*, 1971] where the entire sequence is preserved.

The M-anomalies in northwest Australia and the north Atlantic have been extensively studied, but the clarity of anomaly character and continuity is less than those of the Pacific. Although the northwest Australia sequence shows similar anomaly characteristics to that of the Pacific anomalies, we cannot extract a complete, continuous sequence because these anomalies were recorded on two different ridges at different time periods with a time gap in between, and the area contains numerous fracture zones, ridge jumps, and major tectonic features including the Joey and Roo Rises and Exmouth Plateau [*Fullerton et al.*, 1989; *Robb et al.*, 2005].

Atlantic M-anomalies are observed in both the north and south Atlantic, but nearly complete M-anomaly sequences (M0-M25) occur only within the north Atlantic crust. Although the north Atlantic anomaly sequences appear continuous, the resolution is less than that of the Pacific because seafloor spreading was slow at times and sediment thickness is large near continental margins [*Vogt et al.*, 1971], so that we can only identify larger anomalies. This is especially a problem for the older M-anomalies (> M21), which have low amplitudes that decrease backward in time [*Cande et al.*, 1978]. Furthermore, even though *Sundvick and Larson* (1988) and *Schouten and Klitgord* (1982) mapped M5-M16 off North America from dense aeromagnetic data, these anomalies are attenuated in amplitude and we cannot clearly identify them from existing

sea-surface magnetic profiles. We believe that this "smooth" zone resulted from the effect of slow spreading on the structure of the crustal magnetic source layer.

The three Pacific M-anomaly lineation sets are the Hawaii, Japanese, and Phoenix (Fig. 2). They are isochrons of the expanding Mesozoic Pacific plate formed at the Pacific-Izanagi, Pacific-Farallon, and Pacific-Phoenix ridges, respectively [*Nakanishi et al.*, 1989, 1992]. The Hawaiian lineations have been used as the foundation of previous M-anomaly GPTS because they were the first identified complete lineation group and there are several subparallel, continuous magnetic survey lines that traverse the entire group [*Larson and Hilde*, 1975; *Nakanishi et al.*, 1989]. The younger portion of the Hawaiian M-anomaly set is located near the west end of the Hawaiian seamounts (Hawaii 1 in Figs. 2 and 3), and the older portion lies to the south of Shatsky Rise (Hawaii 2 in Figs. 2 and 3). The Japanese lineation set is subducting at the northwest edge of the Pacific plate in the Japan and Kuril Trenches, and into the Marianas Trench in the western Pacific (Fig. 2). The younger portion of the Japanese M-anomaly set is observed north of the Shatsky Rise (Japanese E and Japanese C in Figs. 2 and 3) [*Nakanishi et al.*, 1999] whereas the older portion of the Japanese M-anomalies is located in the east Mariana basin (Japanese W and S in Figs. 2 and 3) [*Handschumacher et al.*, 1988; *Nakanishi et al.*, 1989]. The younger portion of the Phoenix lineation set lies among many seamounts and fracture zones northeast of Ontong Java Plateau (Phoenix C in Figs. 2 and 3) and the older portion is located in the Nauru Basin (Phoenix N in Figs. 2 and 3). Although this area contains numerous tectonic complications, *Nakanishi et al.* (1992) identified almost the entire M-anomaly sequence in this group except for M0 and pre-M29 anomalies.

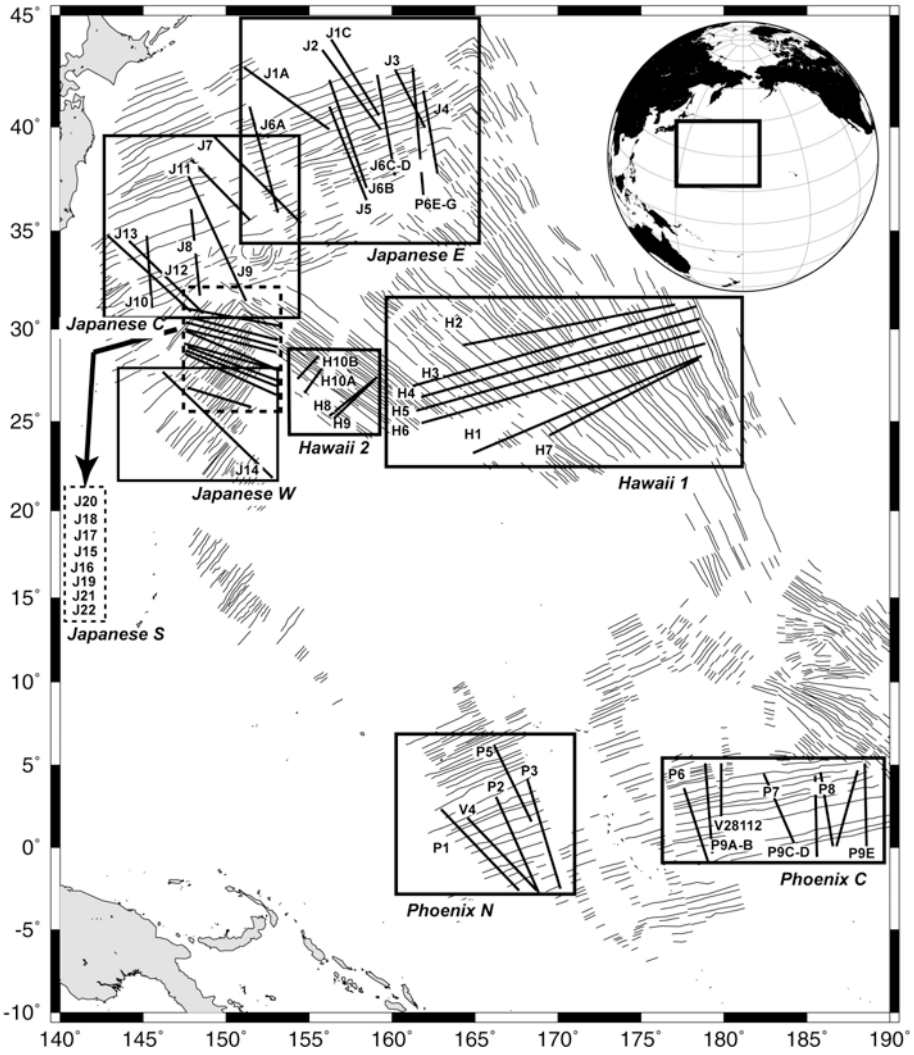

Figure 2. Locations of the Pacific M-anomaly lineation magnetic profiles. Each box shows the location of a group of profiles and the name of the lineation set is indicated. Track lines in each box correspond to those in the table on page 17 and the figures on pages 13-25. Magnetic lineations (gray lines) are from Nakanishi et al. (1992).

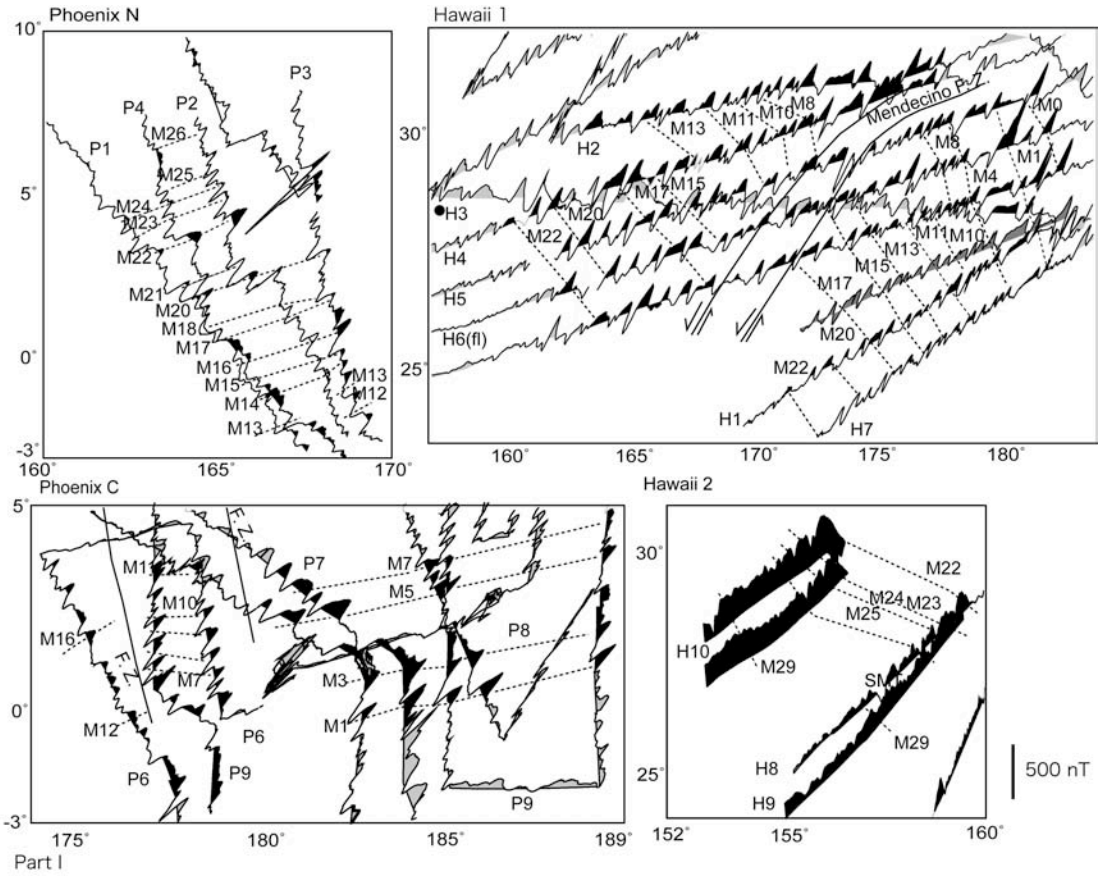

Figure 3. Correlation of anomalies on selected magnetic profiles. (Part I) Anomaly profiles with positive anomalies shaded black were used for anomaly correlations in this study, whereas gray-shaded anomalies were not. Dotted lines indicate correlated anomaly peaks and troughs (e.g., Nakanishi et al., 1992). The regions of Hawaii 1, 2, Phoenix N, and Phoenix C. The profile IDs correspond to "Index" in the table on page 17. The profiles H1, H3, H4, H5, and H6 in Hawaii 1 are used in Larson and Hilde (1975) and Channell et al., (1995a) GPTS model. The profiles P1, P2, and P4 in Phoenix N, P6, P8, and P9 in Phoenix C, and H8, H9, and H10 in Hawaii 2 are used for the anomaly correlations in Nakanishi et al. (1989, 1992).

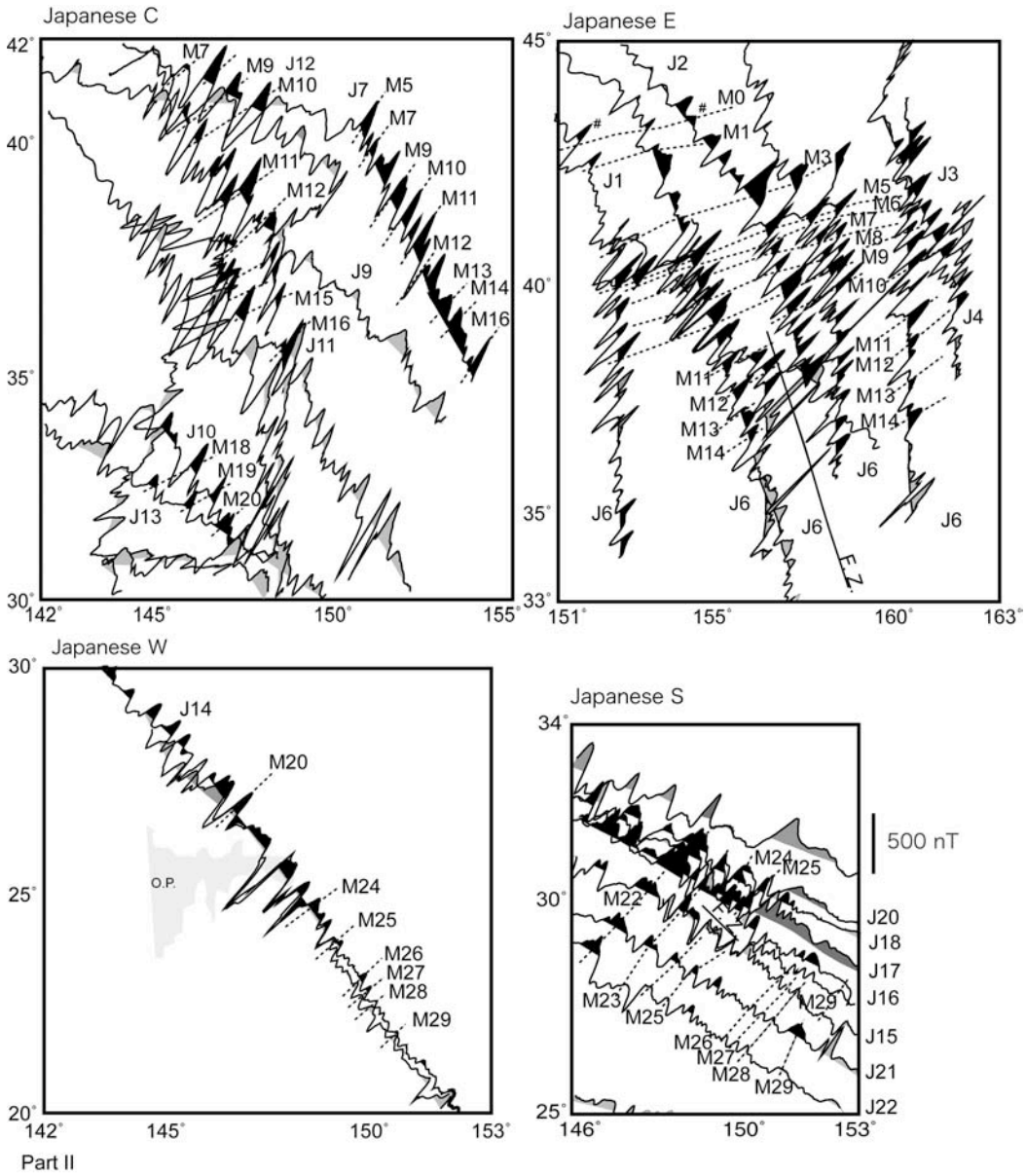

Figure 3. Continued. (Part II) Anomaly profiles with positive anomalies shaded black were used for anomaly correlations in this study, whereas gray-shaded anomalies were not. Dotted lines indicate correlated anomaly peaks and troughs (e.g., Nakanishi et al., 1992). The regions of Japanese C, E, W, and S in Figure 1. The profiles J7, J9, J10, J11, J12, and J13 in Japanese C, J1, J2, J3, and J6 in Japanese E, J14 in Japanese W, and J16, J17, and J18 in Japanese S are used for the anomaly correlations in Nakanishi et al. (1989, 1992). # symbols indicate newly identified occurrences of M0 in the Japanese lineations. F. Z. = Fracture Zone, O. P. = Ogasawara Plateau.

Development of the M-anomaly GPTS

The development of the M-anomaly GPTS occurred mainly with three studies, all of which used a small number of magnetic profiles covering a limited area. The Hawaiian M-anomaly model of *Larson and Hilde* (1975) was the foundation for most subsequent M-anomaly GPTS models. Their GPTS is a composite of 7 segments of magnetic anomaly profiles from the Hawaiian lineations (Fig. 3). In this GPTS, ages of polarity boundaries were determined using a constant spreading rate and biostratigraphic ages for basal sediments overlying the igneous crust from DSDP holes in the Pacific and Atlantic.

Cande et al. (1978) added anomalies M26 – M29 to the GPTS of *Larson and Hilde* (1975). Although they compared segments of 13 magnetic profiles from all three Pacific lineation sets, they used only 1 profile from the Japanese lineation set to construct the M26 – M29 GPTS. Polarity boundary ages were extrapolated from *Larson and Hilde* (1975) assuming a constant spreading rate.

Channell et al. (1995a) was the first major revision of the M-anomaly GPTS. They examined a total of 11 magnetic anomaly profiles from the three Pacific lineation sets to build polarity block models from M0 to M29 for each lineation set. Although they examined three calibration ages for the polarity sequence and modeled all three lineation sets, CENT95 is based only on one profile from the Hawaiian lineations. Age calibration for CENT95 is based on dates of 121.0 and 154.0 Ma for M0 and M25, respectively, with linearly interpolated polarity chron ages in between. The Hawaiian lineation sequence was deemed the "best" representation of the M-anomaly GPTS

because the interpolation of these anomalies most closely matched a third radiometric age, 137.0 Ma, for somewhere in between M15 and M16, taken from a radiometric age from land stratigraphy.

Another widely cited GPTS is the Geological Time Scale book series [*Harland et al.*, 1982; 1989; *Gradstein et al.*, 2005]. The most recent Geological Time Scale [*Gradstein et al.,* 2005; hereafter TS2004] is based on three separate reversal models: the surface magnetic anomaly-based sequence from Hawaiian lineation set for M0-M24 [*Larson and Hilde*, 1975], the aeromagnetic anomaly-based sequence from the Japanese lineation set for M25-M27n [*Handschmacher et al.*, 1988], and a deep-tow magnetic anomaly-based sequence from Japanese lineation set for M27r-M29 [*Sager et al.*, 1998]. TS2004 uses a revised age for M0 (125.0 Ma) based on a suggested new global stratotype for M0 within terrestrial magnetostratigraphy and biostratigraphy [*Channell et al.*, 2000].

DATA AND METHODS

Selection of Magnetic Profiles

We compiled a total of 87 sea-surface magnetic profile segments from the Hawaiian, Japanese, and Phoenix lineation sets in the Pacific using data from the National Geophysical Data Center (Fig. 3, Table 1), most of which were archived as anomaly values corrected to the International Geomagnetic Reference Field for various years. We chose only profiles with along-track bathymetry data and trends nearly perpendicular to previously-determined magnetic lineation strikes and excluded the parts

Table 1. Magnetic profiles and magnetization parameters

NGDC #	Cruise ID	Anomaly	Index	site lat	site lon	pole lat	pole lon	PI	PD	sli
Hawaii 1										
1030095	V2404	M0	H1A	27.5	179.0	49.8	327.1	-15.1	20.1	150
		M5	H1B	27.0	178.0	48.3	322.2	-15.9	23.1	150
		M11	H1C	26.0	176.0	53.0	334.0	-17.0	13.2	150
		M16	H1D	25.0	173.0	60.4	321.5	-1.6	14.9	150
3040053	POL7004	M0	H2A	32.0	176.0	49.8	327.1	-8.5	18.2	150
		M5	H2B	31.5	173.0	48.3	322.2	-11.0	20.0	150
		M11	H2C	31.0	169.0	53.0	334.0	-9.9	8.9	150
		M16	H2D	30.5	165.0	60.4	321.5	5.8	11.3	150
3040057	POL7201	M1	H3A	32.0	176.0	49.8	327.1	-8.5	18.2	150
		M5	H3B	31.0	173.0	48.3	322.2	-11.9	20.0	150
		M11	H3C	30.5	169.0	53.0	334.0	-10.9	9.0	150
		M16	H3D	28.5	164.5	60.4	321.5	1.7	11.1	150
		M0	H4A	31.5	179.0	49.8	327.1	-7.8	19.9	150
		M5	H4B	30.5	176.0	48.3	322.2	-11.1	21.8	150
		M16	H4C	28.5	169.0	60.4	321.5	3.4	13.2	150
		M0	H5A	30.5	179.5	49.8	327.1	-9.3	20.3	150
		M5	H5B	29.5	176.0	48.3	322.2	-12.9	21.9	150
		M16	H5C	28.0	169.0	60.4	321.5	2.4	13.2	150
		M0	H6A	29.0	179.5	49.8	327.1	-12.1	20.4	150
		M5	H6B	28.0	176.0	48.3	322.2	-15.5	21.9	150
		M11	H6C	27.5	173.0	53.0	334.0	-15.3	11.4	150
		M16	H6D	26.5	169.0	60.4	321.5	-0.5	13.2	150
15040233	TUNE09WT	M0	H7A	26.5	179.5	49.8	327.1	-16.5	20.5	150
		M5	H7B	26.0	178.0	48.3	322.2	-17.7	23.2	150
		M11	H7C	25.0	176.0	53.0	334.0	-18.8	13.2	150
		M16	H7D	24.5	176.0	53.0	334.0	-19.7	13.2	158
Hawaii 2										
1030193	V3212	M22	H8	27.0	157.5	61	357.4	-1.0	-9.5	150
1030243	V3612	M22	H9	25.5	157.5	61	357.4	-3.9	-9.5	150
8010069	77031705	M22	H10A	28.5	155.0	61	357.4	2.7	-10.6	150
		M22	H10B	29.0	155.0	61	357.4	3.6	-10.6	150
Japanese E										
1010094	C1405	M0	J1A	42.0	152.0	48.3	322.2	1.4	6.5	70
		M0	J1B	42.0	155.0	48.3	322.2	2.0	8.5	70
		M0	J1C	41.0	157.5	48.3	322.2	0.6	10.1	70
1030055	V2006	M0	J2A	41.0	156.0	49.8	327.1	2.3	5.7	70
		M5	J2B	38.5	156.0	49.8	327.1	-2.7	5.7	70
1030073	V2110	M0	J3A	43.0	160.0	48.3	322.2	5.2	11.7	70
		M5	J3B	40.0	160.0	49.8	327.1	1.0	8.3	70
3040053	POL7004	M10	J4	40.0	162.0	53.0	334.0	6.5	13.0	70
15050030	DSDP32GC	M5	J5A	39.5	155.0	48.3	322.2	-2.9	8.5	70
		M11	J5B	36.0	156.5	53.0	334.0	-1.9	1.5	70
9030026	SI932005	M5	J6A	38.5	152.0	48.3	322.2	-5.5	6.5	70
		M5	J6B	39.0	155.0	48.3	322.2	-3.9	8.5	70
		M5	J6C	40.5	158.5	48.3	322.2	-0.1	10.7	70
		M11	J6D	37.5	158.5	53.0	334.0	1.2	2.7	70
		M2	J6E	42.0	160.5	49.8	327.1	5.1	8.6	70
		M5	J6F	40.5	160.5	48.3	322.2	0.5	12.0	70
		M11	J6G	37.5	160.5	53.0	334.0	1.3	3.9	70
Japanese C										
1010074	C1219	M5	J7A	39.5	151.5	48.3	322.2	-3.6	6.2	70
		M11	J7B	36.5	153.0	53.0	334.0	-0.9	-0.6	70
1010167	C2004	M10	J8	31.0	145.0	53.0	334.0	3.6	10.6	70
1030193	V3212	M10	J9A	39.0	147.0	53.0	334.0	4.3	-4.2	70
		M16	J9B	33.0	150.0	60.4	321.5	3.6	10.6	70
1030195	V3214	M17	J10	38.0	153.0	60.4	321.5	17.3	5.7	70
1030211	V3311	M10	J11A	37.5	149.5	53.0	334.0	1.2	-2.7	70
		M10	J11B	34.5	149.0	53.0	334.0	-4.7	-3.0	70
15010075	ZTES04AR	M13	J12A	37.0	149.0	48.5	322.2	-8.5	4.5	70
		M16	J12B	37.5	149.5	60.4	321.5	15.9	-3.9	70
		M6	J12C	40.0	148.0	48.5	322.2	-2.7	3.8	70
15060015	JPYN04BD	M18	J13	32.0	145.0	60.4	321.5	4.8	1.7	70

Table 1. Continued.

NGDC #	Cruise ID	Anomaly	Index	site lat	site lon	pole lat	pole lon	PI	PD	sli
Japanese W										
15050089	DSDP89GC	M24	J14	23.5	150.0	61.0	357.4	-5.2	-12.9	70
Japanese S										
15050018	DSDP20GC	M22	J15	29.5	150.0	61.0	357.4	6.4	-12.9	70
15060015	JPYN04BD	M21	J16	30.0	150.0	61.0	357.4	7.4	-12.9	70
J2010012	GH7901	M21	J17	30.0	150.0	61.0	357.4	7.4	-12.9	70
J2010018	GH805-A	M21	J18	30.5	150.0	61.0	357.4	8.3	-12.9	70
J2010019	GH805B	M21	J19	29.5	150.0	61.0	357.4	6.4	-12.9	70
J2010022	GH771-C	M21	J20	31.0	150.0	61.0	357.4	9.3	-12.9	70
J2010023	GH824-A	M21	J21	27.5	150.0	61.0	357.4	2.5	-12.9	70
J2010024	GH824-B	M21	J22	26.5	150.0	61.0	357.4	0.5	-12.9	70
Phoenix N										
1010060	C1205	M11	P1A	-1.0	164.0	53.0	334.0	-56.7	7.4	260
		M16	P1B	1.0	164.0	53.0	334.0	-54.8	7.4	260
1030195	V3214	M14	P2A	0.0	167.5	60.4	321.5	-44.7	13.9	260
		M21	P2B	5.0	165.5	53.0	334.0	-50.4	8.1	260
15080020	NOVA1AHO	M10	P3A	0.0	169.0	60.4	321.5	-44.3	14.7	260
		M15	P3B	1.0	169.0	53.0	334.0	-54.8	7.4	260
1030215	V3401	M10	P4A	-0.5	166.0	60.4	321.5	-45.8	13.3	260
		M16	P4B	1.0	164.0	53.0	334.0	-54.8	7.4	260
		M22	P4C	4.5	164.0	61.0	357.4	-41.2	-7.0	260
		M22	P5	7.0	166.0	61.0	357.4	-38.1	-5.9	260
Phoenix C										
1030139	V2811	M5	P6A	1.0	176.0	48.3	322.2	-52.0	26.1	260
		M10	P6B	1.0	176.0	48.3	322.2	-52.0	26.1	260
		M12	P6C	2.0	178.5	53.0	334.0	-50.5	16.9	260
		M15	P6D	2.5	174.0	53.0	334.0	-51.3	14.0	260
15040185	RNDB13WT	M1	P7A	-1.0	182.0	49.8	327.1	-52.2	26.1	260
15040031	7TOW3BWT	M1	P8A	1.5	185.5	49.8	327.1	-48.0	27.3	260
		M5	P8B	4.0	184.5	48.3	322.2	-44.3	29.9	260
		M1	P8C	1.5	187.5	49.8	327.1	-46.9	28.3	260
1010079	C1304	M1	P9A	3.0	189.0	49.8	327.1	-44.4	28.7	260
		M5	P9B	1.0	189.0	48.3	322.2	-44.6	32.7	260
		M1	P9C	3.0	184.0	49.8	327.1	-45.2	30.3	260
		M5	P9D	2.5	184.8	48.3	322.2	-45.7	30.4	260
		M5	P9E	2.0	177.5	49.8	327.1	-51.3	22.6	260

NGDC # = NGDC archive number, ID = survey ID in NGDC archive; Anomaly = a chron number in which approximately an anomaly profile starts; Index = profile ID indicated on Figure 4 and segment ID indicated in Figure 5-9; site lat = latitude of a middle point on a given magnetic profile segment; site lon = longitude of a middle point on a given magnetic profile segment; pole lat = paleo pole latitude; pole lon =paleo pole longitude; PI = paleo inclination of a given profile; PD = paleo declination of a given profile; slin = track line azimuth from north toward young direction of the lienation.

of profiles that cross known fracture zones, ridge jumps that were suggested from previous anomaly correlations, or seamounts and other bathymetric features, because these disturb the magnetic anomaly patterns. These criteria give profiles that show

anomaly character most clearly, aiding in correlation, as well as providing the most repeatable set of anomalies.

Anomaly Correlations

The compiled profiles were grouped into five paleo-pole stages, M0-M4, M5-M10, M10N-M15, M15-M20, and M21-M29, for subsequent calculations (Figs. 4-9). This grouping was necessary because (1) the anomaly sequence spans >1000 km and few magnetic profiles cross it entirely and (2) plate movement during the ~30 Myr history of the M-anomalies changes the paleomagnetic parameters that determine anomaly skewness. These groups match the paleo-pole age groups in the paleomagnetic polar wander path of Larson and Sager (1992), allowing us to subdivide the sequence into approximately equal sections and to use those paleomagnetic poles to estimate paleomagnetic parameters. According to TS2004, the groups span ~ 7 Myr (M0-M4), ~ 4 Myr (M5-M10), ~ 5 Myr (M10N-M15), ~ 6 Myr (M15-M20), and ~ 8 Myr (M21-M29).

Each pole stage group includes 16 to 21 anomaly profiles, with data from all three lineation sets. To provide consistent distances, all of the profiles were projected perpendicular to the local strike of the magnetic lineations. We made preliminary correlations of peaks and troughs of the anomalies among those in each pole stage, referring to correlations from previous studies [*Larson and Hilde*, 1975; *Nakanishi et al.*, 1989, 1992, *Channell et al.*, 1995a] (Fig. 3).

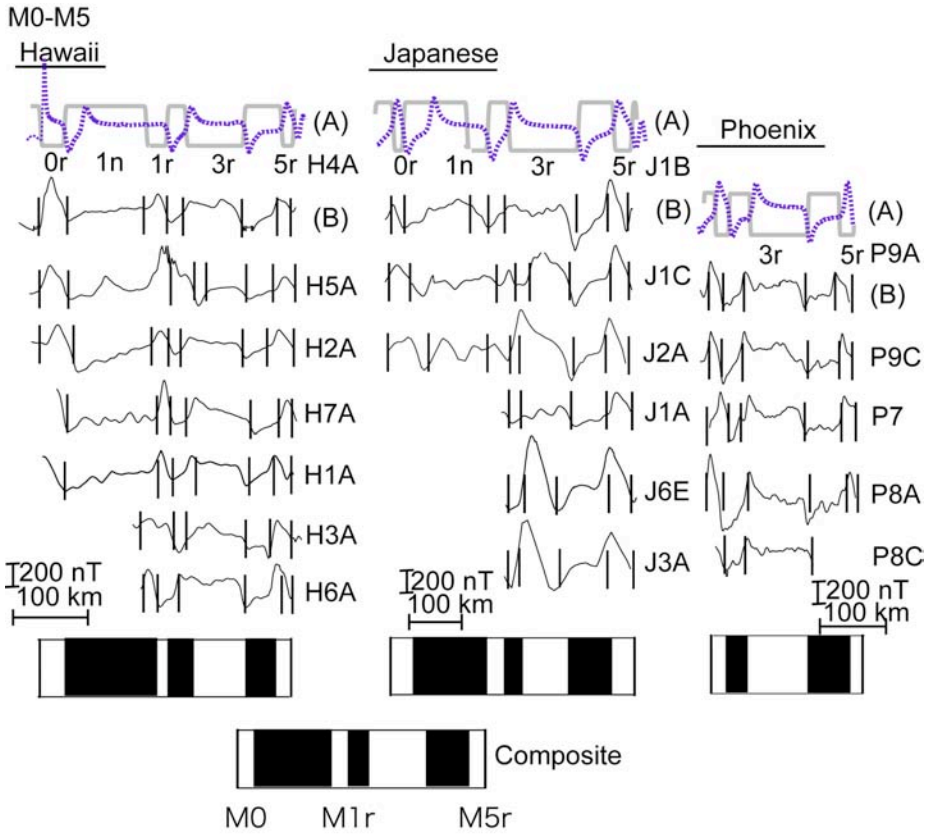

Figure 4. M0-M5n magnetic anomaly profiles and correlations. The profiles are projected with a common azimuth perpendicular to lineation trend. Each anomaly segment is annotated by a cruise identification. (H) = Hawaiian lineation set, (J) = Japanese lineation set, and (P) = Phoenix lineation set. Top pair of profiles in each column show an example profile and model. (A) shows the polarity model (gray) and calculated anomaly, whereas (B) shows the observed anomaly and the location of boundary of the first positive in each major chron with vertical bars. The black and white stripe bars below the profiles show the averaged model from each lineation set; and the one located at the bottom of the figure represents the composite block model from all three lineation sets (see the figures on pages 27 and 35).

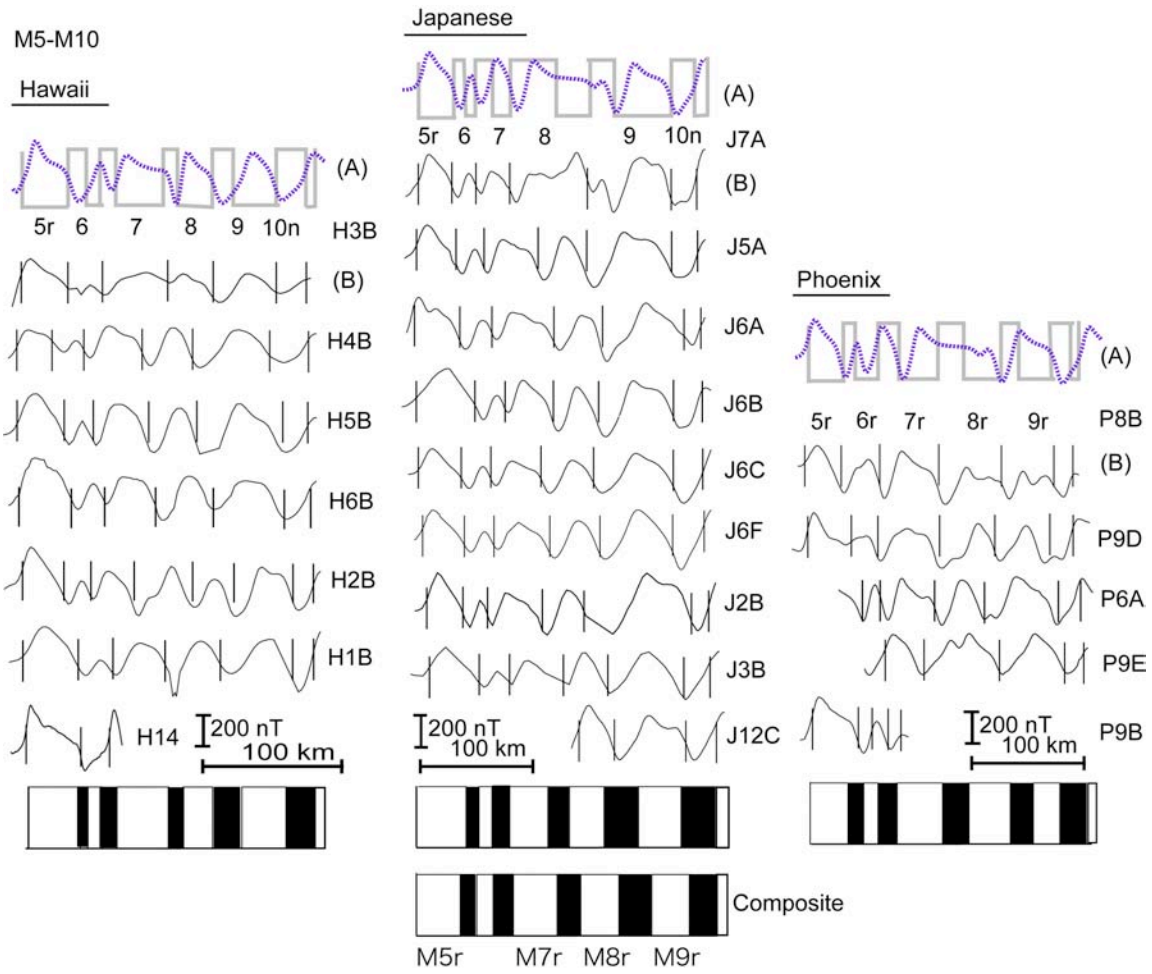

Figure 5. M5r-M10r magnetic anomaly profiles and correlations. Plot conventions as in Figure 4.

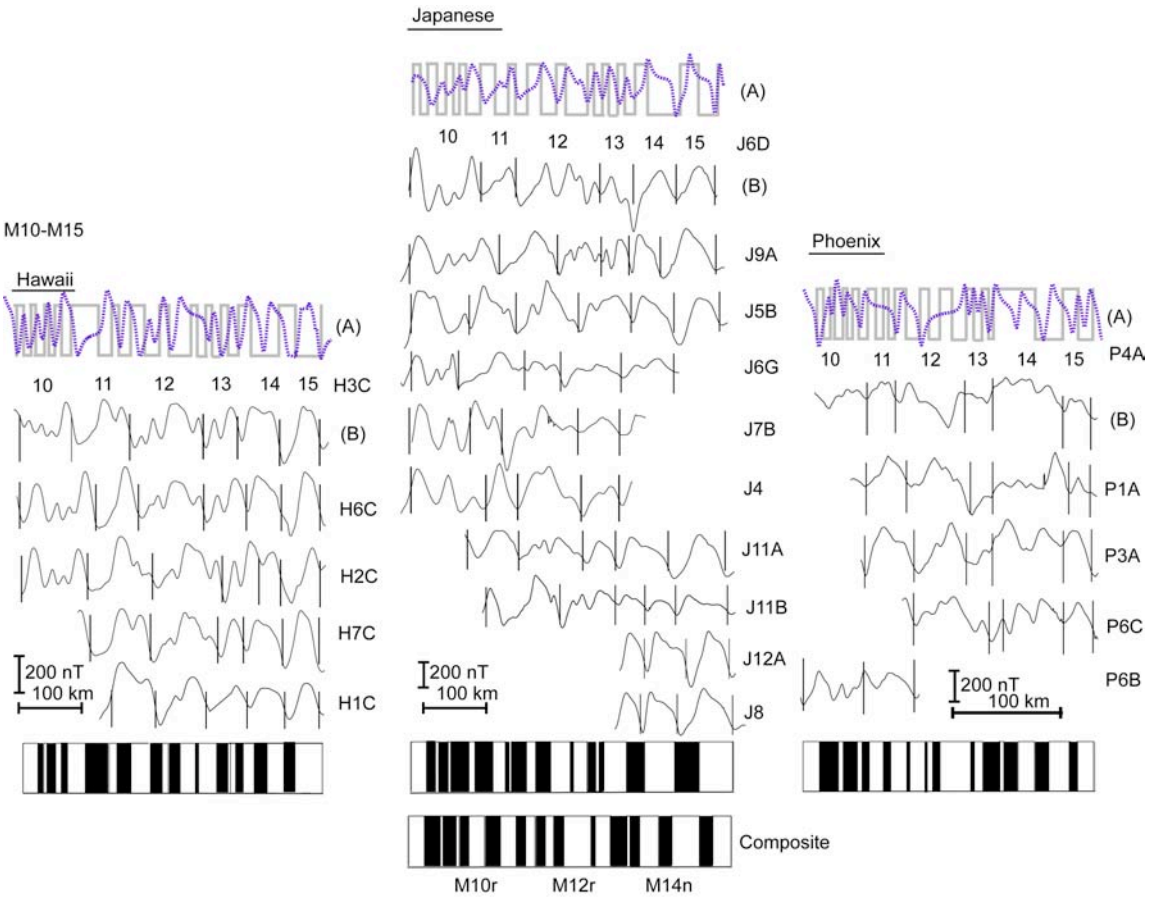

Figure 6. M10N-M15r magnetic anomaly profiles and correlations. Plot conventions as in Figure 4. Subchrons within M10, M11, M12, and M13 are magnified vertically and indicated with arrows in the inset boxes in Figure 9.

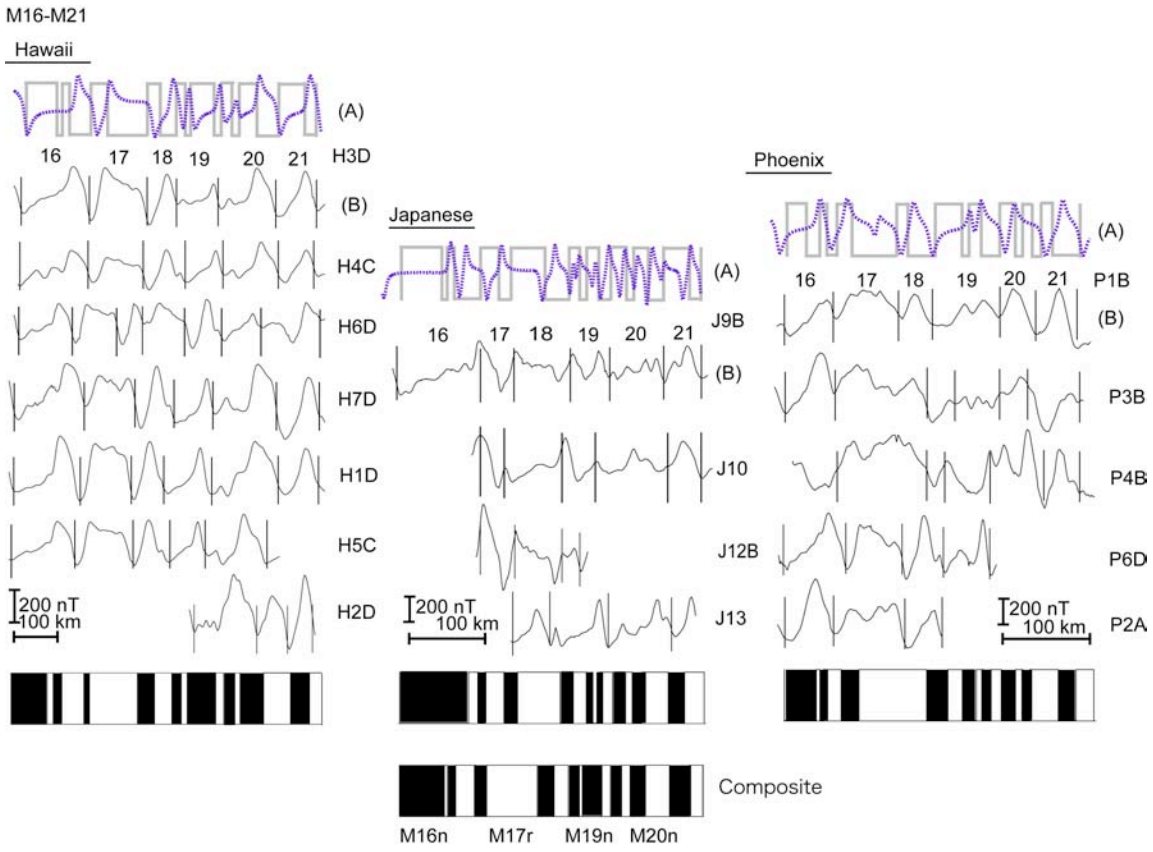

Figure 7. M16n-M20r magnetic anomaly profiles and correlations. Plot conventions as in Figure 4. Subchrons in M16, M19, and M20 are magnified vertically and indicated with arrows in the inset boxes in Figure 9.

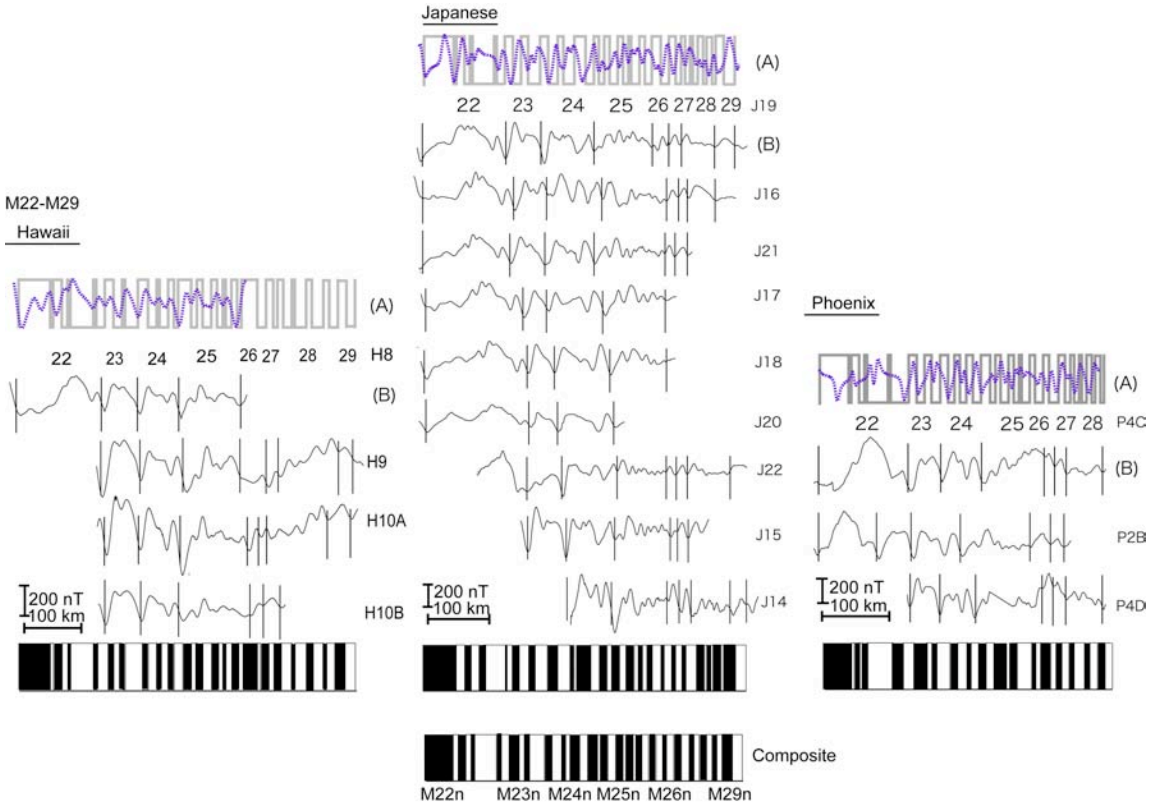

Figure 8. M21n-M29r magnetic anomaly profiles and correlations. Plot conventions as in Figure 4. Subchrons within M22, M23, M24, and M25 are magnified vertically and indicated with arrows in the inset boxes in Figure 9.

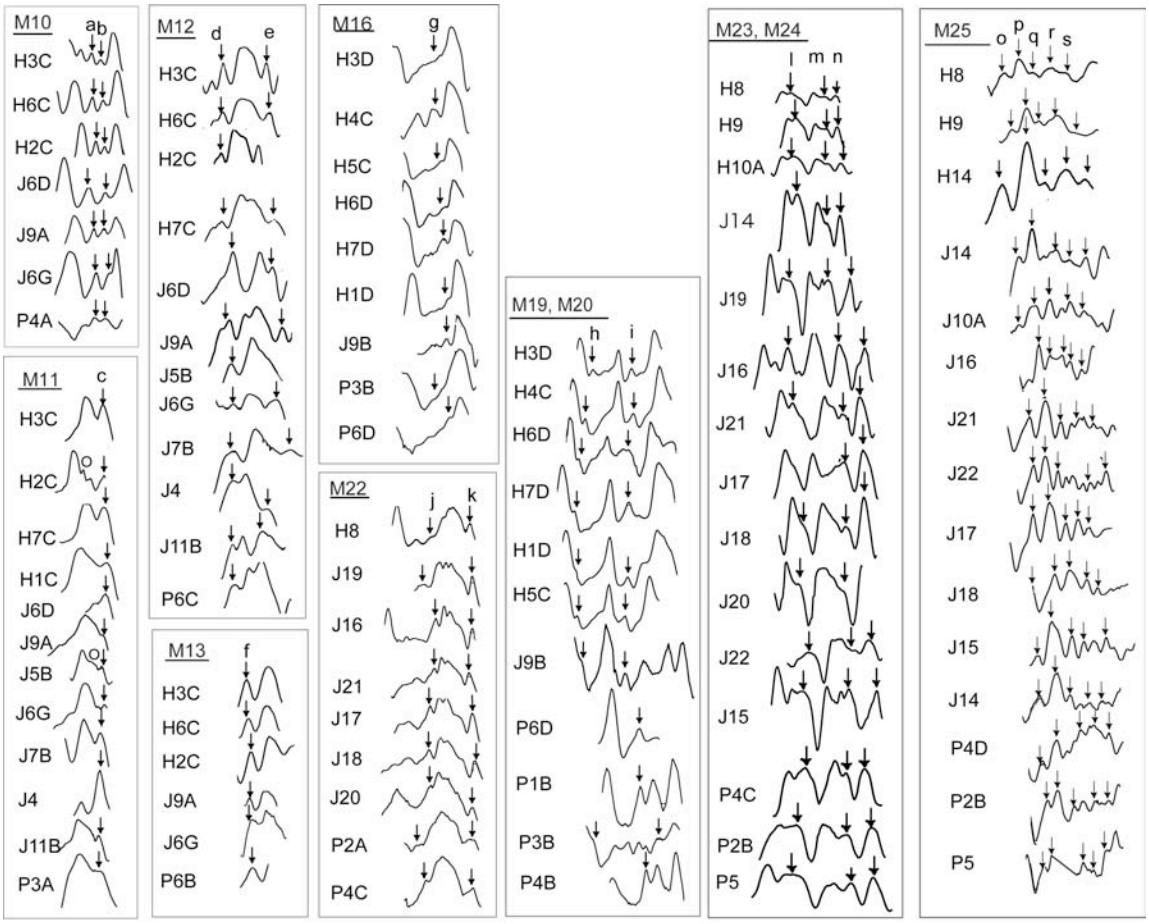

Figure 9. Subchrons identified within major chrons. The parental anomaly correlations are shown in Figures 3-7. The open circles indicate dropped subchrons. For reference, the arrows indicate subchron anomalies as follows: M10-a,-b are M10Nn.1 and M10Nn.2; M11-c is M11r; M12-d,-e are M12n and M12A; M13-f is M13n.1r; M16-g is M16n.1r; M19-h is M19n.1r; M20-i is M20n.1r; M22-j is M22n.2; M22-k is M22A; M23-l is M23r.2r; M24-m is M24r.2r; M24-n is M24Ar; and M25-o ~ -s are five subchrons identified in M25 (see Table 1).

Although our grouping of the anomalies in paleo-pole stages is similar to the method used in *Cande and Kent* (1992a), the purpose of this grouping is slightly different. *Cande and Kent* (1992a) grouped magnetic anomalies to calculate spreading rates and polarity durations using Euler poles. Their method was uniquely applicable to

studies in the south Atlantic because the oceanic lithosphere evolved nearly symmetrically on conjugate sides of the Mid-Atlantic Ridge and without significant changes in latitude [*Cande and Kent*, 1976; *Cande and Kent*, 1992a]. Determining spreading rates using Euler poles was not feasible in the Pacific because we could not model anomalies along a single flow line as did *Cande and Kent* (1992a). We used the age grouping to obtain paleo-inclination and -declination parameters for each paleo pole stage that are used to deskew the magnetic profiles in subsequent polarity block modeling.

Polarity Block Modeling

After the correlation and identification of anomalies, we sought to derive an accurate and robust M-anomaly polarity block model assuming that the correlated anomalies result from blocks of alternating polarity in the upper crust. To prepare for subsequent calculations, we re-sampled both along-track bathymetry and magnetic anomaly profiles into equally spaced data, which are needed for the Fourier transform in the inverse modeling.

A polarity block model was built for each profile taking an approach that used both inverse and forward modeling. Inverse modeling [*Parker and Huestis*, 1974] was used as an objective method to obtain a preliminary model of polarity zones. The inverse modeling outputs a magnetization distribution along the magnetic anomaly profile (Fig. 10 A1-A2) [Parker and Huestis, 1974]. We used this magnetization output to make a preliminary estimate of boundaries of opposite polarity blocks. These, in turn, were used

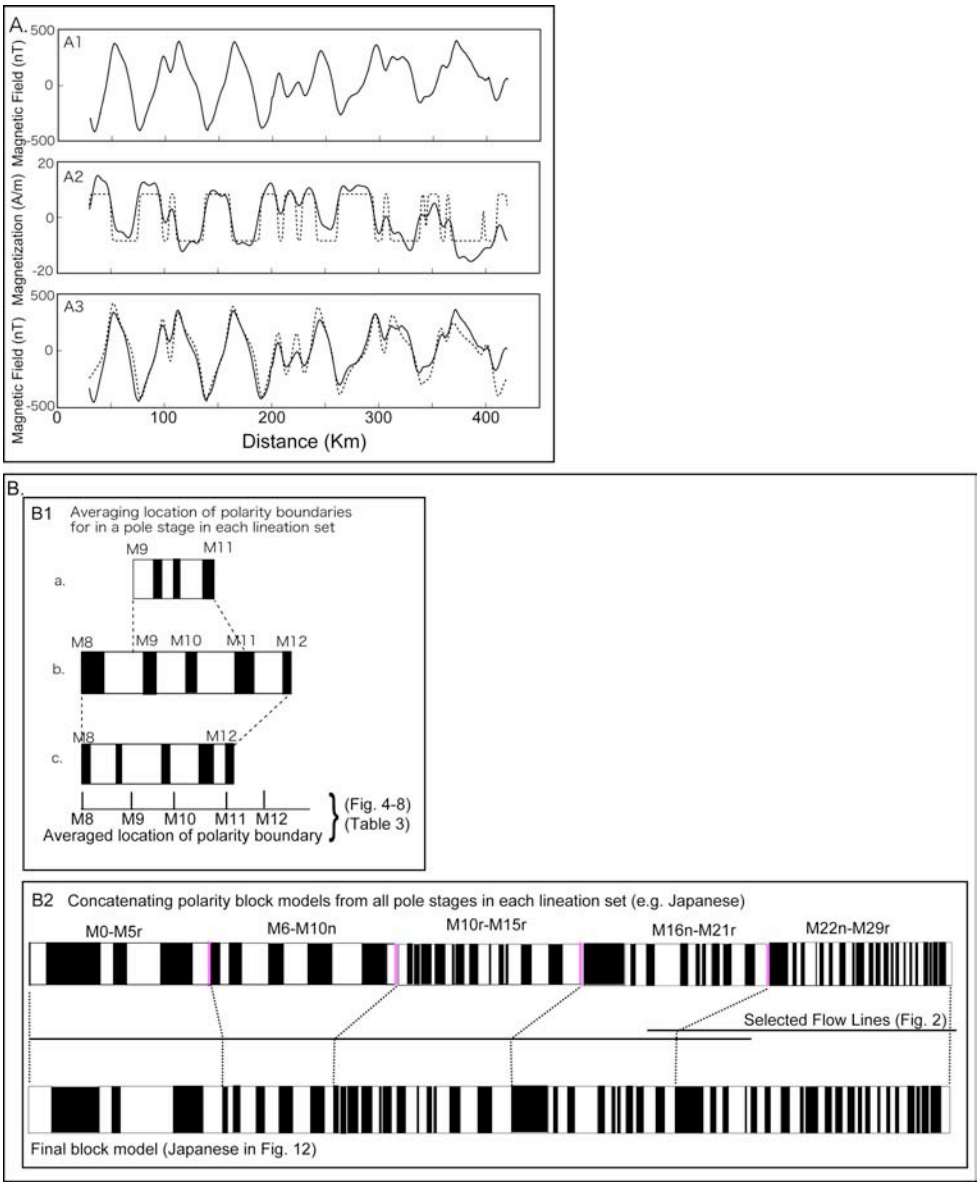

Figure 10. Sketch of the magnetic modeling process. (A1) Observed magnetic anomaly profile (P9, skewed). (A2) Solid line shows inverse results, magnetization values (deskewd). The apparent difference between this magnetization and the original magnetic profile is largely due to anomaly phase shift (skewness). Dotted line shows a polarity block model for the forward model. The polarity block model was Gaussian filtered at polarity boundaries to make finite width polarity transitions. (A3) Solid line shows observed magnetic anomaly profile (same as A) and dotted line shows calculated anomaly from the polarity block model created in A2. (B1-2) Normalization process is schematically described using profiles from the Japanese lineation set(see the details in text). (B1) Blocks a-c represent polarity block models for three individual magnetic profiles. These are normalized to the width of the age group in anomaly number. (B2) Polarity blocks for each age group are assembled to make a complete sequence for each lineation set using reference lines (see section 2.4).

as input for a forward modeling (Fig. 10 A2 - A3). For the forward model, the initial polarity block boundary locations were manually adjusted until the forward modeling resulted in a good match to the observed anomalies. The polarity block model in the forward modeling was Gaussian filtered (σ = 10 km) to give smooth, finite-width polarity transitions and a better match of calculated and observed anomalies (Fig. 10 A2). The reason that we did not use the inverse model to estimate final model polarity boundaries was because the boundary locations can be affected by anomaly base level (i.e., the annihilator function) and the frequency content of the anomalies. For the Pacific, this two-step method yields somewhat more reliable boundary locations as compared with simply using anomaly zero-crossings [c.f., *Cande and Kent*, 1992a]. This is because the M-anomaly sequences can contain gradual changes in amplitude [e.g., *Cande et al.*, 1978] that can offset the zero crossings.

For both inverse and forward modeling, the magnetic anomalies were bandpass filtered to retain wavelengths between of 3 and 140 km. An annihilator function of zero was used under the assumption of approximately equal normal and reversed polarity. To account for anomaly asymmetry (skewness) in inverse and forward modeling, model calculations used values for the remanent magnetization (paleo-inclination and -declination) inferred from the contemporaneous paleomagnetic pole (Fig. 10 A2, Table 1) from *Larson and Sager* (1992). We chose the *Larson and Sager* (1992) paleo-poles calculated without anomalous skewness because anomalous skewness apparently becomes negligible at spreading rates above 50 km/m.y. [*Dyment et al.*, 1994], which are typical of the Pacific plate spreading. To define the depth of the magnetic source layer,

we used along-track bathymetry data to give ocean depth. Sediment thickness was assumed to be constant at 0.3 km because this value is a crude average for the western Pacific [e.g., *Abrams et al.*, 1992], where sediments are usually thin and do not vary greatly in thickness (http://www.ngdc.noaa.gov/mgg/sedthick/sedthick.html). Errors in depth-to-source resulting from this assumption will be at most a few hundred meters and will have a negligible effect on the final model.

We did not use the downward continuation step used by *Cande and Kent* (1992a) to accentuate short wavelength features in the anomaly profiles. This procedure could result in misidentification of subchrons, particularly in the low amplitude M-anomaly profiles, because high wavenumbers, including noise, are enhanced [*Gubbins*, 2004]. In the Pacific, the anomalies are recorded by fast spreading crust, which retains many small anomalies, and downward continuation was unnecessary.

Normalization and Averaging of Polarity Blocks

The resulting polarity block model from each magnetic profile segment in a pole stage was normalized to the distance between the group end anomalies (e.g., M0-M5n etc.). The normalization process is critical for comparing and averaging profiles at different spreading rates because we could not restrict anomalies into single flow line and spreading rates were different on each of the ridges and often varied along ridge strike [e.g., *Nakanishi et al.*, 1989; 1992]. Normalization converts the location of polarity boundaries from distance (e.g., x_i for a particular boundary in kilometers) into a percentage of the period of a pole stage (e.g., p_i, where $0 \leq p_i \leq 1$) (Figs. 4-8).

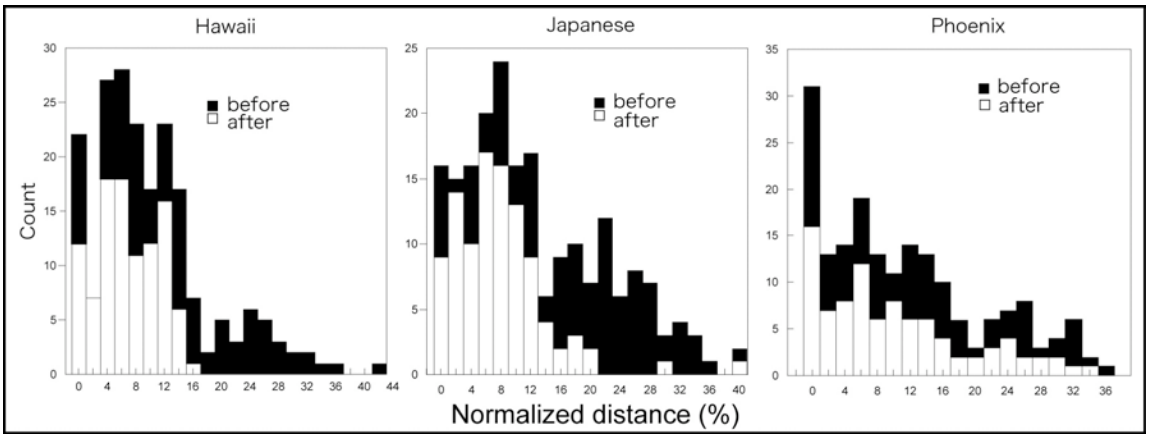

Figure 11. The distribution of standard deviations of individual polarity block boundaries. Black columns show deviations before and white columns show after the outlier rejection process was applied (see section 2.4). Vertical axis indicates the number of count. Horizontal axis indicates standard deviation of polarity block models expressed by normalized distance (%) relative to the anomaly age group. Standard deviations in kilometers are given in the table on page 45.

Normalized polarity boundary locations from each magnetic profile segment were averaged to build an average block model for each pole stage and for each lineation set. Each magnetic profile segment produced a series of polarity block boundaries each of which represents a magnetic reversal, $r_1, r_2, \ldots, r_n$, where n is the number of boundaries. With m observations of a particular boundary, its average position is $\bar{p}_i = \sum_{i=1,m} p_i \Big/ m$. Thus, the end result of the age group averaging is a series of average block boundary positions, $\bar{p}_1, \bar{p}_2, \ldots . \bar{p}_m$, where p is in normalized distance.

In averaging the block models from each magnetic profile segment in a pole stage, we refined the average of each polarity boundary location by excluding values outside the 95% confidence limits and recalculating the average and its standard deviation (Table 2). This step was used to prevent bias in the polarity boundary average

locations by outliers. The 95% confidence limits for each boundary location were calculated using a t-distribution because the number of samples is often small ($m < 30$), and the distribution may not be Gaussian, so using the t-value is potentially a more accurate method. As shown in Figure 11, the outlier rejection process significantly reduced the uncertainty of boundary locations in the Hawaiian and Japanese profiles. The uncertainty distribution was nearly unchanged for the Phoenix profiles, presumably because of greater variability in the polarity boundary locations of those lineations, probably resulting from tectonic complications [e.g., *Nakanishi et al.*, 1992].

Average models for each age group were concatenated to construct a combined model for the complete anomaly sequence. This was done first for each lineation set, so we could compare each lineation set with the others, and then those models were averaged for a Pacific-wide model. When combining the pole stage sequences into a total sequence model, we faced a scaling problem: normalizing the polarity boundaries removed their direct link to distance, and this made it problematic to concatenate the subsets in proper proportions. To determine the proportions, we matched the average polarity sequences to one or two reference magnetic profiles for each lineation set. In other words, at the four joints between the five anomaly age group subsets, the average polarity block model was tied to the distance of the appropriate anomaly on the reference profile. Profile POL7201 was the reference for the Hawaiian anomalies; DSDP32GC and JPYN04BD for the Japanese anomalies; and V3401 and C1304 for the Phoenix anomalies (see also Fig. 3, and Table 1). For these reference lines, we chose profiles that contain the most continuous and clear magnetic sequences. For both the Japanese and

Table 2. Standard deviations of polarity model chron boundaries (km)

Chron	Hawaii	N	Japanese	N	Phoenix	N	Composite	N
M0r	7.07	3	18.68	3			12.87	6
M1n	3.79	5	39.90	2			21.85	7
M1r	12.05	5	29.79	3	3.28	3	15.04	11
M3n	8.49	6	9.76	4	5.51	3	7.92	13
M3r	5.50	5	5.95	5	5.44	3	5.63	13
M5n	0.77	5	1.69	5	1.89	4	1.45	14
M5r	3.01	6	7.06	8	4.88	3	4.98	17
M6n	3.02	4	4.36	5	0.82	3	2.74	12
M6r	4.21	4	4.52	7	5.89	3	4.87	14
M7n	4.37	4	4.09	5	5.15	4	4.54	13
M7r	4.19	4	0.74	5	2.56	4	2.50	13
M8n	2.02	5	3.82	4	11.46	3	5.77	12
M8r	3.47	4	5.20	4	5.64	4	4.77	12
M9n	2.97	4	5.07	5	2.28	3	3.44	12
M9r	1.42	4	3.14	7	8.57	3	4.37	14
M10n	1.26	4	0.59	5	1.09	4	0.98	13
M10r	10.87	3	2.63	4	0.00	1	4.50	8
M10Nn.1n	8.94	3	6.23	4	0.00	1	5.06	8
M10Nn.1r	10.12	3	1.93	4	0.00	1	4.02	8
M10Nn.2n	11.02	3	8.91	3	0.00	1	6.64	7
M10Nn.2r	11.26	3	11.18	4	0.00	1	7.48	8
M10Nn.3n	11.08	3	5.97	4	0.00	1	5.68	8
M10Nr	10.63	3	4.48	4	0.00	1	5.04	8
M11n	11.27	4	9.70	4	8.49	2	9.82	10
M11r	13.81	3	9.28	4	18.88	2	13.99	9
M11An	8.50	3	7.92	3	17.65	2	11.36	8
M11Ar	2.39	2	5.07	3	11.66	2	6.37	7
M12n	12.86	3	10.91	5	3.71	2	9.16	10
M12r.1r	12.99	3	11.83	5	5.51	2	10.11	10
M12r.1n	2.32	3	11.40	5	0.99	2	4.91	10
M12r.2r	11.18	2	10.78	5	13.32	2	11.76	9
M12An	12.65	3	12.05	6	14.57	2	13.09	11
M12Ar	11.72	3	12.52	6	8.83	2	11.02	11
M13n.1n	11.81	3	8.79	6	13.13	3	11.24	12
M13n.1r	11.63	2	11.58	2	7.61	3	10.28	7
M13n.2n	8.26	2	8.86	3	6.25	4	7.79	9
M13r	6.64	4	6.87	7	5.20	4	6.24	15
M14n	10.29	3	10.54	5	9.82	4	10.22	12
M14r	14.09	4	6.08	7	9.38	4	9.85	15
M15n	3.48	3	5.70	6	4.50	4	4.56	13
M15r	0.68	4	0.91	4	7.74	4	3.11	12
M16n	6.15	6	0.00	1	10.44	3	5.53	10
M16n.1r	6.27	4	0.00	1	10.32	3	5.53	8
M16n.2n	5.90	5	0.00	1	8.47	3	4.79	9
M16r	4.61	5	0.00	1	4.70	3	3.10	9
M17n	11.30	5	4.06	3	6.48	5	7.28	13
M17r	14.62	4	1.70	3	12.70	5	9.67	12
M18n	16.08	4	2.36	4	9.98	5	9.47	13
M18r	14.83	4	3.25	4	5.24	5	7.77	13
M19n.1n	14.74	4	1.67	4	6.45	5	7.62	13
M19n.1r	4.59	4	2.01	3	4.69	3	3.76	10
M19n.2n	5.19	3	2.48	3	1.30	3	2.99	9
M19r	6.45	3	1.56	3	1.26	3	3.09	9

Table 2. Continued.

Chron	Hawaii	N	Japanese	N	Phoenix	N	Composite	N
M20n.1n	5.63	3	4.31	3	0.00	3	3.31	9
M20n.1r	8.63	3	10.08	3	0.00	1	6.23	7
M20n.2n	4.35	4	5.30	3	0.00	1	3.22	8
M20r	8.03	4	6.57	3	10.94	3	8.51	10
M21n	7.05	4	0.62	3	20.77	3	9.48	10
M21r	6.75	3	0.08	3	26.41	2	11.08	8
M22n.1n	0.00	1	13.95	6	29.28	2	14.41	9
M22n.1r	0.00	1	5.78	4	31.08	2	12.29	7
M22n.2n	0.00	1	1.28	4	28.22	2	9.83	7
M22n.2r	0.00	1	5.28	4	30.21	2	11.83	7
M22n.3n	0.00	1	7.32	4	24.62	2	10.65	7
M22r	0.00	1	15.32	4	28.77	2	14.69	7
M22An	0.00	1	13.21	6	33.60	2	15.61	9
M22Ar	0.01	1	10.00	5	26.24	2	12.08	8
M23n	6.39	4	8.95	7	21.37	3	12.24	14
M23r.1r	2.95	4	8.95	7	23.79	3	11.90	14
M23r.1n	3.28	4	7.49	7	22.81	3	11.19	14
M23r.2r	3.31	4	1.21	5	23.77	3	9.43	12
M24n	4.52	4	6.28	5	23.31	3	11.37	12
M24r.1r	0.59	4	8.35	5	20.02	3	9.65	12
M24r.1n	3.01	3	8.62	3	21.29	3	10.97	9
M24r.2r	3.60	3	8.62	6	16.17	3	9.46	12
M24An	5.26	3	1.99	6	16.35	3	7.87	12
M24Ar	5.93	4	8.50	5	15.07	3	9.84	12
M25n	7.29	4	9.39	6	13.55	3	10.08	13
M25r	5.89	4	12.95	5	12.76	3	10.54	12
M25An.1n	6.88	4	6.68	6	13.53	3	9.03	13
M25An.1r	7.25	4	12.03	5	11.96	3	10.41	12
M25An.2n	7.29	4	7.74	6	15.88	3	10.30	13
M25An.2r	9.61	4	9.52	5	14.71	3	11.28	12
M25An.3n	9.66	4	10.73	5	10.43	3	10.27	12
M25Ar	9.09	4	10.40	6	11.66	3	10.38	13
M25n5	11.84	4	10.53	7	10.44	3	10.94	14
M25r5	9.36	4	7.78	6	4.15	3	7.10	13
M26n	11.15	3	5.12	3	6.33	3	7.53	9
M26r	9.25	3	2.60	6	2.49	3	4.78	12
M27n	13.49	3	5.28	3	3.62	3	7.47	9
M27r	5.12	3	8.02	4	0.09	3	4.41	10
M28n	10.01	3	3.23	4	0.00	3	4.41	10
M28r	5.75	3	1.05	4	0.00	1	2.27	8
M28An	9.76	3	13.41	4			11.59	7
M28Ar	5.51	3	12.15	2			8.83	5
M28Bn	5.34	2	15.66	2			10.50	4
M28Br	3.69	2	14.05	2			8.87	4
M28Cn	3.83	2	18.97	2			11.40	4
M28Cr	0.15	2	18.51	2			9.33	4
M29n	9.37	2	20.52	2			14.94	4
M29r	12.38	2	19.56	2			15.97	4

N=number of polarity boundaries used. These standard deviations were referenced to distance along the following magnetic profiles: Hawaiian, NOAA4; Japanese, C1402/DSDP32; Phoenix, C1304/V3401.

Phoenix lineations, it was necessary to choose two magnetic profiles because there is no single profile that covers the entire M0 to M29 sequence in these lineation sets. We thus combined these two profiles into a composite reference line by adjusting one profile to the other using overlapped sequences around M10. The average polarity models span from M0 to M29 for the Hawaiian and Japanese lineation sets and from M1 to M28 for the Phoenix lineation set.

In addition to the Pacific-wide model, we also built a composite model using only the Hawaiian and Japanese lineation sets because of concern that the higher variability in Phoenix block model may adversely affect the composite model. As we describe in the discussion, however, this Phoenix-less model provided no significant improvement (Figs. 12 and 13).

Age Calibration for Time Scale Model

Few radiometric ages are available for the M-anomalies [e.g., *Pàlfy*, 2000] and most are not directly connected to marine magnetic anomalies [e.g., *Gradstein et al.*, 2005]. Because we could not find any reliable direct dates for the middle of the polarity sequence, we used only two age calibration points, one at each end of the anomaly sequence. For the old end, we used 155.7 ± 3.4 Ma for the base of the M26r, a date from rocks cored on M26 in the Argo Abyssal Plain [*Ludden*, 1992]. At the young end of the sequence, we used 125.0 Ma for the base of M0r because this is the accepted age and stratigraphic correlation (Barremian-Aptian stage boundary) [*Channell et al.*, 2000].

Given the poor age constraints for the M-anomalies, a simple linear interpolation is appropriate.

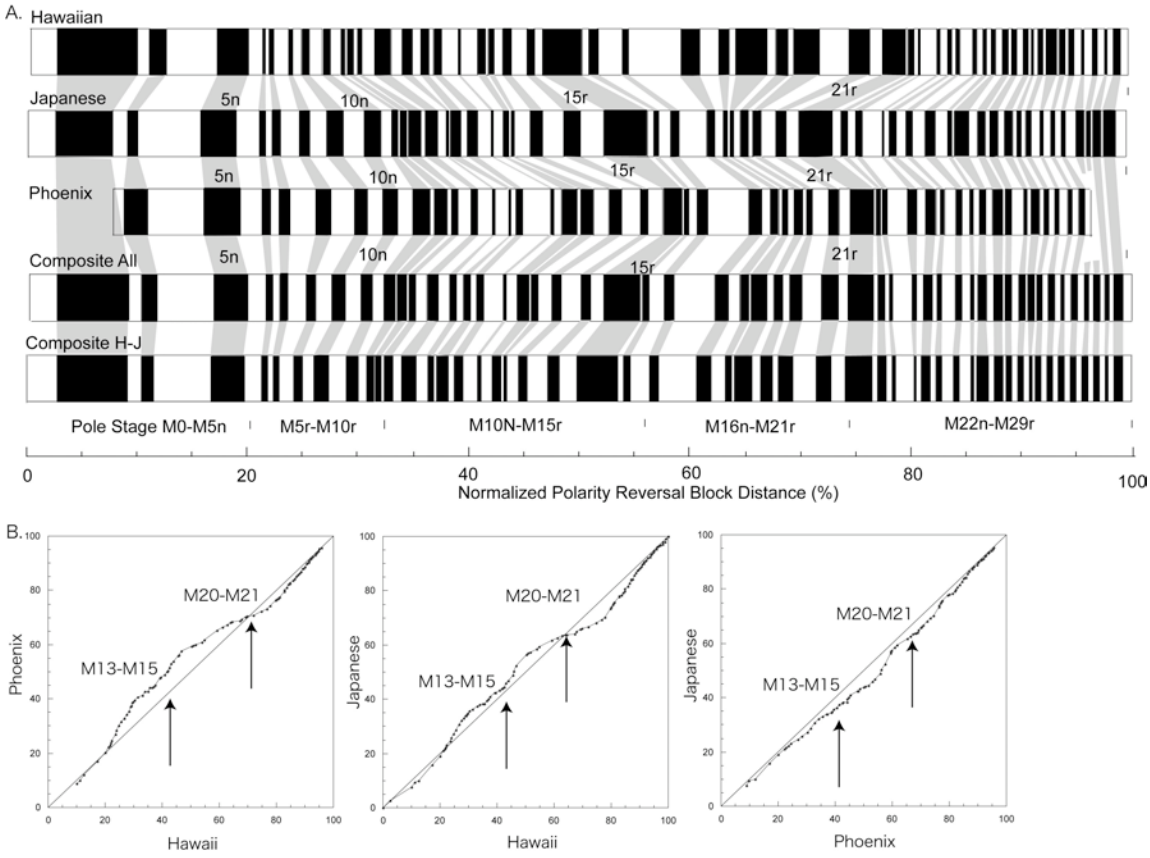

Figure 12. Polarity block models. (A) Block models plotted versus normalized distance. Top three sequences are from the Hawaiian, Japanese, and Phoenix lineation sets. Bottom two sequences are a composite model constructed from all three lineation set models and another that leaves out the Phoenix model. Positive polarity block correlations are indicated with gray shaded bands. The horizontal axis indicates the normalized distance. (B) Comparison of polarity block models between different lineation sets. Both vertical and horizontal axes indicate normalized distance (see Table 2). Straight diagonal lines represent (left) Phoenix vs. Hawaii, (middle) Japanese vs. Hawaii, and (right) Japanese vs. Phoenix. Arrows denote two periods of simultaneous changes in spreading regime (see text).

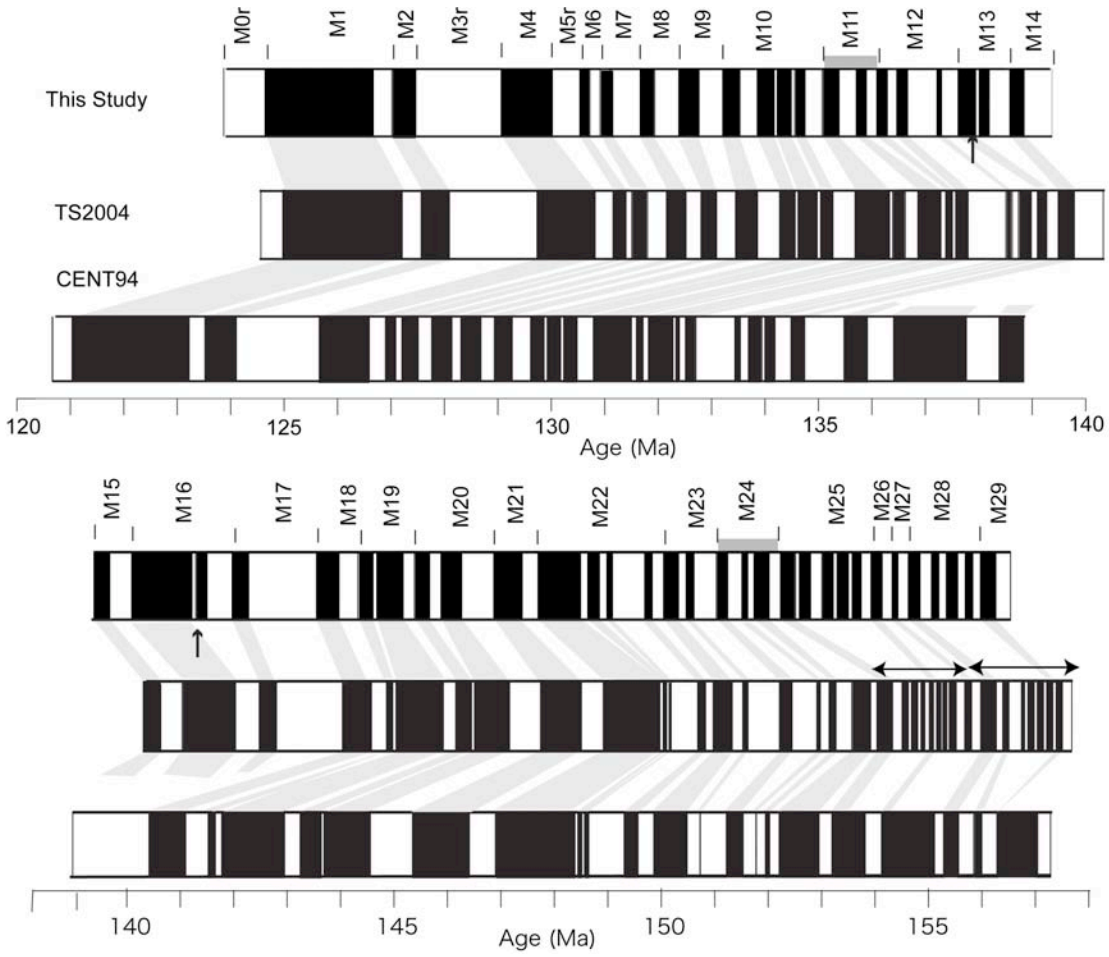

Figure 13. New M-anomaly GPTS and comparison with the CENT94 (*Channell et al.*, 1995a) and TS2004 (*Gradstein et al.*, 2005) models. "This study" is the composite model from all the three Pacific lineation sets. Arrows show correlations where two new subchrons were added (in M13 and M16). Gray bands next to the new GPTS show locations where subchrons were dropped (in M11 and M24). Note that CENT94 did not include subchrons in pre-M25 anomalies and had additional subchron in M24. Arrows over M25-M29 in TS2004 indicate that the TS2004 model used different reference block models for M0-M24 (*Larson and Hilde*, 1975), M25-M27 (*Handschumacher et al.*, 1988), and pre M28 (*Sager et al.*, 1998). In particular, the larger numbers of subchrons in M25-M29 are derived from aeromagnetic (Handschmacher et al., 1988) and deep-towed magnetic (*Sager et al.*, 1998) data.

RESULTS

Anomaly Correlations

Overall, correlations of anomalies within each lineation set were readily made because the anomalies are mostly coherent in shape and amplitude for the entire M0-M29 period. Anomaly shapes compared among lineation sets have only minor differences, which show up mainly in M19, M20, and M25-M29 (Figs. 7-9). This high repeatability among all three lineation sets implies that the modeled polarity chrons reflect Pacific-wide geomagnetic behavior. In this section, we describe differences in chron and subchron correlations (Figs. 4-8) with respect to previous studies. Most of the differences are in the interpretation of secondary anomalies.

We identified M0 in the Japanese lineation set (Figs. 3 and 4) on two profiles near the Japan Trench. Although M0 was not recognized in the Japanese lineation set by *Nakanishi et al.* (1989), on these two profiles it compares well to the expected shape and spacing with M0 in the Hawaiian lineation set. The broad normal and reverse polarity sequence of M1r and M3n are also characteristic features easily recognized in many profiles in this region (Fig. 4).

In previous studies of the M-anomalies, there has been no consistent treatment of small anomalies and the polarity subchrons that they represent in the reversal model. To be included in our model, any small anomaly had to pass the following criterion: it was identified on >50 % of the total available profiles and recognized in all three lineation sets. This indicates that the anomaly is a global, repeatable feature (Fig. 9). Because of this criterion, we dropped one subchron anomaly from the previous M11 and M24

correlations [*Channell et al.*, 1995a, 1995b] and we added one anomaly each to M13 and M16. Our correlations showed that one of the two previously-identified correlated anomalies in M11 is observed only on profiles POL7004 and DSDP32GC (H2C and J5B in Fig. 9), whereas the other is confirmed by the Pacific-wide correlation. This subchron was probably retained in previous studies because it occurs on profile POL7004, which is one of those used by *Larson and Hilde* (1975) to define the M-anomalies. A new subchron within M13n, not reported previously, is recognized in all three lineation sets and numbered M13n.1r (f in Figs. 6 and 9). We also propose a new subchron in M16n, which divides that normal polarity block and results in the pair, M16n.1r and M16n.2n (g in Fig. 9). This subchron has not been reported in previous studies but is observed in all three lineation sets. Although the anomaly amplitude is low for this subchron it is similar to previously identified low amplitude, short wavelength anomaly features in other chrons (e.g., M19.n1 and M20.n1, h and i in Fig. 9).

For the paleo-pole stage M21-M29, anomaly correlation is more difficult than in younger anomalies because anomaly amplitudes decrease with increasing age past M21. Although CENT95 contains four pairs of normal and reversed blocks within M24, our model retains only two pairs. The difference can be attributed to the fact that the extra subchrons in CENT95 are interpreted from short wavelength, small amplitude anomalies observed only on a few magnetic profiles in the Hawaiian lineation set. Anomalies prior to M24 become even more difficult to identify due to their low amplitudes. Nevertheless, we identified the previously-suggested anomalies prior to M24 on 15 magnetic profiles (Fig. 8), so we consider that the model sequence represents

correlatable anomaly features that are consistent with the chrons and subchrons suggested in previous studies [*Nakanishi et al.*, 1989, 1992]. Our model contains two more subchrons in M25, and one less in M28 compared to those in TS2004 [*Gradstein et al.*, 2005]. This difference occurs because TS2004 used different data sets: aeromagnetic data for M25-27 [*Handschumacher et al.*, 1988] and deep-towed magnetic data [*Sager et al.*, 1998] for pre-M28 anomalies.

Variability in Location of Polarity Boundaries

Average block models for each pole stage subset from all three lineation sets and their composite models are shown in Figures 4-8. Overall, the distribution of polarity boundaries amongst the three lineation sets for each pole stage is nearly identical, suggesting that there is little variability in the polarity reversal records in crust on different ridges with different spreading rates. Model variability is least in the sequence M0-M10 where polarity boundaries in stacked profiles line up closely (Figs. 4-5). The highest variability is observed in M11-M15 (Fig. 6). Although the repeatability of the anomaly sequence is convincing, there is a greater variability of anomaly widths and more instances where an anomaly on a given profile may not appear with its characteristic shape. Anomalies M16-M21 show somewhat greater regularity (Fig. 7), especially within the Hawaiian anomalies. Anomalies M21-M24 appear quite regular in all lineation sets (Figs. 7, 8). Despite the fact that the small amplitude M25 and older anomalies are more difficult to correlate, the modeled polarity boundaries show remarkably little variation (Fig. 8).

Variation in polarity block model spacing is apparent when composite models for each lineation set are compared (Fig. 12). Little difference is seen from M0-M7, but from M8-M15 the Japanese model is expanded relative to the Hawaiian blocks and the Phoenix blocks are expanded over the Japanese blocks. From M15-M21, the Hawaiian blocks catch up to and exceed the spacing of the Japanese blocks while the Phoenix blocks maintain a lead over the Japanese blocks. The differences disappear towards the end of the polarity model sequences as the models are all constrained to the end point of 100 %. These model differences are highlighted by plotting the polarity block distances (in percentage) for two of the three lineation set models one against the other (Fig. 12). The Japanese and Phoenix models produce the least deviation from a straight diagonal (a perfect match). In contrast, both the Phoenix and Japanese models give similar patterns relative to the Hawaiian model. Both the Phoenix and Japanese models plot above the diagonal (are more expanded) until about M21, when the reverse becomes true.

Modeling Uncertainty

Standard deviations of model polarity boundary locations were first determined in dimensionless percentage, but can be translated into kilometers with the mapping of the model onto the reference anomaly profiles. Polarity boundary location uncertainties show a range of 7-17 km (Table 2). To calculate the corresponding uncertainty in polarity zone widths, for comparison with the results of *Cande and Kent* (1992a), we use values from two, neighboring boundaries, defining the polarity zone widths: $w_i = p_{i+1} - p_i$ and $\sigma_i = \sqrt{\sigma_i^{\,2} + \sigma_{i+1}^{\,2}}$ where σ_i is the standard deviation of p_i.

The polarity zone width standard deviations range 2-22 km (average 11 km) for the Hawaiian model, 1- 49 km (12 km) for the Japanese model, and 2-44 km (17 km) for the Phoenix model. These values are similar to those from the model of *Cande and Kent* (1992), suggesting that the M-anomaly model has similar precision as that well-accepted C-anomaly time scale.

DISCUSSION

M-anomaly Correlation

In previous studies, polarity block modeling was carried out with a small number of profiles and focused on one lineation set. That restriction can be problematic because each individual magnetic profile contains perturbations caused by geologic "noise", i.e., irregularities in the anomaly spacing and shapes resulting from the crustal recording process. A more representative model can be derived by averaging many profiles covering a wide geographic area. Such a model is an improvement for two reasons: (1) averaging many, carefully selected anomaly profiles improves the fidelity of the composite because random variations in anomaly spacing, shapes, and amplitudes are averaged out and (2) wide geographic spacing insures that the magnetic changes are global in nature and errors caused by local tectonic factors, such as ridge jumps or spreading rate changes can be recognized and excluded. Our use of 87 magnetic anomaly profile segments, representing each of the five pole stages with an average of 18 profiles, is a factor two larger than the data set used for the widely accepted C-

anomaly GPTS [*Cande and Kent*, 1992a]. This redundancy has allowed us to determine the location of polarity boundaries with similar precision.

For the M0-M24 anomalies, a high degree of correlation among anomalies in each of the three lineation sets, as indicated by mostly small standard deviations in the location of polarity boundaries, is observed. Moreover, the general lack of significant differences between our model and previous versions implies that the recording of magnetic anomalies by the Pacific Plate ridges during this time period was remarkably regular.

The correlation of the M25-M29 anomalies in the sequence is a special problem. Although we can correlate anomalies consistent with previously defined M25-M29, there is larger variability, as compared to M0-M24 correlations, and the variability can be attributed to less accurate location of polarity boundaries within the closely spaced, short-wavelength, low-amplitude anomalies. With the difference in characteristics between the M25-M29 and M0-M24 correlatability, we ask two questions: (1) do M25-M29 anomalies represent actual polarity reversals? and (2) even if the M25-M29 anomalies are attributed to polarity reversals, do we extend the GPTS based on the correlation of these less consistent anomalies?

The M26-M29 anomalies were previously examined on 13 profiles in the three lineation sets across the western Pacific [*Cande et al.*, 1978]. The number and spacing of these small anomalies were found to be consistent, but the anomaly amplitudes are much smaller than that of younger anomalies (Figs. 4-8). *Cande et al.* (1978) discussed the origin of these anomalies and whether they represent actual short polarity reversals

or fluctuations of magnetic field intensity with uniform polarity. The conclusion was that the smooth increases in anomaly amplitude from M29 forward in time connects the M25-M29 anomalies with the M0-M24 anomalies and that they have common origin, which is polarity reversals [*Cande et al.*, 1978].

Because of uncertainty about the cause of such small anomalies [*Cande and Kent,* 1992b, *Sager et al.*, 1998], it is not certain that all of these anomalies result from polarity reversals. Terrestrial magnetostratigraphy shows many polarity chrons identified within M25-M29 [*Ogg and Gutowski*, 1995; *Pryzbyiski and Ogg*, 2007], but it is challenging to make a one-to-one correlation between polarity reversals in terrestrial magnetostratigraphy and marine magnetic anomalies of this age. At best, we can say that the magnetostratigraphic record shows alternating polarity chrons of the appropriate duration and age, so we suggest that this supports the interpretation of the M25-M29 anomalies as actual polarity reversals.

Although we accept the M25-M29 anomalies as polarity reversals, whether they should contribute to the extension of the GPTS is debatable. Anomalies M0-M29 have been widely identified and the correlations have been well accepted [*Cande et al.,* 1978; *Nakanishi et al.*, 1989; *Nakanishi et al*., 1992; *Channell et al.*, 1995a]. However, because of the small anomaly amplitudes, some anomalies may be geomagnetic field intensity fluctuations rather than reversals [e.g., *Bowles et al.*, 2003]. Furthermore, owing to the short wavelengths and less distinctive nature of individual anomalies, it is possible that we can miscorrelate some of the anomalies in the M25-M29 period. In this portion of the sequence, the GPTS is not as well founded, and thus should be interpreted

and used with some caution. To improve correlations, higher resolution data, such as deep-tow magnetic profiles from a wide geographic area would be useful.

Identification of Subchrons (Short Duration Reversals)

In constructing a GPTS model, the meaning of small anomalies has been in debate because it is difficult to determine whether those small anomalies represent reversals or not [e.g., *Cande and Kent*, 1992b; *Sager et al.*, 1998; *Tominaga et al.*, 2008]. *Cande and Kent* (1992a) excluded anomalies with durations of <30 kyr, arguing that these short anomalies are more likely to result from geomagnetic field intensity fluctuations than polarity reversals. However, this value is arbitrary, and there is no reliable duration cut-off that we can utilize.

In this study, nearly 60% of the subchrons in our GPTS have a duration >0.2 Ma. Only a few subchrons (M10r1, M10r2, M12.n3), identified in both previous studies and magnetostratigraphy, have durations of < 0.1 Ma, and the rest of the subchrons span 0.1 – 0.2 Ma. These durations are about three orders of magnitude longer than the cut-off value suggested in *Cande and Kent* (1992a). For those two 'excursions' suggested in *Speranza et al.* (2005), we include both in our GPTS because they meet our conservative acceptance criteria. One is included for the first time (M16n.1r) and the other was suggested in previous GPTS (M20n.1r). The durations of M16n.1r and M20n.1n are 0.2 and 0.1 Ma, respectively (Table 3). We observe that the anomalies defining these subchrons are little different from other observed correlatable, small anomalies that have been interpreted as reversals.

Table 3. Widths of modeled polarity chrons (normalized)

Chron	Hawaii	Japanese	Phoenix	Comp.	Age	#
M0r R	0.00	0.00		0.00	124.14	1
M1n N	2.49	2.61		2.54	125.00	2
M1r	9.89	7.71	0.00	8.86	127.15	3
M3n	11.08	9.25	1.23	10.12	127.57	4
M3r	12.47	9.98	3.54	11.52	128.05	5
M5n	17.15	15.84	9.34	16.67	129.80	6
M5r	19.98	19.05	13.06	19.75	130.84	7
M6n	21.22	21.06	15.33	21.47	131.42	8
M6r	21.54	21.63	16.08	21.98	131.60	9
M7n	21.90	22.26	17.03	22.58	131.80	10
M7r	22.31	23.01	18.12	23.27	132.03	11
M8n	23.54	24.69	20.80	25.01	132.62	12
M8r	23.96	25.70	22.40	25.93	132.94	13
M9n	24.78	27.15	24.68	27.33	133.41	14
M9r	25.54	28.76	26.18	28.54	133.82	15
M10n	26.65	30.75	27.72	29.99	134.31	16
M10r	27.46	32.20	29.28	31.17	134.72	17
M10Nn.1n	28.29	33.17	30.75	32.20	135.06	18
M10Nn.1r	28.83	33.82	32.48	33.10	135.37	19
M10Nn.2n	29.05	33.96	32.89	33.34	135.45	20
M10Nn.2r	29.55	34.57	34.32	34.12	135.72	21
M10Nn.3n	29.84	34.78	34.73	34.41	135.81	22
M10Nr	30.36	35.75	35.31	35.06	136.03	23
M11n	31.37	36.20	36.65	35.95	136.34	24
M11r	32.99	37.32	37.41	37.10	136.72	25
M11An	33.96	38.17	38.92	38.15	137.08	26
M11Ar	34.91	38.44	39.04	38.60	137.24	27
M12n1	35.66	38.45	40.65	39.35	137.49	28
M12r.1r	36.44	39.52	40.71	39.97	137.70	29
M12r.1n	36.86	40.11	41.22	40.45	137.86	30
M12r.23	37.64	40.95	41.87	41.18	138.11	31
M12An	39.08	42.36	44.87	43.00	138.73	32
M12Ar	39.36	42.43	45.08	43.18	138.79	33
M13n.1n	40.83	43.26	46.00	44.24	139.15	34
M13n.1r	41.77	44.00	47.56	45.26	139.49	35
M13n.2n	41.84	44.05	47.94	45.41	139.54	36
M13r	42.41	44.31	49.27	46.08	139.77	37
M14n	43.09	45.85	50.84	47.25	140.17	38
M14r	43.79	46.84	51.96	48.13	140.47	39
M15n	45.47	48.80	54.12	49.96	141.09	40
M15r	45.91	50.39	54.61	50.75	141.35	41
M16n.1n	46.77	52.48	56.19	52.15	141.83	42
M16n.1r	50.41	56.46	58.30	55.29	142.90	43
M16n.2n	50.89	56.98	58.44	55.66	143.02	44
M16r	51.80	57.37	58.75	56.20	143.20	45
M17n	54.02	58.62	59.87	57.70	143.72	46
M17r	54.67	59.34	60.87	58.45	143.97	47
M18n	59.28	61.83	65.10	62.10	145.21	48
M18r	61.02	62.57	66.30	63.30	145.61	49
M19n.1n	62.72	63.44	67.22	64.45	146.00	50
M19n.1r	63.80	63.69	68.18	65.20	146.26	51
M19n.2n	64.37	63.84	68.52	65.54	146.37	52

Table 3. Continued.

Chron	Hawaii	Japanese	Phoenix	Comp.	Age	#
M19r	67.22	64.19	69.10	66.85	146.82	53
M20n.1n	67.88	64.89	69.67	67.46	147.03	54
M20n.1r	69.07	65.71	70.60	68.41	147.35	55
M20n.2n	69.71	66.13	70.92	68.87	147.50	56
M20r	72.05	66.59	71.52	70.03	147.90	57
M21n	74.65	68.14	73.18	71.92	148.54	58
M21r	76.54	69.20	74.21	73.22	148.98	59
M22n.1n	77.80	70.30	75.45	74.37	149.37	60
M22n.1r	79.74	73.27	77.77	76.65	150.14	61
M22n.2n	79.96	74.11	77.95	77.04	150.27	62
M22n.2r	80.67	74.74	78.54	77.66	150.49	63
M22n.3n	80.88	75.50	78.79	78.04	150.61	64
M22r	81.11	75.74	79.23	78.32	150.71	65
M22An	82.72	77.94	81.32	80.18	151.34	66
M22Ar	82.85	77.99	82.14	80.48	151.44	67
M23n	83.54	78.50	83.12	81.17	151.68	68
M23r.1r	84.09	79.27	84.32	81.96	151.94	69
M23r.1n	84.61	79.93	84.68	82.45	152.11	70
M23r.2r	84.80	80.65	85.06	82.84	152.24	71
M24n	85.96	81.70	86.25	83.93	152.61	72
M24r.1r	86.35	82.62	86.97	84.56	152.83	73
M24r.1n	86.91	83.89	87.80	85.39	153.11	74
M24r.2r	87.09	84.12	87.98	85.58	153.17	75
M24An	87.63	84.12	88.69	85.98	153.31	76
M24Ar	88.06	85.81	89.31	86.83	153.59	77
M25n	88.55	86.60	90.02	87.45	153.81	78
M25r	89.27	87.30	91.18	88.26	154.08	79
M25An.1n	89.47	87.66	91.38	88.50	154.16	80
M25An.1r	89.90	88.37	91.97	89.04	154.35	81
M25An.2n	90.46	88.92	93.16	89.76	154.59	82
M25An.2r	90.86	89.82	93.55	90.29	154.77	83
M25An.3n	91.27	90.19	93.90	90.65	154.89	84
M25Ar	91.49	90.61	94.71	91.10	155.04	85
M25n5	91.90	90.92	95.21	91.48	155.17	86
M25r5	92.21	91.31	95.62	91.83	155.29	87
M26n	92.69	92.19	96.37	92.49	155.52	88
M26r	93.61	92.40	96.86	93.03	155.70	89
M27n	93.83	93.19	97.75	93.61	155.81	90
M27r	94.28	93.51	98.00	93.94	156.02	91
M28n	94.76	94.20	98.80	94.56	156.18	92
M28r	95.14	94.62	99.48	95.02	156.40	93
M28An	95.85	95.44	(100.0)	95.68	156.55	94
M28Ar	96.04	96.19		96.13	156.73	95
M28Bn	96.77	96.45		96.64	156.87	96
M28Br	97.24	96.84		97.07	157.04	97
M28Cn	97.99	97.05		97.57	157.19	98
M28Cr	98.13	97.83		98.00	157.34	99
M29n	98.78	98.03		98.45	157.61	100
M29r	99.28	99.19		99.25	157.87	101
	(100.0)	(100.0)		(100.0)		(102)

Changes in Spreading Rates

It is important to examine the implications of our GPTS construction methodology for changes in seafloor spreading that affect the GPTS. *Cande and Kent* (1992a) applied their C-anomaly GPTS, which was derived mainly from anomalies recorded at a single ridge, to investigate Cenozoic seafloor spreading history on several ridges in different oceans. They reasoned that the optimal GPTS would minimize apparent abrupt changes in seafloor spreading when applied to a global array of spreading ridges. A similar approach would be sensible for the M-anomaly GPTS, but cannot easily be accomplished for two reasons. One is that sparse age constraints for the M-anomaly GPTS leave us little choice in adjusting the anomaly sequence because we can only interpolate ages between two dates, one on each end of the sequence. The other is that the Pacific M-anomalies are the only well-defined, complete sequence in which all anomalies are clearly identified, so comparison with other oceans is difficult. Nevertheless, we can investigate possible spreading rate variations within Pacific plate by comparing the three lineation sets.

To understand implications about spreading rates, it is helpful to review how such rates were treated in the polarity sequence model construction. For most steps of the analysis, spreading rates were removed as a factor by normalization. This step translated the anomaly sequence from distance in kilometers to a unit-less distance (i.e., percent of total). Subsequent steps combined age group polarity sequence models into whole lineation set models and a composite model using reference profiles (Fig. 12). The polarity blocks were adjusted in proportion in the whole lineation set model based on the

spacing of break-point anomalies in the reference profiles (Table 3). There is, however, a subtle assumption about spreading rates in this method: we have tacitly assumed that each anomaly occupies the same percentage of a given sequence on each ridge. In essence, this means that the ratio of spreading rates among the three ridges remained constant. This seems a reasonable first-order assumption because spreading rates in many oceans appear to change little for long periods between major tectonic reorganizations. Furthermore, without independent evidence of changes in the spreading rate ratios among the three ridge systems, it is difficult to make a more accurate assumption.

To further investigate differences in spreading rate among the three ridge systems, we plot, one-to-one, the polarity duration from pairs of the three lineation sets (Fig. 12B). If each of the two compared lineation sets maintained a constant spreading rate through the M0 - M29 time period, the polarity block comparison curve should form a straight line. Departure from a straight line indicates differences in spreading rates. This is because for constant spreading the width of a polarity block (or group of polarity blocks) in all three lineation sets should occupy the same percentage of the M0 - M29 time period.

The relative spreading rate plots (Fig. 12B) show departures of as much as ~10 % with the greatest difference between the Hawaiian and Phoenix lineations and the least between the Japanese and Phoenix lineations spreading rate curves. As a result, the Japanese and Phoenix anomalies relative to the Hawaiian anomalies appear similar. Compared with the Phoenix anomalies, the Japanese anomalies match well at the

beginning and end of the M-sequence, but in the middle, between about M7 to M22, they are slightly behind the Phoenix by ~7 % at maximum. Relative to the Hawaiian anomalies both the Japanese and Phoenix anomalies lag, from about M25 to M21, but then shift abruptly to leading, from M21-M7, with the Phoenix anomalies showing the greatest departure, ~11 % at M15. These differences indicate that spreading on the Hawaiian lineations was initially slower than that on the other ridges, but then became faster, after an abrupt change at around M20-M21 time. This time corresponds to a change in spreading ridge reorganization on the Pacific ridges [*Sager et al.*, 1988]. Another modest change in spreading has been recognized around M13-M15 time [*Nakanishi et al.*, 1989] but in the relative spreading rate curves, it caused only a minor kink (Fig. 12B).

Although differences in spreading rates are observed among the three ridge systems, the differences are not large and there is significant consistency, especially between the Japanese and Phoenix anomalies. Without independent data to determine and correct for actual spreading rates, our composite model is a reasonable approximation of the overall anomaly sequence. Despite such differences, we think that our composite model is a better representation of the polarity sequence than previous models based on one ridge system because it is more of a Pacific-wide average.

Comparison to Previous Polarity Block Models

In Figure 13, polarity block GPTS models from previous studies are compared with our Pacific composite model. The overall time span of the composite M-anomaly

GPTS is shorter than that of CENT95 and TS2004 because of the older age that we used for the base of M0r [*Channell et al., 2000*; *Gradstein et al.*, 2005] (Fig. 13). The shorter M0-M29 time period makes the frequency of reversals slightly higher, especially in M21-M29, as compared to the frequency in the same anomalies reversals in CENT95 and TS2004.

Our composite GPTS model shows minor differences in the distribution of polarity reversals compared to previous studies. The polarity sequences in CENT95 and TS2004 are almost the same, particularly for M0-M24, presumably because both are based primarily on magnetic profiles from the Hawaiian lineation set. For pre-M24 reversals, CENT95 and TS2004 are significantly different because CENT95 did not identify any subchrons in M25. In contrast, TS2004 used M25 and older polarity chrons derived from aeromagnetic and deep-tow magnetic data with higher resolution than the sea surface data used for other chrons. Comparing our GPTS to the previous studies: (1) the distribution of polarity reversals within M0-M5 is about the same, (2) M6-M15 are slightly different and the polarity seems to be biased toward normal in previous models while the polarity seems to be distributed more-or-less equally in our model, (3) M16-M21 are about the same but more evenly spaced in our model, and (4) M21-M29 are nearly the same.

Age Calibration

A significant challenge for the current M-anomaly GPTS is age calibration, which is poor owing to the paucity of reliable radiometric dates directly tied to magnetic

anomalies. In this section, we summarize how our choices of age calibration are different from those of previous studies.

Unlike *Cande and Kent* (1992a), who could use nine radiometric ages for calibration, we found only two dates that seem reasonably well constrained for our GPTS: 125.0 Ma for M0 and 155.7 Ma for M26. The former date is suggested from a recent revision of the Aptian/Barremian stage boundary [*Channell et al.*, 2000] and re-evaluation of biostratigraphy and radiometric age data from MIT Guyot in the Pacific [*Pringle et al.*, 2003; *Gradstein et al.*, 2005]. The latter date is from $^{40}Ar/^{39}Ar$ dating of celadonite veins cored from M26-age crust in the Argo Abyssal plain [*Ludden*, 1992]. Although there may have been a time lag because celadonite was deposited by hydrothermal processes, it is thought that the delay was small because the hydrothermal circulation was likely driven by heat near the ridge crest.

There are other dates available, but none are direct or free of uncertainty. Many available dates of basement from drilled cores on the M-anomalies are biostratigraphically constrained and lack the accuracy of radiometric ages (e.g., DSDP Site 417 (M0r) in the Atlantic, DSDP Site 303 (M4), 304 (M9), and 307 (M21) in the Pacific). A couple of radiometric ages measured on basement cores drilled on M-anomalies are not used in this study. One is the Ar^{40}/Ar^{39} date (126 Ma) from basalt core at DSDP Site 387 in the Atlantic for M16. This date is significantly offset from biostratigraphic ages from overlying sediments. Furthermore, this date is close to the accepted age of M0. For both reasons, this date is probably misleading. The other is a 127 Ma Ar^{40}/Ar^{39} date from a basalt core drilled at ODP Hole 1149D on anomaly M12

in the western Pacific M12 [*Pringle*, 1992]. This age is also significantly younger than expected on the basis of TS2004 age for the M12 anomaly. Moreover, older (132 Ma) nannofossils are found in the basal sediments, suggesting that the cored igneous rocks may be a late stage sill above the Jurassic basement.

The dates for M0 and M26 are different from those used in CENT95, which used 121.0 Ma for M0 and 154.0 Ma for M26 with linearly-interpolated ages for the rest of the polarity boundaries. The former date was inferred from terrestrial stratigraphy, which was later reinterpreted and shifted ~4 Ma by *Channell et al.* (2000). The latter date was inferred from U-Pb and $^{40}Ar/^{39}Ar$ ages in Oxfordian-Kimmeridgian strata [*Channell et al.*, 1995a]. The dates used in CENT95 were revised in TS2004. TS2004 used the same two dates that we used for M0 and M26. In addition, TS2004 contains stratigraphic and radiometric ages for stage boundaries, tied to the reversal sequence by magnetic stratigraphy with interpolation in between those boundaries assuming a constant spreading in the Hawaiian lineations [*Gradstein et al.*, 2005]. We did not use these stratigraphic ages because they are indirect and include uncertainty in the determination of stage boundary ages in terrestrial stratigraphy and their correlation to the reversal sequence.

Without a larger series of age calibration points, uncertainty in absolute duration of each polarity in our model remains greater than other well calibrated GPTS (e.g., Quaternary in TS2004) [*Gradstein et al.*, 2005]. Although absolute ages remain poorly defined, the polarity reversal sequence is robust and can be recalibrated when more reliable ages become available.

Implication of the New M-anomaly GPTS

Discrepancies between our GPTS and previous models are first explained by differences in the collection of magnetic profiles and the particulars of age calibration points. CENT95 is primarily based on one profile from the Hawaiian lineation set and two calibration dates whereas TS2004 is a composite of the *Larson and Hilde* (1975), *Handschumacher et al.* (1988), and *Sager et al.* (1998) polarity models. In TS2004, the Hawaiian lineation-based reversal sequence [*Larson and Hilde*, 1975] was extended backward with aeromagnetic [*Handschumacher et al.*, 1988] and deep-tow magnetic [*Sager et al.*, 1998] studies of the Japanese lineations. The GPTS developed in the present study is an average representation of many magnetic profiles with wide geographic distribution. Unlike previous models, in which polarity interval durations were determined from one or a small number of magnetic profiles, polarity interval durations in our model are derived from an average of many individual polarity boundary locations.

It should be noted that different methods of determining polarity boundaries result in somewhat different polarity boundary distributions in a GPTS, particularly for M11 and M12, where many subchrons are identified. These subchrons are interpreted from small amplitude, short wavelength anomalies, for which polarity boundary locations can be shifted slightly depending on the method used to model the location of polarity boundaries. Our modeling resulted in a reversal sequence with nearly zero polarity bias, whereas previous studies derived a sequence that is more dominantly normal polarity in the M11 and M12 period (Fig. 13).

The distribution of polarity reversals significantly affects polarity reversal rates, which have been used to investigate paleo-geomagnetic field behavior. Although reversal rates derived from CENT95, TS 2004, and this study give similar reversal rate curves as a whole, our study gives a smoother curve compared to other two (Fig. 14). The CENT95 curve shows a peak in reversal rates between 130.0 and 135.0 Ma and diminishing rates before 150.0 Ma. The former is attributed to many subchrons between M10-M15, and the latter is attributed to omitted subchrons in the pre-M24 reversal sequence. The TS 2004 curve also shows a peak between 135.0 and 140.0, and an abrupt increase to high rates between 152.0 and 157.0 Ma. Again the young peak results from M10-M15 subchrons. This peak is offset from CENT95 because of an older age used for M0. The older, abrupt peak is attributed to the discontinuity resulting from the use of polarity block models made from higher resolution magnetic profiles in *Handshumacher et al.* (1988) and *Sager et al.* (1998). The curve from this study is similar to that from TS2004, but it is smoother and does not show such an abrupt rise before M25. This smoothness results from the more even distribution of polarity blocks as compared to the other two models and it implies that changes in reversal rate were smoother than previous models. If one accepts the premise that actual changes in reversal rate were more likely to have been smooth, then this observation implies that our model is a better representation of the polarity sequence.

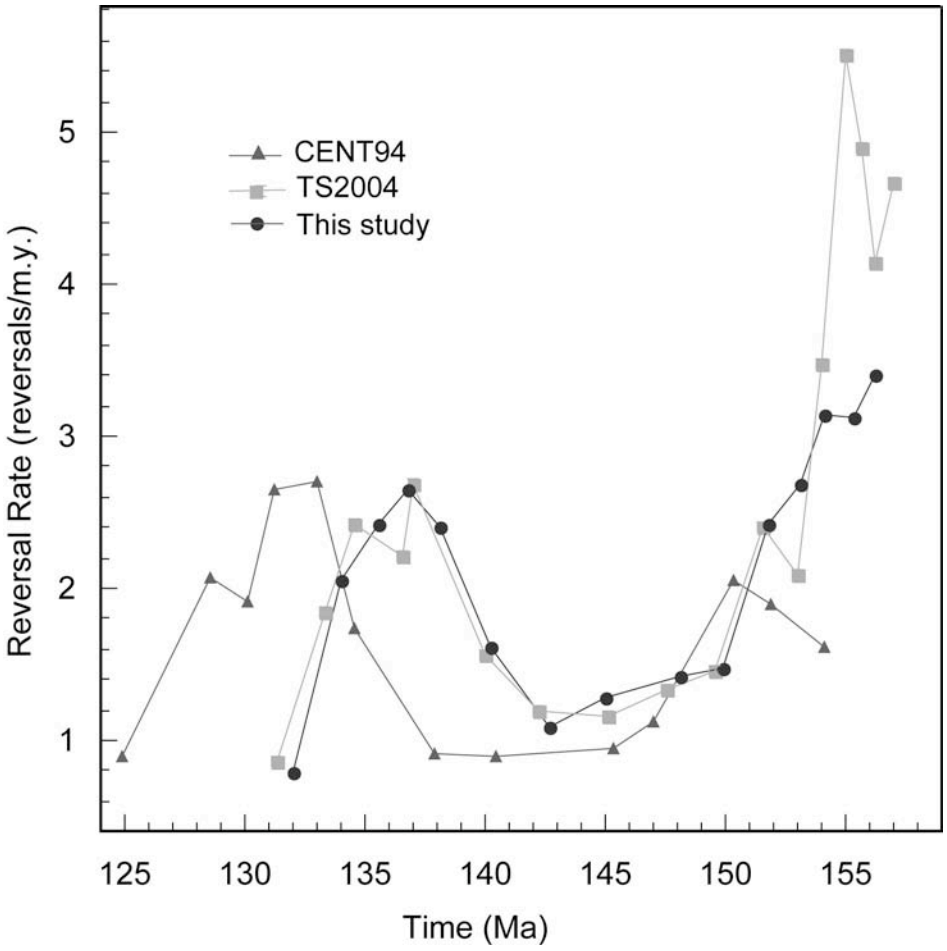

Figure 14. Late Jurassic-Early Cretaceous magnetic polarity reversal rate versus age for the GPTS calculated in this study compared with others. The black curve with circles is from this study; the gray curve with triangles is from CENT94; and the pale gray curve with squares is from TS2004. Reversal rate values were calculated at 2 m.y. intervals with a 4 m.y. sliding window. Note that the CENT94 time scale has an offset at M0 compared to TS 2004 and this study that is a result of a younger age assignment for M0.

Atlantic M-anomalies

It is natural to compare M-anomalies observed elsewhere in the ocean basins with the new Pacific composite GPTS model. Most extra-Pacific M-anomaly sequences are incomplete and difficult to correlate, but the North Atlantic M-anomalies do display a complete sequence from M0-M25. Older anomalies are not widely recognized in the North Atlantic because of their low amplitudes (Fig. 15A-B).

Keathley and Canary Block Models

We constructed an Atlantic M-anomaly block model in a manner similar to the Pacific models. We used a total of 4 anomaly profiles from the Keathley lineations (off northeast coast of the U.S.) and 7 from the Canary lineations (off northwest coast of Africa). All profiles are located between the Atlantis and Kane fracture zones (Appendix A). These profiles are closely spaced and perpendicular to the previously-determined lineation strikes, and because they contain the entire anomaly sequence, we did not have to normalize the profiles; instead, we used actual distance to calculate polarity spacing. To deskew the magnetic anomaly profiles, we used paleo-inclination and declination determined from average paleomagnetic poles for North America (120, 130, 140, and 150 Ma) [*Besse and Courtillot*, 2002].

The north Atlantic polarity model has standard deviations of polarity boundary locations (4-28 km) similar to the Pacific model through M0 –M5r and M16n-M20 for Keathley and Canary lineation sets, respectively. These uncertainties become greater (as high as 36 km) through M17-M25 and M21r-M25 in the Keathley and Canary lineation

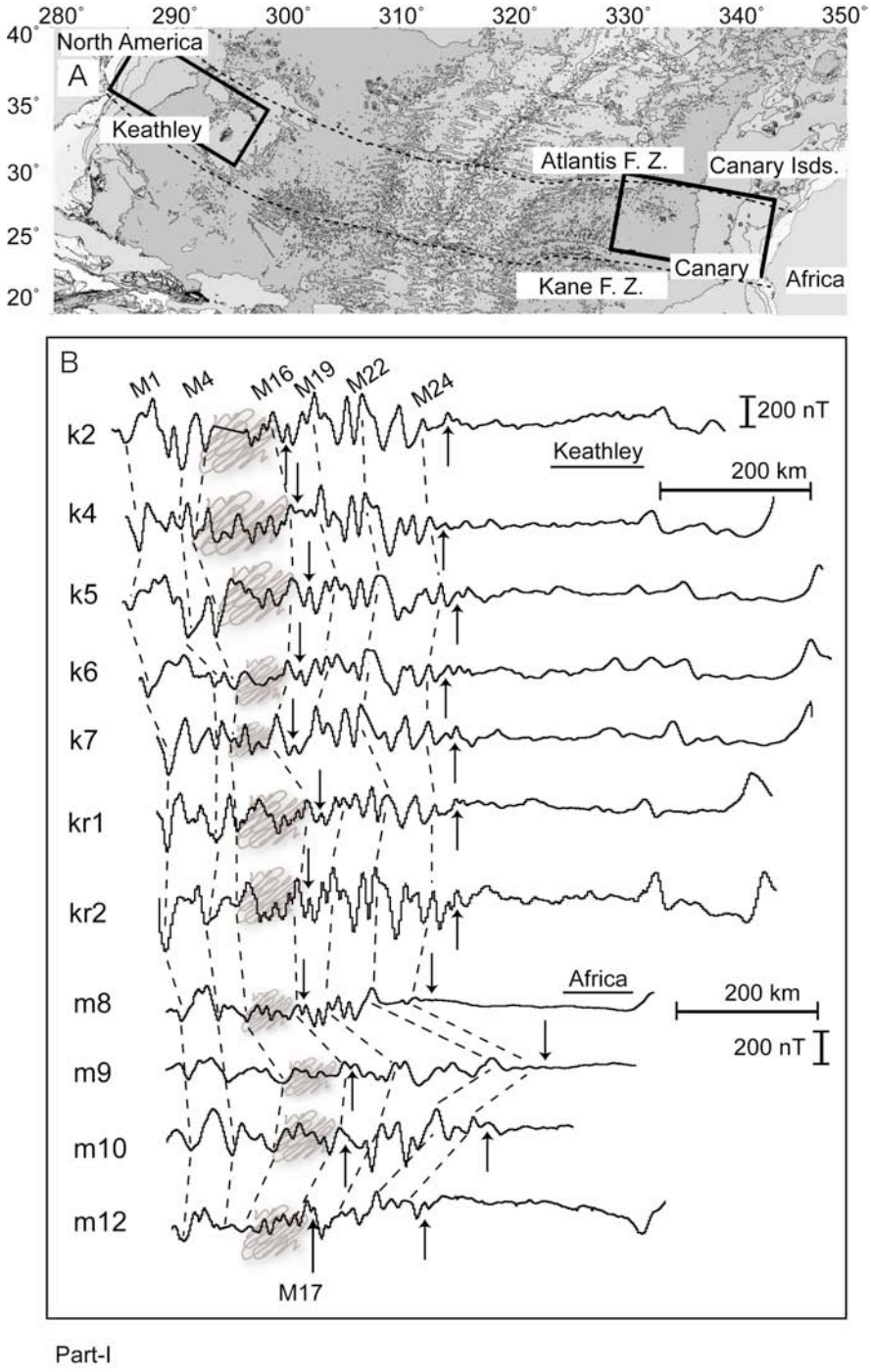

Figure 15. Summary of north Atlantic M-anomalies. (A) Locations of the Keathley and Canary lineation sets. Doted lines indicate Atlantis fracture zone (north) and Kane fracture zone (south). (B) Selected anomaly profiles from the north Atlantic basin. k2-k7, kr1-kr2, and m8-m12 are profiles listed in Appendix A. Scratched marks indicate the poorly expressed zone anomaly identification in the Atlantic M-anomalies (M5r-M15r). Dashed lines indicate anomaly correlations.

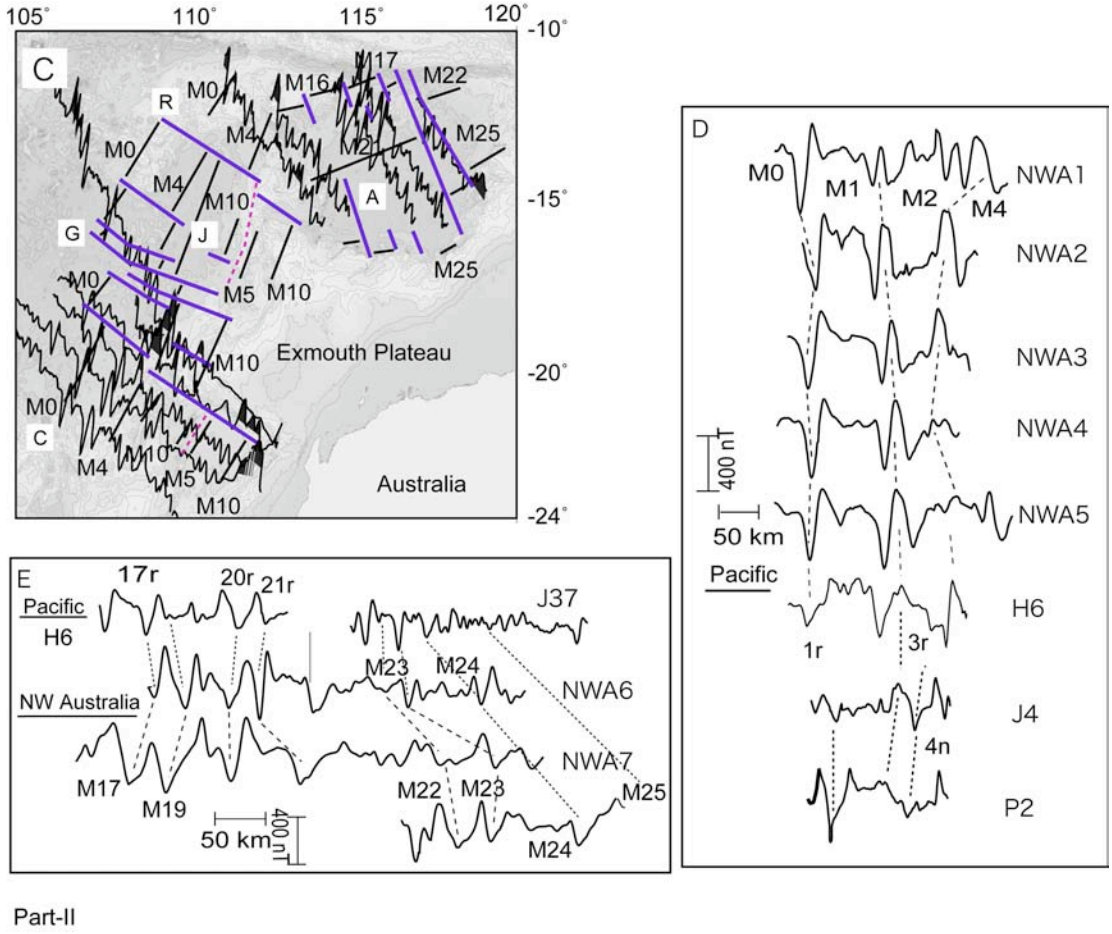

Figure 15. Continued. (C) Northwest Australia lineation sets. A = Argo Abyssal Plain, J = Joey Rise, R = Roo Rise, G = Gascoyne Abyssal Plain, and C = Cuvier Abyssal Plain. Purple solid and pink dotted lines indicate fracture zones and ridge jumps identified in Sager et al. (1992). (D) Selected M0- M4 anomaly profiles from the magnetic profiles shown in C. Corresponding anomalies from Pacific lineation sets are also shown. Dashed lines indicate anomaly correlations. (E) Selected M17-M25 anomaly profiles from the magnetic profiles shown in C. Dashed lines indicate anomaly correlations. Corresponding anomalies from Pacific lineation sets are also shown.

sets, respectively. The increase probably results from difficulty in identifying short duration polarity blocks that characterize pre-M22 anomalies. After we calculated the locations of the polarity boundaries, the block models were averaged, resulting in Keathley and Canary average models (Fig. 16). Anomalies from M5 to M16 are not

included because they are poorly expressed and difficult to correlate in the North Atlantic (Fig. 15, hatches in Appendix B).

The Keathley and Canary block models show little difference from one another in the distribution of polarities through M16-M25, indicating the spreading system at the contemporaneous north Mid-Atlantic Ridge was nearly symmetric. In contrast, the distribution of polarities show greater differences through M0-M4, implying the spreading system was asymmetric. From the observation of the different spreading distances and crustal accretion, the asymmetric spreading in the Atlantic is thought to indicate the interaction between MAR and a mantle plume [*Müller et al.*, 1998] or ridge jumps caused by asthenospheric flow during the M0-M4 period [*Bird et al.*, 2007].

Comparison between the Pacific and Atlantic GPTS Models

To investigate how well the Pacific composite GPTS model represents the nature of global M-anomalies, we compared synthetic anomaly profiles calculated by forward modeling of the Pacific anomalies to the Keathley and Canary block models. We used a magnetization distribution of ± 0.5 A/m for the low amplitude M5-M15 blocks and ±1 A/m for the rest of blocks (Fig. 16). Two anomaly profiles from the Pacific composite model are presented in Figure 16: one is the synthetic anomaly profile calculated with the Pacific spreading rates and the other is the synthetic anomaly profile calculated using the Keathley anomaly spreading rates.

The Pacific synthetic anomaly profile with Keathley spreading rates shows good agreement to that of the Keathley model for M0-M4 anomalies and to that of the

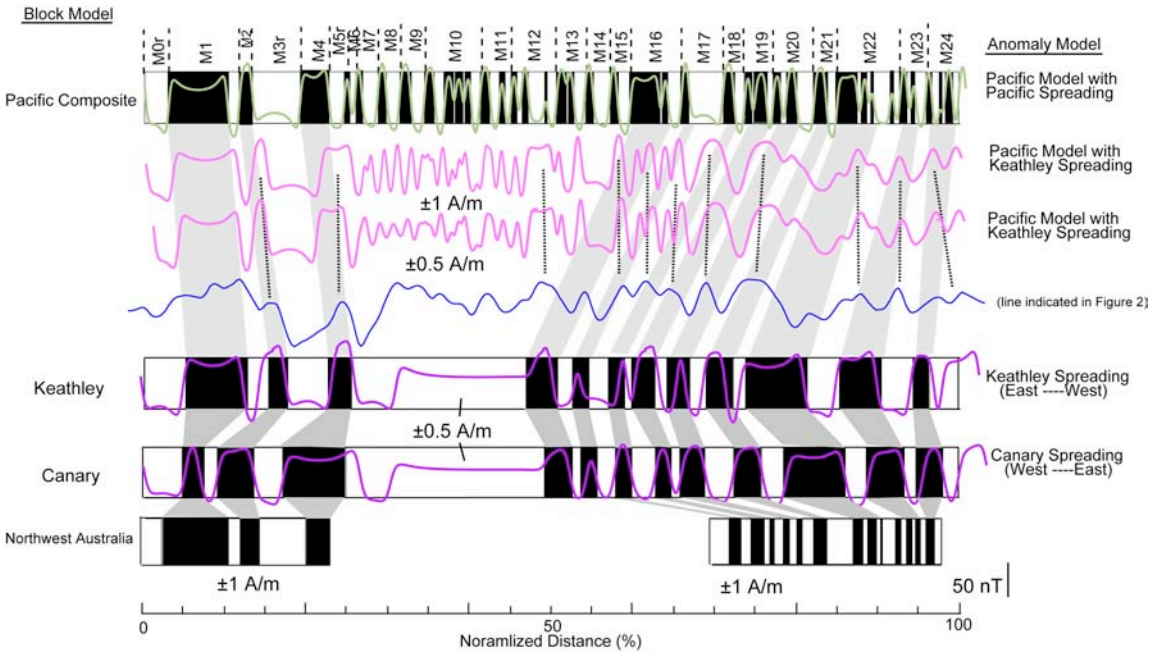

Figure 16. Polarity block models for the Keathley and Canary lineation sets in comparison to the Pacific composite model. M5r-M15r are left blank in the Keathley and Canary models because these anomalies are poorly expressed. Pale gray bands indicate correlations between the Pacific composite and Keathley, and the correlation between the Keathley and Canary lineations. Pink and green anomaly profiles are forward model results from the block models. The two pink profiles show forward model results from different magnetization values: ±1 A/m and ±0.5 A/m (in the M5-M15 zone) for upper and lower profiles, respectively. The green anomaly profile indicates the calculated anomaly from the Pacific composite model and the pink anomaly profiles show the calculated anomaly from the Pacific composite model with its spreading rate adjusted to fit the Keathley sequence. The blue profile shows an example of observed anomalies from the Keathley anomalies (k5 in Figure 15). The purple anomaly profiles indicate the calculated anomaly from the Keathley and Canary model.

Keathley and Canary models for M16-M25 anomalies. Lesser agreement for the Canary M0-M5 anomalies apparently results from asymmetric spreading. For the M16-M25 period, Pacific model anomalies have slightly greater amplitudes and are somewhat more distinct as compared to the Atlantic model. The Atlantic spreading system was evidently less capable of resolving the anomalies, perhaps because of slower spreading

or a wider crustal accretion zone that may blur the anomalies. During the M5-M15 period, which is blank in the Atlantic model, Atlantic anomalies are greatly diminished in amplitude, to the point of being difficult to correlate. As seen in Figure 16, the reduced magnetization Pacific anomaly model at Atlantic spreading rates shows much more distinct anomalies, implying that this diminution is not simply an effect of the spreading rate difference, but some more fundamental difference in the recording process. The discussion of this issue is beyond the scope of this study and will be presented in separate paper.

Atlantic Spreading Regime

To further investigate the implications of the Atlantic M-anomalies, we assigned ages for the polarity boundaries from the Pacific composite model to the Keathley and Canary block models (Appendix B). It is important to note that these ages for the polarity boundaries are based on the assumption of constant spreading rates and ratios in the Pacific model. Both Keathley and Canary block models show four distinctive periods of constant spreading rates: M25n-M21, M21n-M16n, M15r-M5r, and M5n-M0r (Fig. 17). The divisions prior to M16 are consistent with those defined by *Sundvick and Larson* (1988), however, our analysis suggests M15r-M5r as one spreading phase whereas they defined the spreading change at M10N. North Atlantic spreading rates dropped at M21 by nearly a factor of two. At M16n, the spreading rate again dropped by a factor of two, with spreading at only 9.5 km/m.y. for the Keathley lineations and 7.1

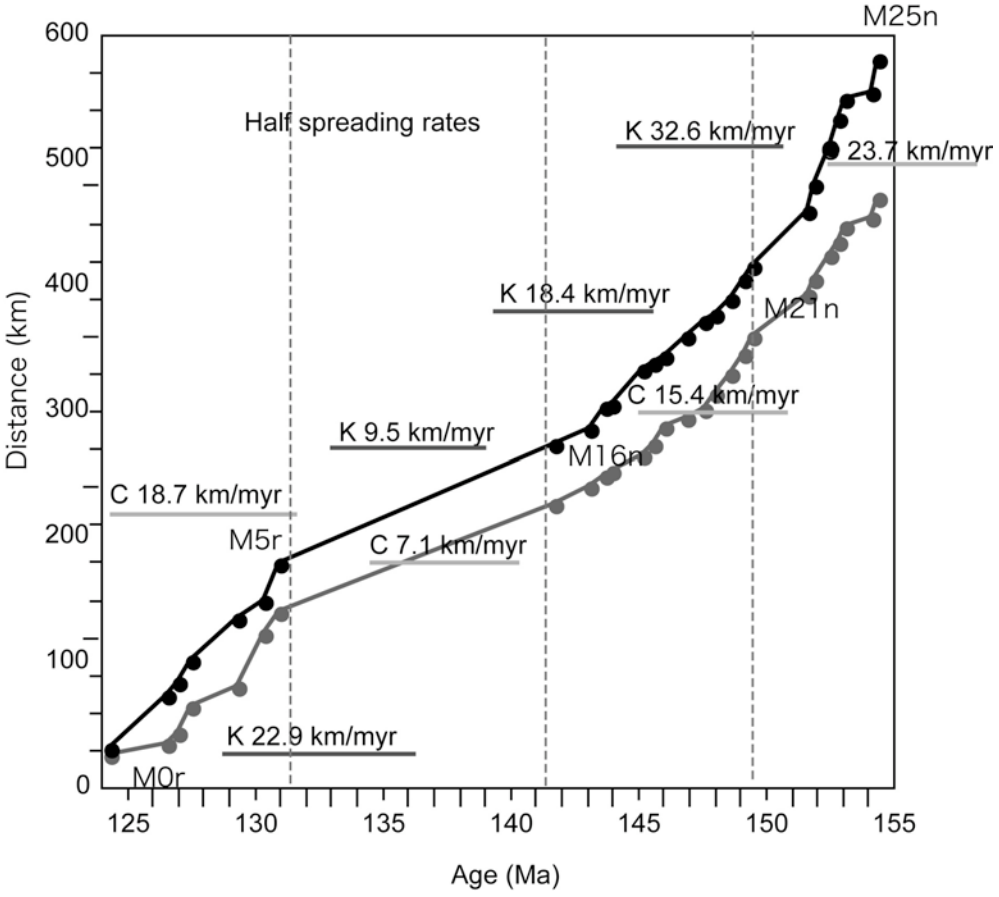

Figure 17. Half spreading rates calculated from averaged Keathley and Canary M-anomalies using the Pacific anomaly model (Appendix B). Four different periods of nearly uniform spreading rates are suggested (dashed lines). Pale gray solid circles indicate the polarity boundary in the Canary anomalies. Darker gray solid circles indicate the Keathley anomalies. K=Keathley spreading rates and C = Canary spreading rates.

km/Myr for the Canary lineations. After ~10 Myr of slow spreading, the spreading rates increased, approximately doubling from M5r-M0 (Fig. 17).

The shift from long-term spreading rate decline (M25-M5) to increase (M4-M0) in spreading rates coincides with changes in the variability in the distribution of polarities. Recall that the distribution of the Keathley and Canary polarity blocks show polarity spacing nearly equal during M25-M16 but asymmetric from M4-M0. This

coincidence implies that a significant change in spreading regime occurred at the paleo Mid-Atlantic Ridge at the time of M5-M4. The nearly identical polarity distribution between Keathley and Canary models through the period of M24-M16, with intermediate-slow spreading rates, suggests that the Mid Atlantic Ridge spreading regime was similar to that of modern day intermediate spreading ridges. We assume that while the spreading rates gradually dropped from intermediate to almost ultra-slow during this time period, the symmetric spreading regime gradually shifted to asymmetric spreading as seen during the period of M4-M0.

Northwest Australia Lineation Set

To further examine the global validity of the Pacific GPTS, we also compared our time scale to the northwest Australia M-anomaly lineation set (Fig. 15 C-E). The northwest Australia sequences show very similar anomaly characteristics (i.e., spacing, amplitude, shape) to that of the Pacific anomalies, probably because of the intermediate to fast spreading rates [*Robb et al.*, 2005]. With the northwest Australian lineation set, we are unable to construct a continuous polarity block model because the anomaly sequence is missing a large section (M7-M15) between the anomaly sequences in the Cuvier-Gascoyne and Argo abyssal plains (Figure 15C). Furthermore, parts of the Gascoyne sequence are difficult to model owing to ridge jumps [*Fullerton et al.*, 1989; *Robb et al.*, 2005].

For the comparison of the Pacific and Australian M-anomalies, we focused on two piece- meal sections: M0-M4 and M17-M24 (Figure 15D-E). A total of 5 profiles

from Cuvier Abyssal plain and 2 profiles from Argo Abyssal plain were used to construct M0-M4 and M17-M25 block models, respectively (Fig. 15C). The methodology for the construction of block models was the same as for the Keathley and Canary block models (Appendix C).

The resulting block models are shown in Figure 16. Overall distribution of polarity spacing agrees with that of the Pacific, including short wavelength features in the anomalies prior to M17. The similarity between the Pacific and northwest Australia anomalies and the agreement in polarity spacing between their block models indicate that the Pacific-based GPTS provides an adequate model for the northwest Australia lineation set.

CONCLUSIONS

(1) We collected and correlated 87 segments of magnetic profiles covering all three Pacific M-anomaly lineation sets and constructed a revised GPTS model that spans M0 to M29. Two dates were used to calibrate the GPTS, one for M0r (125 Ma) and one for M26n (155.7 Ma), with linear interpolation in between. Although age constraint is poor, our compilation represents a wider and statistically more robust analysis of anomalies, giving a more reliable record of changes in the Earth's geomagnetic field than previous models.

(2) Overall anomaly correlations among the three lineation sets are excellent and major polarity chrons are mostly unchanged from previous studies. New subchrons were identified in M13 and M16, whereas one subchron was dropped from M11 and M24.

(3) The new M-anomaly GPTS shows minor differences in the spacing of polarity chrons as compared with previous models because (a) we used a different collection of magnetic anomaly profiles, and (b) there are a few differences in anomaly correlations, such as adding subchrons (M13 and M16) and dropping subchrons (M11 and M24). The new GPTS shows more regular spacing of polarity zones than previous GPTS.

(4) Careful selection of anomaly profiles made it possible to build a robust block model in which the accuracy of the location of polarity boundaries (average standard deviation 11~ 17 km) is similar to that of well accepted C-anomaly block model of Cande and Kent (1992).

(5) Interpretation and application of pre-M24 anomalies should be approached with caution because the small amplitude, short-wavelength anomalies that characterize the pre-M24 sequence are more difficult to correlate uniquely than younger anomalies.

(6) Comparison among spreading regimes in the three lineation sets indicates that all had almost the same spreading history. Two minor changes in relative spreading are observed around M13-M15 and M20-M21.

(7) The good agreement between the Pacific, Atlantic, and northwest Australian anomalies implies that the Pacific model is representative of the global anomaly signal.

CHAPTER III

THE ORIGIN OF THE SMOOTH ZONE IN EARLY CRETACEOUS NORTH ATLANTIC MAGNETIC ANOMALIES

OVERVIEW

Late Jurassic- Early Cretaceous marine magnetic anomalies observed in the north Atlantic Ocean exhibit an abrupt change in character in M15-M5 crust. The anomalies are smoother with low amplitudes, and are difficult to correlate among nearby profiles. The accepted explanation for the origin of this smooth zone is diminished resolution and anomaly interference due to slow spreading rate. We have made magnetic models of these anomalies that indicate low spreading rates are not the sole reason for the smooth zone. Combined with other geophysical evidence, our study implies that two additional factors are responsible for the origin of the smooth zone: a decrease in geomagnetic field intensity and a thinned crustal basalt layer or a non-basaltic magnetic source layer resulting from low melt supply during a period of ultra-slow (~ 7 km/Myr) spreading.

INTRODUCTION

Linear magnetic anomalies are nearly ubiquitous in the ocean basins. These anomalies are attributed to the recording of contemporaneous magnetic field by the upper oceanic crust [*Vine and Matthews*, 1963]. The remarkable consistency of anomaly shapes and spacing has allowed these anomalies to serve as the basis for models of geomagnetic polarity reversal sequence. However, in some places the magnetic

anomalies are not so regular and clear. One such area is the magnetic "smooth zone" in the middle of the Late Jurassic – Early Cretaceous anomalies (M-anomalies) in the North Atlantic Ocean.

This zone ("Atlantic M-anomaly Smooth Zone" or AMSZ) is located in between M5 and M15 on conjugate sides of the Mid-Atlantic Ridge (MAR) and has been known for nearly four decades (Figure 1). Previous magnetic studies suggested that the origin of AMSZ was a decrease in spreading rate, which resulted in diminished anomalies due to closely-spaced, polarity zones that induce overlapping, interfering magnetic anomalies [*Sundvik and Larson*, 1988]. This explanation is suspect because slow spreading elsewhere in the Atlantic has produced clear anomalies. Thus, we ask did the AMSZ result solely from slow spreading rates? Are there other possible causes? In this paper, we present an analysis of magnetic anomalies and other geophysical data to shed light on the origin of the AMSZ.

BACKGROUND: ATLANTIC M-ANOMALIES

Atlantic M-anomaly lineations are well mapped and coherent in most of the northwest Atlantic basins (Keathley lineations, 29 - 38 N, 73 -60 W) and near the Canary Islands (Canary lineations, 10 - 35 S, 30 -10 W), the conjugate side of the MAR (Figure 18). Compared with the Pacific magnetic lineations that have been used to develop the M-anomaly reversal sequence model, those in the North Atlantic are dominated by longer wavelengths due mainly to the slower spreading rates. Both the Keathley and Canary anomalies are clearly linear and consistent in shape between M0-

M4 and M16-M21. In contrast, between M5-M15 and prior to M25 the anomaly shapes are less regular and amplitudes are smaller [*Vogt and Einwhich*, 1979].

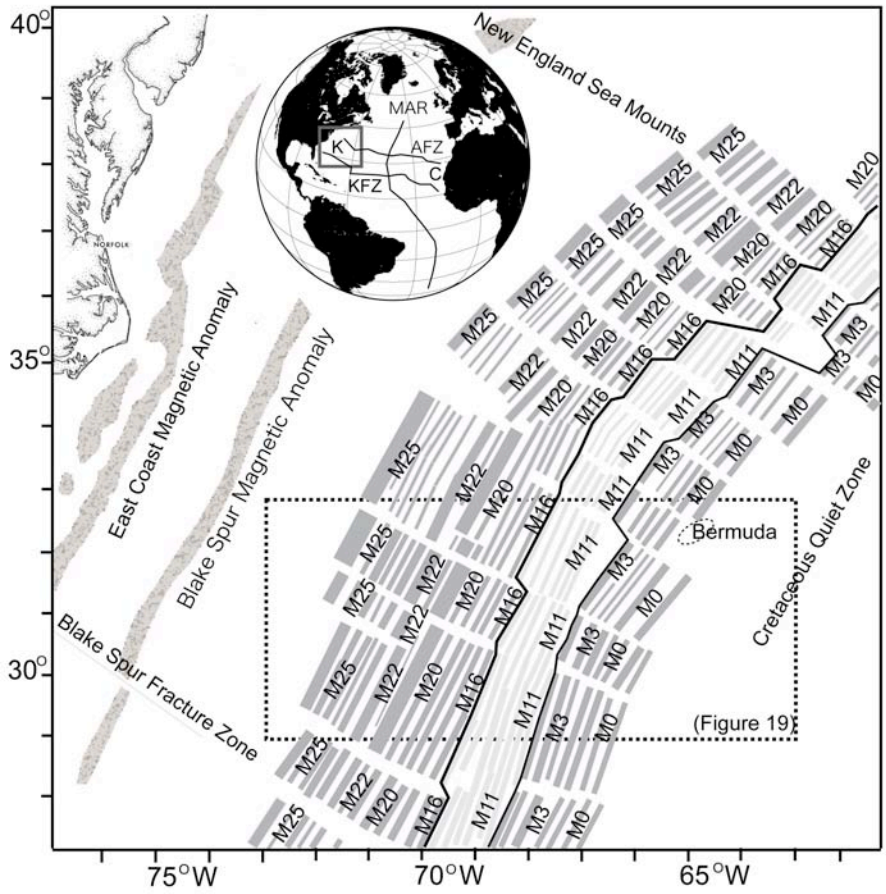

Figure 18. The map of the Atlantic M-anomaly lineations modified from Schouten and Klitgord (1977). The box on the globe shows the area of this map. MAR = Mid Atlantic Ridge, AFZ= Atlantis Fracture Zone, KFZ= Kane Fracture Zone, K = Keathley lineations, and C= Canary lineations. Darker gray bands indicate positive anomaly lineations (M16-M25). Lighter gray bands indicate positive anomaly lineations with lower amplitudes and smoother character. The black solid lines along M16 and M4 show the bounds of the AMSZ. The box indicates the area of anomalies analysed in this study.

In addition, M5-M10 only spans one forth of the distance that M11-M15 spans (Figure 18), indicating that there may be a change within the AMSZ with the slowest spreading between M5-M10.

The true extent of the AMSZ is undefined. The smooth zone was originally recognized between M5-M15 [*Larson and Pitman*, 1973] in the Keathley lineations where anomaly characters do not closely resemble the contemporaneous anomalies in the Pacific. *Schouten and Klitgord* (1977, 1982) correlated anomalies in the AMSZ based on Project MAGNET aeromagnetic data; although, the anomalies showed less correlatability and repeatability compared to anomalies outside of the AMSZ. The AMSZ is also recognized between M5-M14 ubiquitously in Canary Basin, the conjugate side of the MAR [*Hayes and Rabinowitz*, 1975]; however, the anomaly character is more diminished compared to that of the Keathley lineations. In this study, we define the AMSZ between M5-M15 because of the changes in anomaly characters compared to M-anomaly character elsewhere in both the Keathley and Canary M-anomaly lineations.

Several seismic studies have observed changes in basement topography, crustal structure and thickness, and mantle velocity gradient near the older boundary of the AMSZ [*Grow and Markl*, 1977; *Lizarralde et al.*, 2004]. Basement topography shows a transition from smooth to rough at around M11 in the middle of the AMSZ, observed in both the Keathley and Canary crust. Older crust displays smoother seafloor whereas younger crust shows rough, ~1.0 – 1.5 km topographic relief [*Grow and Markl*, 1977; *Ranero et al*, 1997]. Seismic section over older crust shows many crustal architecture characters (e.g., clear Moho, faults in the lower crust) suggesting the stratified upper and

lower crust whereas none of those characters appears in the younger crust [*McCarthy et al.*, 1988; *Morris et al.*, 1993]. Together with decreasing spreading rates, this transition from the smooth (older than the AMSZ) to rough topography indicates a shift from a magmatic-dominated spreading to tectonic-dominated extension in the crustal construction at the MAR [*Vogt et al., 1969*; *Lizarralde et al.*, 2004]. The abrupt lateral changes in bulk mantle seismic properties observed in crust younger than M11 indicate that the retention and crystallization of melt occurred in the shallow mantle due to the low melt extraction, resulting in ~ 1.4 km thinner crust than that of prior to M11 [*Lizarralde et al.*, 2004]. The location of this transition does not exactly coincide with the older boundary of the AMSZ probably because changes in spreading regimes gradually affected to the crustal construction.

ANOMALY ANALYSES

In this study, we focused on analyzing magnetic profiles from Keathley lineations because both magnetic and seismic studies have been carried out in this area. Two sets of Atlantic M-anomaly data have been collected from the Keathley lineations, both with subparallel, East-West oriented track lines, nearly perpendicular to the magnetic lineations. The first is a set of ship tracks with 20-minute spacing between lines collected during the 1967-68 U.S.N.S *Keathley* cruise (Figure 19). The second consists of closely-spaced (11 minute) aeromagnetic profiles collected by Project MAGNET [*Schouten and Klitgord*, 1982]. Unfortunately, the Project MAGNET data is unavailable, so our analyses are based on the sea surface profiles.

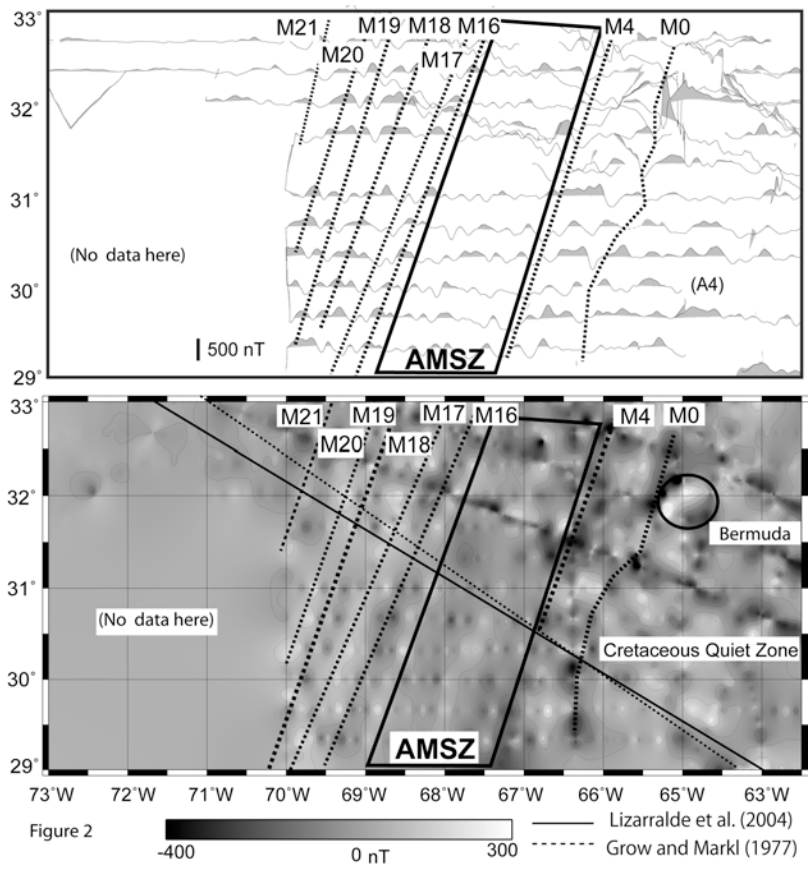

Figure 19. Atlantic M-anomalies for the area indicated by the box in the figure on page 68. These data were collected by USNS *Keathley*. (A) Anomaly profiles with positive anomalies filled by gray. The profile in black is the reference anomaly profile in Figure 3. (B) Contour map of anomaly amplitude produced from the profiles in (A). Gray bars indicate previously identified anomaly lineations (e.g., Schouten and Klitgord, 1982). Two seismic lines are indicated by solid (Lizarralde et al., 2004) and dotted (Grow and Mark, 1977) black lines.

We analyzed the magnetic lineations of the Northern Atlantic crust during M0-M24 by constructing polarity block models. For calibration, we used a polarity sequence derived from Pacific M-anomalies, which is standard because rapid spreading in the Pacific resulted in a detailed record of magnetic polarity. Although we used our own

model of the Pacific polarity sequence, this new model is not significantly different from previous, widely-accepted models. For the Atlantic models, a compilation of 7 (Keathley) and 4 (Canary) anomaly profiles were used to build normalized polarity block models. A polarity block model from each magnetic profile was normalized to the width of M0-M25 because different areas of the North Atlantic have somewhat different local spreading rates. Normalized locations of polarity boundaries were averaged to determine the average width of each polarity block in the M0-M25 span. Ages for polarity boundaries for the Keathley and Canary block models were derived by assigning polarity boundary ages from the Pacific composite geomagnetic polarity reversal time scale (Figure 20B). Spreading rates for the Keathley and Canary lineations were derived by computing age-distance curves from the averaged polarity block models.

Synthetic magnetic anomalies were calculated from these block models using 2D forward modeling with appropriate geographic parameters (i.e. ambient field and skewness factors). For comparison, the Pacific model was computed and adjusted to the spreading rate of the Keathley lineations (Figure 20A). For simplicity, we assumed that the magnetic source is a homogeneously magnetized, constant thickness layer in all the models. To test the effect of magnetization strength on the coherency of Atlantic

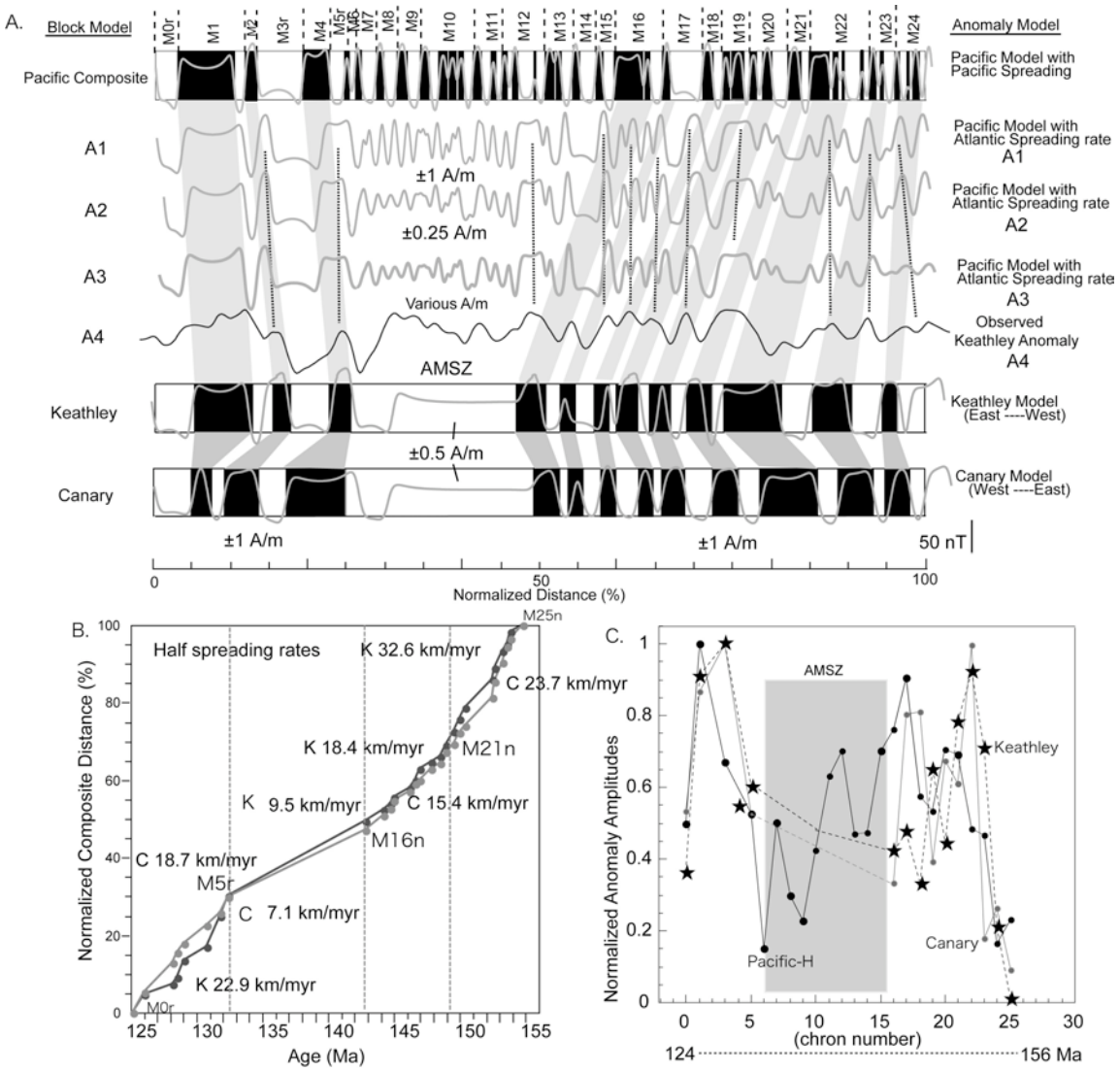

Figure 20. Results from anomaly analyses. (A) Normalized polarity block models built on the compilation of the Pacific, Keathely, and Canary anomalies (see text). The gray bands show the correlations of polarity blocks amongst different models. The top block model represents the Pacific composite model. A1, A2, and A3 anomaly profiles show synthetic anomaly models calculated from the Pacific-derived polarity model with the Keathley spreading rates and various magnetization values. The bottom two block models represent the Keathley and Canary models. Overlying anomaly profiles show synthetic anomaly model calculated from the block models. (B) Half-spreading rates for the Keathley (Ke) and Canary (Ca) magnetic lineations using the Pacific polarity model. (C) Normalized anomaly amplitudes plotted against to chron numbers. The solid circles, stars, and gray circles indicate the Pacific (Hawaiian), Keathley, and Canary profiles, respectively.

anomalies, we constructed several synthetic anomaly profiles calculated with different magnetization values. The first used a magnetization value of 1 A/m because this provides a good match to anomalies outside the AMSZ. An additional synthetic profile was calculated using a magnetization of 0. 25 A/m for the AMSZ to see if this much lower values is an adequate explanation for the observed low-amplitude anomalies. Another model was calculated using a varying magnetization that was derived from the curve of Pacific anomaly amplitude versus time (Figure 20A-3).

The anomaly amplitude versus time curve was constructed for the Pacific anomalies. For each anomaly, we measured the amplitude from the peak of the positive the trough of the negative and normalized by the maximum amplitude value in the magnetic profile from the each lineation set. For comparison, we also computed similar curves for Atlantic anomalies outside the AMSZ. Barring wholesale changes in crustal chemistry, these amplitudes can be a proxy for geomagnetic field intensity [*McElhinny and Larson*, 2003]. Normalized amplitude (field intensity) models for each of the Pacific, Keathley, and Canary lineation sets were built on a representative, continuous magnetic profile collected during a single cruise in each of these lineation sets (Figure 3C). Using a single profile minimizes the influence of non-crustal geomagnetic field variations (e.g., diurnal effects, secular variation) that can occur with data compiled from multiple cruises.

RESULTS

The distribution of polarity spacing between the Keathley and Canary models is identical in M16-M24 but different in M0-M4. The Keathley and Canary lineations are conjugate pairs located on opposite sides of the MAR, so this discrepancy in the distribution of polarity spacing suggests that spreading was symmetric during M16-M24 but became asymmetric during M0-M4. Asymmetric spreading in the Atlantic is thought to indicate an interaction between the MAR and a mantle plume [*Müller et al.*, 1998] or ridge jumps caused by asthenospheric flow [*Bird et al.*, 2007].

The Keathley and Canary spreading rate curves show four abrupt changes similar to those recognized by Sundvik and Larson (1988)(Figure 20B). During the period M25n-M21n, half-spreading rates were 32.6 (K: Keathley) and 23.7 (C: Canary) km/Myr, an intermediate spreading rate, such as that observed on the modern Juan de Fuca Ridge. Spreading rates decreased by a factor of two, 18.4 (K) and 15.4 (C) km/Myr, during M20r-M16n. In the AMSZ (M15-M6), the interpolated spreading rate dropped to 9.5 (K) and 7.1 (C) km/Myr, rates that are considered ultra-slow spreading rates (half spreading < 10 km/Myr) similar to these observed on the modern Southwest Indian Ridge (SWIR) [*Sauter et al.*, 2008]. After the AMSZ, the spreading rate increased back to 22.9 (K) and 18.7 (C) km/Myr, rates that are similar to the fastest of present MAR spreading rates.

Paleomagnetic studies have suggested a long-term paleointensity-low during the period 120-160 Ma [e.g., *Tauxe*, 2006]. Both Pacific and Atlantic anomaly amplitude curves show variations during this period, but overall the anomaly amplitudes are also

low. The relative amplitude curves from the Pacific and Atlantic show synchronous peaks, trends, and transitions between peaks (Figure 20C). From M25, the intensity increases from low values to peak at M20, decreases between M20-M4 making a "valley", with values as low as 20 % of the full field intensity at M6.

The anomaly expressions in the synthetic anomaly profiles from the Pacific, Keathley, and Canary block models show obvious correlatability and repeatability over the M-anomalies except for the AMSZ. For M5-M15 anomalies in synthetic profiles calculated from different but lower magnetization values show distinct anomalies in contrast to the observed anomalies, which are smooth and are not reproduced by modeling with slow spreading and low magnetization values (Figure 20A).

THE ORIGIN OF THE AMSZ

Previous interpretations of North Atlantic anomalies suggested that the AMSZ resulted from slow seafloor spreading [e.g., *Sundvik and Larson*, 1988]. Our examination of spreading rates confirmed that the time period corresponding to the AMSZ, indeed, had anomalously slow spreading rates (Figure 20B). The appearance of marine magnetic anomalies is certainly a function of spreading rate and slow spreading can cause a reduction in anomaly amplitude and detail because of overlapping and interfering anomalies. This is probably part of the explanation for the AMSZ, but our modeling shows that it is insufficient to explain the observed muted anomaly character. Observed AMSZ anomalies are more subdued than modeled anomalies and have different characteristics than the anomalies prior to and after the AMSZ. The AMSZ

anomalies do not exhibit the same coherency in anomaly character, such as the locations of peaks, troughs, and long-wavelength features (Figure 20A). These observations imply that there are other factors causing the AMSZ.

Assuming a uniform crustal formation, anomalies recorded by the crust are an expression of geomagnetic field strength [e.g., *McElhinny and Larson*, 2003]. Following the global trend of changes in normalized amplitudes, it is reasonable to assume that the paleo-geomagnetic field behavior during M5-M15 in the Keathley and Canary (Atlantic) was similar to that of the Pacific (Figure 20C). This means that the anomaly amplitudes during M5-M15 were reduced as low as 20% of the maximum field intensity. The low geomagnetic field lowered magnetization recorded in the crust, which in turn produced lower amplitude magnetic anomalies. Nevertheless, as Figure 3 shows, even at 25% of the magnetization that explains surrounding anomalies, the model anomaly still shows anomalies that are more distinct than observed. While we propose that the intensity low was partially responsible for the production of the AMSZ, the uniquely smooth character of the observed anomalies remains unexplained.

Although a possible explanation for the appearance of the AMSZ is anomalous regional geomagnetic field over the Atlantic, this explanation seems unrealistic simply because such long-lived (M5-M16 = 10 Ma) anomalous behavior of the geomagnetic field has not been found in paleomagnetic studies. Instead, we think that the anomalous character of the AMSZ is largely a product of amagmatic spreading, which occurs in some ultra-slow to slow spreading regimes. This interpretation is bolstered by seismic studies [e.g., *Lizarralde et al.*, 2004] and geophysical, structural, and petrological

observations in modern ultra-slow and slow spreading environments [e.g., *Sauter et al.*, 2008; *Smith et al.*, 2008]. Other studies show that in such circumstances, the upper crust basalt layers (which normally record strong, linear magnetic anomalies) are attenuated or absent entirely.

In ultra-slow to slow spreading, a low melt supply results in the construction of a spatially heterogeneous crustal structure with thin basaltic crust and often the lower crust is exposed at the seafloor, e.g., ocean core complexes along the MAR [*Smith et al.*, 2008] and SWIR [*Sauter et al.*, 2008]. In such a spreading regime, much of the crust can consist of gabbroic rocks, which act as the magnetic source layer. The gabbro layer has a smaller magnetization, typically values as low as 25% of basaltic crust [*Sauter et al.*, 2008]. The exposed olivine-rich mantle rocks (i.e., peridotites) observed at slow and ultra-slow spreading are often serpentinized [*Dick et al.*, 2008]. With a large degree of surpentinization (>75 %), the mantle rock produces induced remanence magnetization that can significantly contribute to the surface magnetic anomalies [*Oufi et al.*, 2002]. The mixture of gabbroic and peridotitic rocks in the source layer can build a complicated magnetic source layer with smaller magnetization values and the process of the lower crust exposure can make a less-coherent magnetic signature than is normal for fast-intermediate spreading rate crust.

Magnetic signatures from such slow and ultraslow spreading environment are low amplitudes and often muted [*Escartin et al.*, 2008]. In the crust of the SWIR, one of the slowest spreading ridges, well-organized crustal accretion, thin crust, and the exposure of plutonic (gabbric/peridotitic) complex are observed [*Hosford et al.*, 2003].

The transition from a rough, basaltic crust to smooth, gabbroic/peridotitic seafloor coincides with decreases in full spreading rates from ~30 to ~14 km/Myr [*Hosford et al.*, 2003; *Sauter et al.*, 2008]. Although anomalies are remarkably precise over the SWIR crust, amplitudes of anomalies over gabbroic/peridotitic seafloor are lower than that of basaltic seafloor. At the modern MAR crust between the Atlantis and Kane fracture zones, the modern spreading center of the same ridge segment that created the AMSZ, where extensive geophysical studies have been carried out, and the crust is observed to contain many ocean core complexes in various stages of growth formed by asymmetrically accreting ridges [*Smith et al.*, 2008]. This crust shows zones with irregular crustal accretion patterns, detachment faults, the exposure of the lower crust, and complex, low-amplitude magnetic signals compared to the young crust elsewhere, characterized by linear, symmetrical spreading [*Escartin et al.*, 2008].

From our analysis, the AMSZ coincides with the slowest spreading rates and low melt supply that is suggested by seismic studies [*Lizarralde et al.*, 2004]. For the evidence of possible lower crustal exposure at the AMSZ, seismic data acquired on the Canary side of the Atlantic shows several detachment faults, suggesting that lower crust exposures possibly occurred within the AMSZ crust between M11-M3 [*Ranero and Reston*, 1999]. We think that the AMSZ crust displays irregular seafloor morphology seafloor flanked by lower crust exposures via detachment faulting similar to the present-day crust with ocean core complexes.

In summary, we propose that the causes of the AMSZ were both geomagnetic field behavior and changes in crustal spreading regime. The contemporaneous low

intensity field with minima during the time of AMSZ contributed to the overall reduction of magnetic anomaly amplitudes over the AMSZ. The observed slowing of spreading rates had two effects: (1) closely-spaced interfering anomalies which reduced anomaly amplitude, and (2) a transition from a magmatic-dominated crustal formation to tectonic extension, producing a thin or absent basaltic layer and the exposure of non-basaltic magnetic source layer through detachment faults.

CHAPTER IV

DETERMINATION OF THE VOLCANOSTRATIGRAPHY OF OCEANIC CRUST FORMED AT SUPER-FAST SPREADING RIDGE: ELECTROFACIES ANALYSES OF ODP/IODP HOLE 1256D*

OVERVIEW

The objective of this study is to construct by electrofacies analyses a representative volcanostratigraphy of Ocean Drilling Program (ODP)/Integrated Ocean Drilling Program (IODP) Hole 1256D, the first complete penetration of intact upper oceanic crust formed at a fast spreading rate. An accurate knowledge of the volcanostratigraphy is vital to understand processes of crustal construction, submarine magmatism, and to estimate chemical exchange with seawater, but this is rarely achieved due to very low rates of core recovery in most basement holes. We used two approaches to determine the rock types that form the wall rocks in the volcanic and intrusive sections of Hole 1256D: (1) user guided interpretations of electrofacies acquired by imaging tools combined with other wire line tools; and (2) the use of an Artificial Neutral Network to objectively classify the responses of all available logging information. The first approach is greatly assisted by the availability of Formation MicroScanner images from

---

*Reprinted with permission from "Determination of the volcanostratigraphy of oceanic crust formed at superfast spreading ridge: Electrofacies analyses of ODP/IODP Hole 1256D" by Tominaga, M., D. A. H. Teagle, J. C. Alt, and S. Umino, *in press*., *Geochemistry Geophysics Geosystems.,* doi:10.1029/2008GC002143, Copyright by American Geophysical Union.

multiple logging passes that provide superior coverage of the borehole wall compared to previous attempts at core-log integration. This has resulted in more confident and detailed lithologic classifications, such as with the distinction between pillows and different styles of breciation. We propose ten lithology types for our new volcanostratigraphy of Hole 1256D: Massive Flows, Ponded Lava, Fractured Massive Flows, Fragmented Flows, Thin flows or thick pillows, Pillows, Breccias, Dikes in dike complex, Isolated Dikes, and Gabbros. Three major lithology types are Massive Flows (both Massive and Fragmented Massive Flow, 22 % in the volcanic section), Fragmented Flows (32 %), and Breccias (19 %). Pillow lavas make up only 1.9% of the volcanic section and are confined to a hundred meter interval. Electrofacies analyses suggest that the lower boundary of the Transition Zone between extrusive and intrusive rocks is located at 1064 mbsf. Beneath this depth, subvertical contacts interpreted to be dike margins are typically observed every 1 to 2 m down hole commonly with brecciated zones along the contacts. The dikes dip steeply (~79°) to the north-east indicating slight rotation away from the ridge axis.

We used an Artificial Neural Network approach to determine a quantitative lithostratigraphy, yielding different results compared to our user-guided interpretive approach. The ANN is most strongly influenced by porosity and alteration degrees and the resulting stratigraphy most closely resembles the above classifications when clustered by FMS-texture as opposed to lithologic interpretation. The ANN thus provides a porosity-based stratigraphy of the basement rather than the traditional lithology-based stratigraphy.

INTRODUCTION

An accurate downhole lithostratigraphy provides the basic foundation for interpreting any section of drilled oceanic crust. However, reconstructing the distribution of rock types downhole remains one of the major challenges to hard rock ocean drilling. This is because core recovery rates in the upper oceanic crust are typically low (<30%) with few long continuous core pieces, and better-drilled rock types (i.e., less fractured rocks) are preferentially recovered. Volcanostratigraphy models derived solely from recovered cores thus only partially represent the basement and are generally strongly biased against more fragile rock types such as highly altered and fractured formations, breccias, and fracture fills. With such low recovery rates, there is significant uncertainty as to the original *in situ* location of the core pieces recovered, so the unrecovered rock formations must be interpolated from the recovered rock types. Consequently, core-based volcanostratigraphic models may lead to erroneous classifications of lithologic types, misinterpretations of crustal construction processes, and inaccurate estimates of seawater-basalt chemical exchange fluxes resulting from hydrothermal alteration [e.g., *Alt and Teagle*, 1999; *Teagle et al.*, 1998, 2003; *Fisher*, 2004; *Nielsen et al.,* 2006]. An alternative to the current approach of developing crustal stratigraphies solely from the recovered cores is essential.

In this study, we present a qualitative electrofacies analysis of *in situ* wire-line logs integrated with observations of the recovered cores to reconstruct an igneous stratigraphy model of the intact upper oceanic crust in Ocean Drilling Program/Integrated Ocean Drilling Program (ODP/IODP) Hole 1256D. We further

investigated quantitative wire-line log analysis through the use of unsupervised Artificial Neural Network (ANN) methods to automatically and objectively construct a quantitative volcanic stratigraphy model. We compare the results of the ANN technique with our qualitative electrofacies analysis to investigate the characteristics of each approach and discuss how we can utilize these qualitative and quantitative analyses to improve the construction of a volcanostratigraphy model. Testing the quantitative approach is important to consider if semi-automated lithostratigraphy modeling immediately at the completion of logging operations onboard is possible and informative. Companion papers will discuss the geological implications of the basement volcanostratigraphy developed here with respect to the accretion of the upper crust at Site 1256, the implications for crustal magnetism, and hydrothermal chemical exchange.

BACKGROUND

Geological Background

ODP/IODP Hole 1256D (6° 44.1' N, 91° 56.1') is located in the Guatemala Basin on the eastern flank of the East Pacific Rise (EPR). Marine magnetic anomalies indicate that the crust was accreted ~15 M.y.-ago during an episode of super-fast spreading (full >220 mm/yr, Figure 21) [*Wilson*, 1996]. The location of Hole 1256D was specifically sited to (1) drill the first continuous section of intact upper oceanic crust down to gabbros, (2) test the correlation between the increasing spreading rate and the

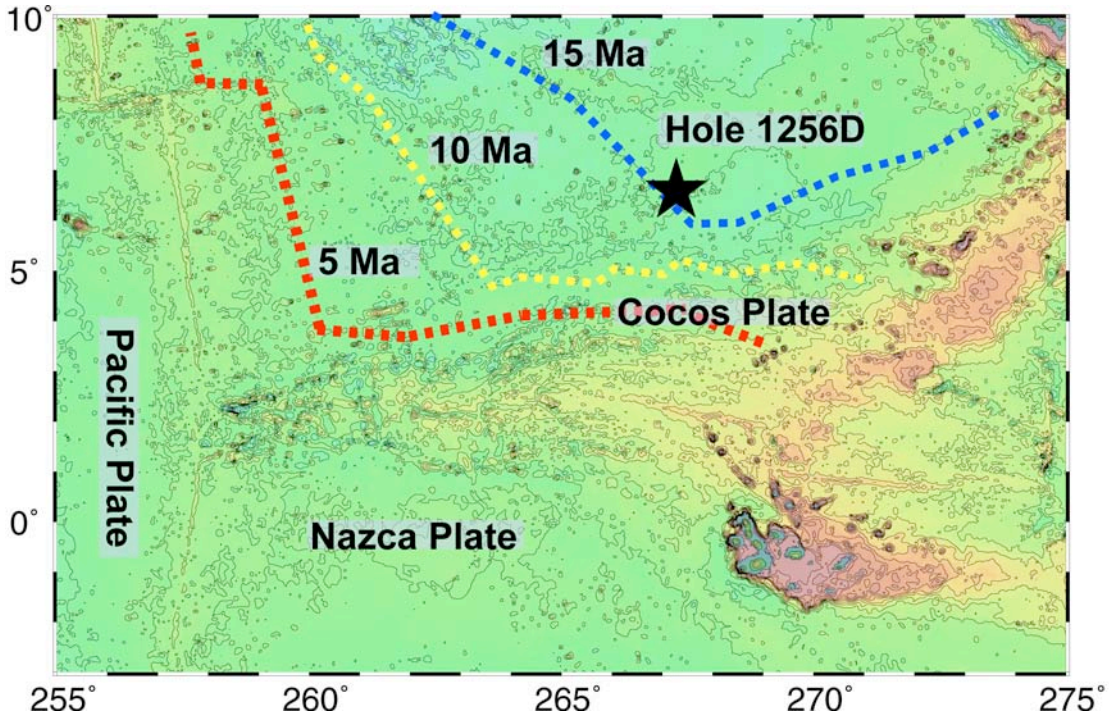

Figure 21. Predicted bathymetry map of the Cocos-Nazca-Pacific region and location of ODP/IODP Hole 1256D (*Smith and Sandwell*, 1997). Red and blue dashed lines indicate 10 and 15 Ma isochrons, respectively.

decreasing depth to the axial low-velocity zones thought to be axial melt lenses and now preserved as gabbros [e.g., *Purdy et al.*, 1992], (3) determine the lithology and structure of the upper oceanic crust from a super-fast spreading rate end-member, (4) examine the seismic and magnetic structure of the upper oceanic crust, and (5) investigate magmatic and alteration processes through intact upper oceanic crust. Drilling at Site 1256 was initiated on ODP Leg 206 [*Teagle et al.*, 2006] and continued on IODP Expeditions 309 and 312 [*Teagle et al.*, 2006]. Hole 1256D now penetrates 1507.1 meters below seafloor (mbsf; 1257 m sub-basement (msb)) with the first gabbroic rocks recovered at 1407

mbsf. The preliminary downhole stratigraphy established from shipboard core observations and wire-line log interpretations onboard revealed that the drilled crust, from top to bottom, consists of (1) lava section that is composed of ponded lavas, inflated flows, sheet flows, and massive flows (751 m), (2) lava-dike transition zone (60 m), (3) sheeted dikes (346 m), and (4) gabbroic rocks intruded into screens of contact metamorphosed dikes (Figure 22).

The uppermost crust is made up of a single >74 m-thick ponded lava flow overlain by thin sheet flows. This thick lava correlates with a 32 m-thick massive lava cored in the neighboring pilot Hole 1256C indicating significant basement topography at the time of eruption. By analogy with observations of the modern EPR [*MacDonald et al.*, 1996] and the need for significant topography to pond such a thickness of lava, this massive flow is interpreted to have solidified 5 to 10 km off axis [*Teagle et al.*, 2006]. The lavas directly underlying the ponded flow display rare sub-vertical hyaloclastite-filled inflation structures, indicative of eruption onto a near horizontal surface [e.g., *Umino*, 2002], and are interpreted to have also solidified off axis. Sheet flows with subordinate massive (>3 m thick) flows make up the bulk of the extrusive section (533.9 to 1004.1 mbsf). Sub-vertical igneous contacts, commonly brecciated and mineralized, are abundant throughout the sheeted dike complex. The lower ~60 m of the sheeted dikes are strongly recrystallized to microcrystalline granoblastic textures through contact metamorphism by underlying gabbro sills. Secondary mineral assemblages indicate very high geothermal gradients (>1500 °C/km) in this region. The plutonic section from 1407

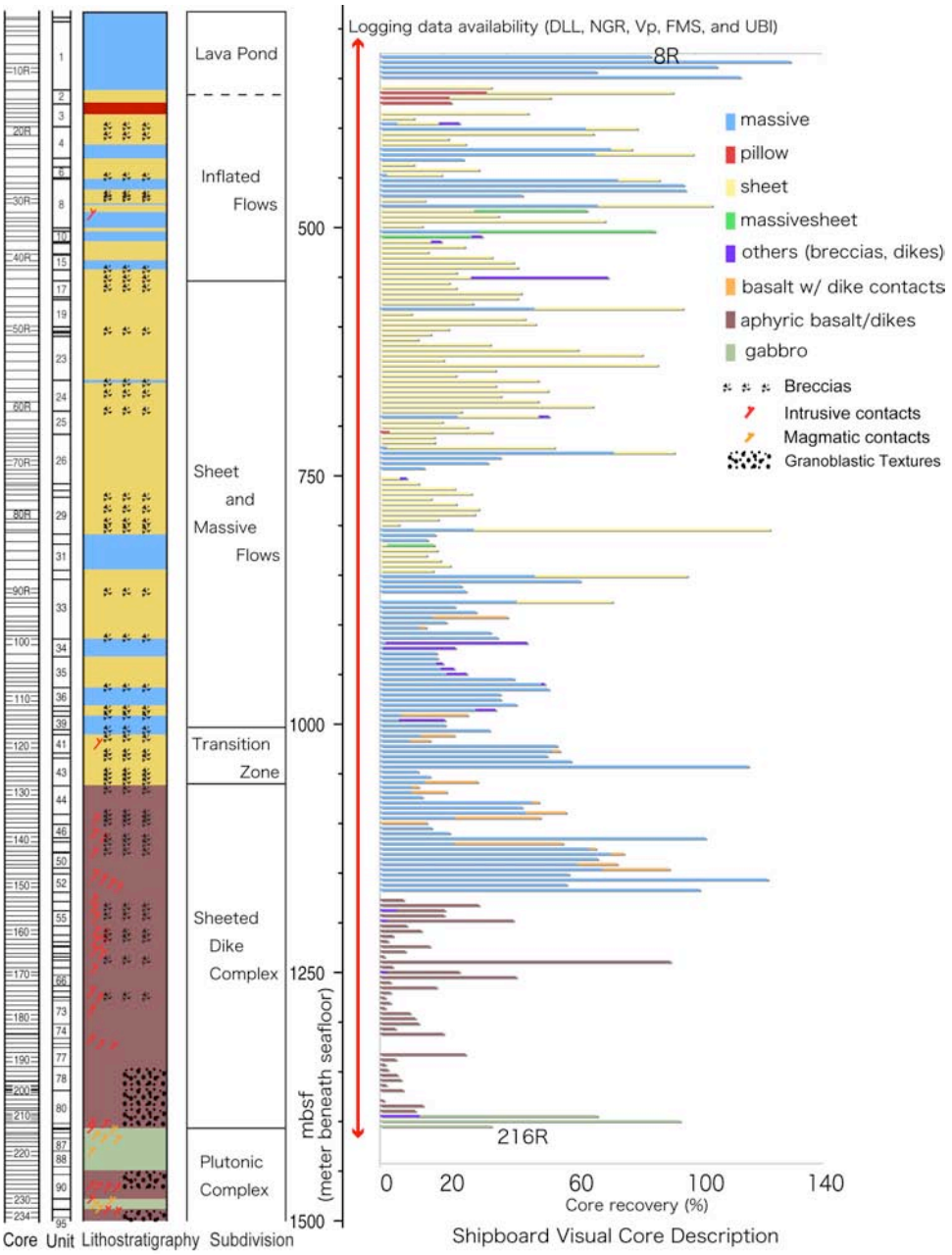

Figure 22. Shipboard summary of Hole 1256D. Left, colored column: Lithological subunits determined aboard by shipboard scientists (*Teagle et al.*, 2006). Sheet flow and sheet-massive flows are distinguished with an arbitrary 3-m cutoff (*Teagle et al.*, 2006). Right, Cumulative occurrences of rock types: Recovery rate (%) in horizontal axis. Each bar corresponds to a recovered core interval for Core 206-1256D-8R to 312-1256D-216R (312-1425 mbsf) with colored bars proportional to the abundance of the material recovered. According to the different rock types recorded in the shipboard visual core descriptions. Core recovery is plotted for basement depths that were logged, and core recovered below the deepest logged section is not plotted. Note that cores with more than 100% recovery may include un-recovered cores drilled in the previous interval. Thick red line shows the region of downhole tool coverage.

mbsf forms the upper portion of a dike-gabbro transition zone and comprises two gabbroic sills 52 and 24 m –thick intruded into a 24 m-thick screen of granoblastically recrystallized dikes. The drilled sequence has normal mid-ocean-ridge basalt composition and is similar to modern EPR basalts [*Wilson et al.*, 2006; *Teagle et al.*, 2006]. The gabbroic rocks recovered to date have chemistries similar to the overlying extrusive rocks and sheeted dikes.

The volcanic section in Hole 1256D has an average recovery rate of 37 % but this is highly variable and includes several intervals with no recovery (Figure 22). Drilling in massive formations provides higher recovery rates (average ~ 50 %) whereas recovery rates in other rock types are typically much lower (Figure 22). The volcanostratigraphy determined onboard during ODP Leg 206, and IODP Expeditions 309 and 312 is based on descriptions of the recovered cores, assuming that these are representative of the basement. Although it is acknowledged that this assumption is most probably incorrect, in the absence of other information, regions of low or no recovery are typically assumed to be similar to the nearest recovered cores.

Core-Log Integration Studies

There have been relatively few attempts to overcome the inherent biases of the core-derived volcanostratigraphy of ODP basement sites through detailed core-log integration [*Bartetzko et al.*, 2002; *Haggas et al.*, 2001; *Haggas et al.*, 2002*; Barr et al.*, 2002; *Revillon et al.*, 2002; *Pockalny and Larson*, 2002; *Bartetzko et al.*, 2003; *Bartetzko et al.*, 2006]. In these studies, core descriptions and *in situ* depths were re-examined and

lithologic classification criteria developed based on response ranges of the wire-line logs and imaging tools. These logging responses were then applied to regions of low and no core recovery to construct a basement stratigraphy. However, these previous studies generally had only limited coverage of the borehole wall due to only single passes by imaging tools, such as the Formation Micro Scanner (FMS) and Ultrasonic Borehole Imager (UBI), making it challenging to differentiate, for example, pillow lavas from highly fractured formations. In contrast, multiple passes of Hole 1256D over the three cruises by the FMS and UBI provide greater coverage of the borehole walls. With a more comprehensive data set from Hole 1256D, a more robust lithostratigraphy can be constructed with much greater confidence than earlier studies.

METHOD

Hole 1256D Logging Operations

Comprehensive wire-line logging programs were conducted following drilling on all three cruises, as well as before the initiation of coring on Expedition 309 (Figure 23). All wire-line logging data were depth-matched and archived by Borehole Research Group of the Lamont-Doherty Earth Observatory (http://iodp.ldeo.columbia.edu/DATA/IODP/index.html). Single and orthogonal caliper measurements show that the Hole 1256D borehole is in generally good condition with few intervals of significant washout (>14 in.). As such, most of the logging data should be reliable [*Williams and Broglia*, 2006]. All types of logs are available for the interval

from 312 to 1425 mbsf that includes the lower part of the ponded lava down to the uppermost gabbros (Figures 22 and 23).

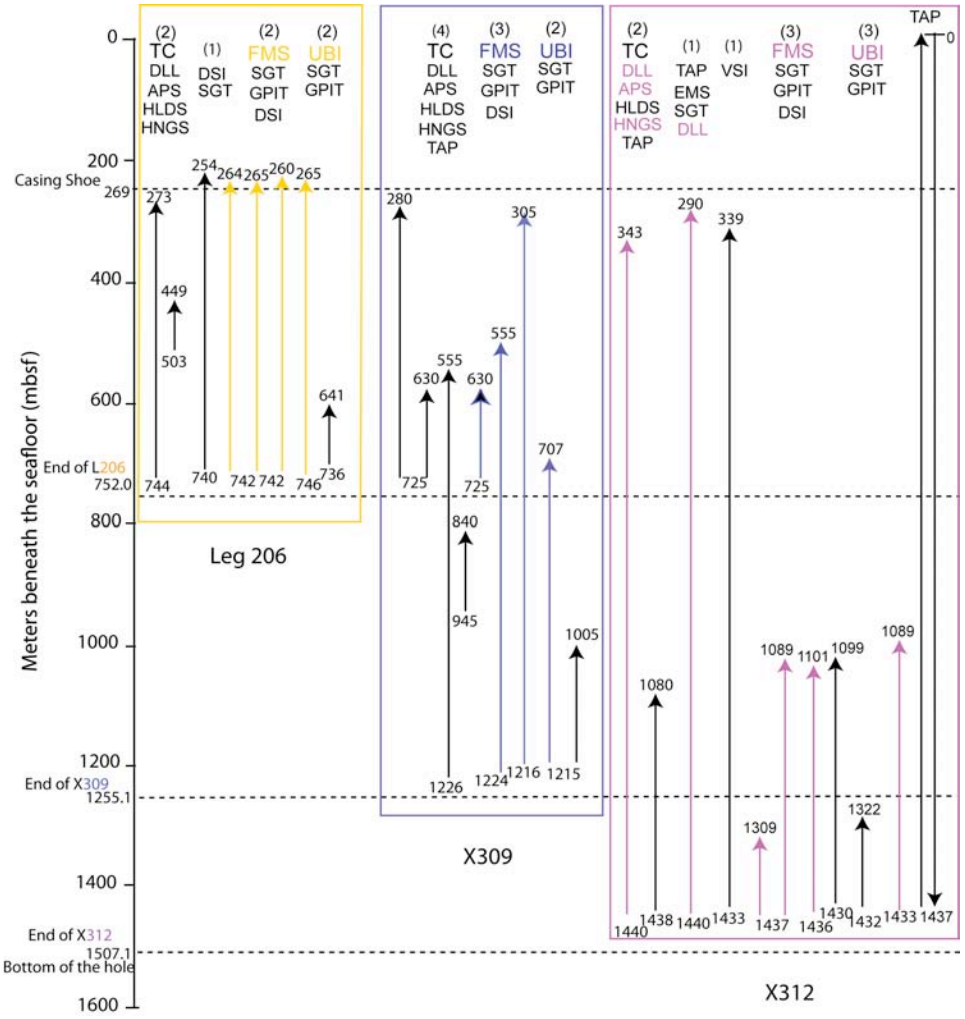

Figure 23. Summary of Leg 206 (yellow), Expedition 309 (blue) and 312 (pink) logging operations. Colored lines and letters indicate wire-line logs that were used in this study. The top and bottom of the logging depth was indicated. Numbers in bracket (1~4) indicate the number of passes. TC = triple combo, HNGS = Hostile Environment Gamma Ray Sonde, APS = Accelerator Porosity Sonde, HLDS = Hostile Environmental Lithodensity Sonde, DLL = Dual Laterolog, TAP = Temperature Acceleration Pressure Tool, SGT = Scintillation Gamma Ray Tool, DSI = Dipole Sonic Imager, GPIT = General Purpose Inclinometer Tool, FMS = Formation MicroScanner, UBI = Ultra Sonic Borehole Imager, VSI = Versatile Seismic Imager, and EMS = Environmental Mechanical Sonde. Parameters used are DLL (LLD and LLS), APS (porosity), HNGS (NGR), DSI (compressional velocity), HLDS (density), and FMS and UBI.

For simplicity, we hereafter distinguish tools that report a single measurement at each depth as 'one dimensional tools', and instruments that record measurements as a function of depth and direction as 'imaging tools'. The former includes the deep and shallow penetration resistivity (Dual LateroLog LLD and LLS), Natural Gamma Ray (NGR), compressional velocity (Vp), density, photoelectric effect factor, and porosity logs. The latter includes: FMS and UBI. Each logging tool measures different *in situ* physical properties and the responses are dependent on and indicative of the different rock types, structures and intensity of alteration present in the borehole walls.

NGR, Vp, density, photoelectric effect factor, and porosity were measured with 0.15~ 0.20 m sampling intervals. NGR counts are acquired even on relatively irregular borehole walls using the Hostile Environment Natural Gamma Ray Sonde [*Rider*, 1996]. NGR provides a measurement of radioactivity of the formation, in particular that resulting from concentrations of K, U, and Th in the wall rock formation. Total gamma and 5-window spectroscopy allows the estimation of individual K, U and Th concentrations. In ocean floor basalts this tool is most sensitive to the presence of potassium-bearing secondary minerals resulting from the low temperature seawater alteration of basalts [e.g., *Revillon et al.*, 2002]. Vp values are acquired by the Dipole Sonic Imager measuring the sonic wave propagation into the rock formation. Density values are acquired by the Hostile Environment Litho-Density Sonde measuring the electron density of rock formations (that is related to the bulk density). This tool also measures photoelectric effect factor values from the occurrence of photoelectric absorption of the gamma rays in rock formations. Because the photoelectric effect factor

depends on the atomic number of the elements in the formation, these values are used to refer the chemical composition of the rock formations [e.g., *Bartetzko et al.*, 2003]. Porosity values are acquired by the Accelerator Porosity Sonde measuring the energy loss of the emitted neutrons.

LLD, LLS, and FMS measure electric current returns (1/resistivity = conductivity) that are sensitive to the porosity structure and cation exchange capacity of the formation [*Pezard*, 1990]. The electric current from Dual Laterolog tool penetrates ~0.5 m into the wall rock and returns to detectors on the tool strings. The detection range of resistivity by LLD and LLS is from 0.2 to 40,000 ohm•m and measurements are carried out typically with 0.15-0.2 m sampling intervals. In contrast, the FMS tool has four orthogonal pads each with 16 sensor buttons that when extended provide partial but significant lateral coverage of the borehole wall (up to 40 % with four orthogonal pads in 8 in. borehole) with high spatial resolution (~0.002 m) resistivity readings. The resulting FMS data provide high-resolution resistivity images of the borehole wall. UBI measures the acoustic reflections from borehole wall with 360° coverage, and provides a visualization of the borehole wall reflectivity as two-dimensional images with a sampling resolution of ~0.15 m. Both the FMS and UBI images are azimuthally oriented to the geographic reference frame using the General Purpose Inclinometer Tool. The FMS and UBI *in situ* physical property measurements essentially provide "scanned-images" of the borehole wall that are of great help for determining the morphology of the basement formations penetrated. In Hole 1256D, multiple FMS runs provide significant intervals with non-overlapping pad traces providing increased lateral

coverage of the borehole wall compared to a single pass. The vertical distribution of non-overlapped pad traces by four-, eight-, and twelve pads downhole is 35, 45, and 20 %, respectively. The multiple passes of the FMS in Hole 1256D result in the FMS logging operation yielding greater than 40 to 60% lateral coverage (as high as 216°) for that over 65% of the logged interval.

The extreme contrast between the highly conductive seawater in the borehole and highly resistive gabbroic rocks led to saturation of the wire-line resistivity tools (> 4.6 Log-ohm/m; e.g., ODP Leg 176 logging summary). As such the occurrence of gabbroic rocks remains as determined from the core descriptions at the curatorial depth of 1407 mbsf. We await further drilling and logging of Hole 1256D to provide better wire-line log data to characterize the plutonic section of Hole 1256D.

Logging Data Collection

After we closely examined all the wire-line logging data from Hole 1256D collected on ODP Leg 206, and IODP Expeditions 309 and 312, we used FMS and UBI images, LLD, LLS and NGR as primary, and density, Vp, photoelectric effect factor and porosity as secondary parameters to classify rock and flow types in the electrofacies analysis. We found that the combination of the primary wire-line log parameters with the FMS images provides the most distinctive signatures for different rock formations. The secondary wire-line parameters are useful for detailed chemical composition-rock type determination [e.g., *Bartetzko et al.*, 2003]. However, a preliminary examination of all the wireline data from Hole 1256D indicated that the crust is highly fragmented.

Such formations mean that wireline tool responses of these secondary parameters are strongly influenced by the presence of fluid (including hydrogen bounds in altered rocks) or the quality of contact with the borehole wall. Because of these *in situ* conditions, we have given these secondary parameters less weight in our electrofacies analysis. Instead we have used the resistivity logs as an alternative and more representative recorder of the information provided by the density, Vp, photoelectric effect factor, and porosity data because resistivity is some, albeit unknown function of the local porosity structure and the rock formation [e.g., *Pezard*, 1990].

FMS and UBI images were re-plotted by using a 2 m window for dynamic calculation onto the depth matched values at the Borehole Research Group, University of Leicester and at the Institute for Frontier Research on Earth Revolution, Japan Agency for Marine-Earth Science and Technology. FMS images can be displayed with either static or dynamic normalization. Static normalization computes the relative contrast in resistivity over the entire logged interval so that absolute values can be comparable downhole. For dynamic normalization, resistivity contrasts are compared within designated short intervals and this approach has been utilized in our analysis because this more strongly emphasizes local contrasts of conductive features. The UBI images are strongly influenced by the hole condition and were mostly utilized to check the locations and appearances of major features on the FMS images.

Core-Log Correlation and Qualitative Electrofacies Analysis

High- resolution FMS images (.tiff format) were acquired using the GeoFrame^{TM}

software and the borehole was subdivided into 50 m intervals for printing onto 36 x 48 inch paper together with the depth-matched LLD, LLS, NGR, FMS and caliper logs to enable the "mapping" of the downhole geology. These plotted images when combined with images on GeoFrame were found to be an efficient method of electrofacies analysis as this allowed the complete stratigraphy to be assessed simultaneously and the responses of similar rock types from different intervals to be readily compared.

First, we identified flow boundaries, distinctive conductive fractures, and sub-vertical contacts using the FMS and UBI images. The lithology of the units between these boundaries was then determined based on the morphologies of the borehole walls as observed from the FMS and UBI images, the ranges of LLD, LLS, and NGR responses, and nature of the recovered core pieces. The FMS caliper measurement was carefully monitored because irregularities in the borehole walls can interfere with resistivity responses.

Next, we investigated the correlation between recovered core pieces and observations on logging interpretation. The preliminary inspection of the FMS images provided us with broad clues to match recovered cores and unrecovered intervals with corresponding rock types. Continuous core pieces are typically only recovered from intervals of homogeneous, slightly altered, massive lavas. We tried to establish the *in situ* depths of recovered continuous core pieces (approximately > 8 cm) by comparing the depths of intervals assumed to be massive flows based on their relatively homogeneous textures on the FMS images with the curatorial depths of continuous core pieces. In some cases, the recovered continuous core pieces can be unambiguously

assigned to the depth of the massive lavas observed on FMS images, and then neighboring core pieces can be assigned depths by considering their juxtaposition with respect to the massive lava intervals. One might think that FMS or UBI images may readily be used to relocate brecciated pieces to appropriate fragmented intervals identified. However, the relocation of individual pieces is extremely challenging even when there are distinctive features in cores such as veins and fractures. This is principally due to very low recovery rates in such intervals and the large distance between the exterior of the recovered cores and the borehole walls (>10 cm). We also examined the onboard physical property measurements on the recovered cores (i.e., magnetic susceptibility, gamma-ray attenuation porosity, wet bulk density, and natural gamma emission measured by Multisensor Track) to see how these physical property measurements help us to match core observations to wire-line logs. We found that, however, these cores and the measured values represent only limited aspects of the *in situ* bulk formation because the core recovery rates are so low and recovered core types are strongly biased. Following examination of the complete section, the curatorial depths and the logger's depths were generally found to be no more than a few meters difference in Hole 1256D (Appendix D).

Lastly, we have finalized the classification of lithofacies principally based on wire-line logs. These lithofacies classifications are named after rock formation textures on the FMS images. Classifying flow types in a volcanostratigraphy model based on electrofacies analyses relies on criteria that are somewhat different from those for identifications based on observations of surficial lava morphology from underwater

vehicles [e.g., *Umino et al.*, 2000]. In electrofacies analyses one observes a cross-section of the accumulated lava flows as represented by resistivity contrasts. Following this approach, we can generally identify lava as either as a massive flow, pillow lava, a fragmented interval, or some form of physically altered, fragmented flows.

RESULTS

Hole 1256D Qualitative Volcanostratigraphy

A new igneous stratigraphy of Hole 1256D from 312 to 1425 mbsf is proposed (Figure 24, Table 4) and the characteristic parameters for recognizing each electrofacies are summarized in Table 5. We suggest ten lithofacies: Massive Flows, Massive Off-Axis Ponded Lava, Fractured Massive Flows, Thin Flows/Thick Pillows, Pillows, Fragmented Flows, Breccias, Isolated Dikes, Dikes in Sheeted Dike Complex, and Gabbros.

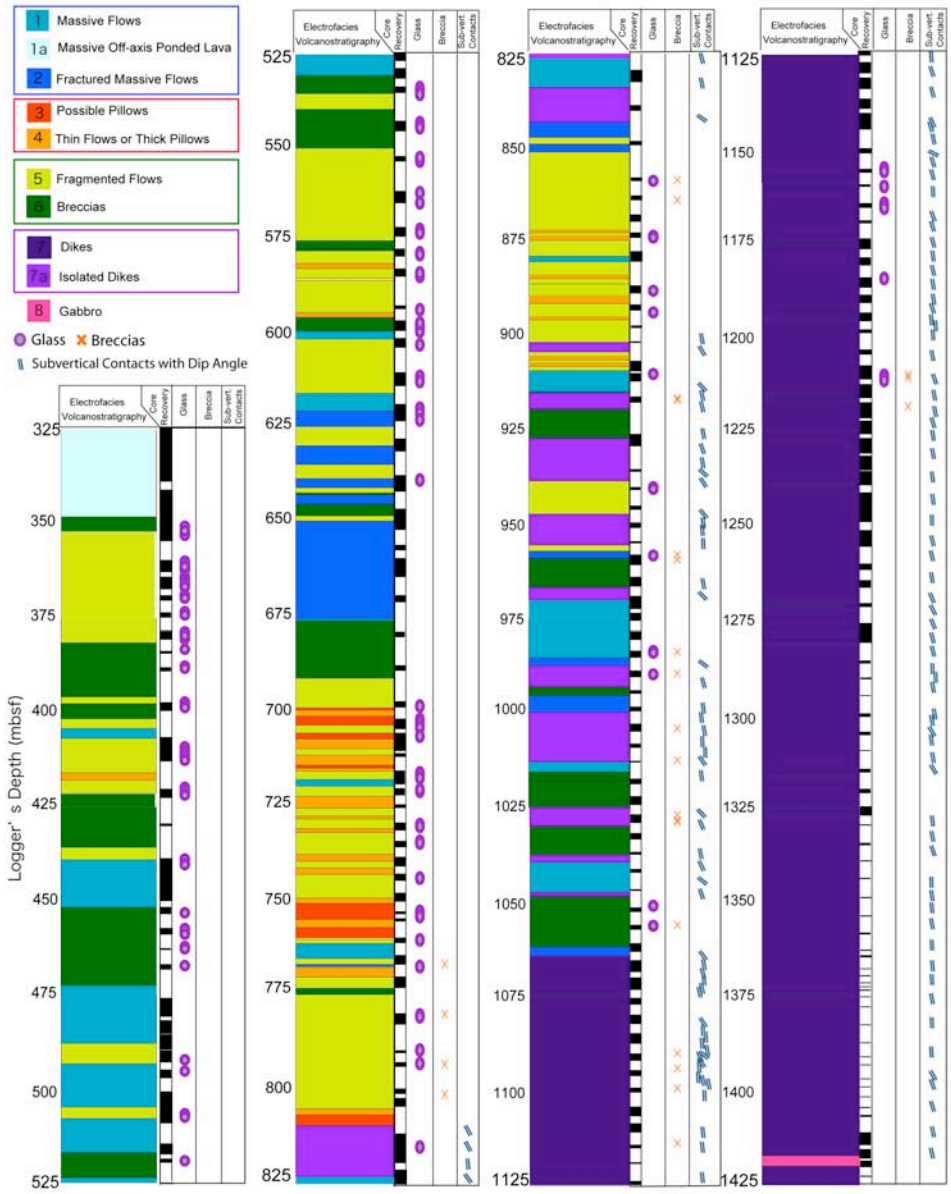

Figure 24. Complete igneous stratigraphy of ODP/IODP Hole 1256D crust. Colored column show the sequence of electrofacies, and these color codes for 10 lithologies are indicated at the left side of the panel. For simplicity, blue colors summarize the intervals of "massive" textures, red colors summarize pillows or thin flows, green colors indicate fragmented intervals, purple colors indicate dikes, and a pink color indicates gabbros. For volcanostratigraphy, logging depth is used. The columns of black and white stripe show core recovery rates (black = recovered) that are shown with using curatorial (drilling) depth. Curatorial depths of recovered glass and breccias, and observed subvertical contacts are shown. Note that the recovered intervals are all pushed up to the top of cored interval.

Massive Flows, Fractured Massive Flows, and Fragmented Flows are the dominant lithofacies in the extrusive sequences and make up approximately 13, 5, and 23 %, respectively, of the complete section (Table 6). Pillow Lavas make up only 1.4 % of our new stratigraphy and are confined to a number of 0.5 - 3 m-thick intervals between between 700 and 810 mbsf. The pillow zone between 364 and 388 mbsf identified by shipboard scientists is re-interpreted as a zone of Fragmented Flows and Breccias. Isolated Dikes and Dikes in sheeted dike complex make 12 and 28 %, respectively, of the new stratigraphy and include some brecciated zones with discernible sub-vertical contacts.

Our new volcanostratigraphy exhibits significant differences in the fractions of breccias and sheet flows compared to the shipboard stratigraphy (Figure 25). This discrepancy clearly indicates that core recovery is highly biased towards better drilled, massive, less fractured rocks.

Table 4. Electrofacies

top	bottom	Flow	top	bottom	Flow	top	bottom	Flow	top	bottom	Flow	top	bottom	Flow
312.12	348.02	MOPL	477.72	482.96	MAS	615.15	617.06	MAS	703.02	703.73	FF	757.20	758.57	P
348.02	351.98	BR	482.96	488.00	MAS	617.06	617.84	MAS	703.73	704.37	FF	758.57	759.51	P
351.98	353.33	FF	488.00	493.43	FF	617.84	619.85	MAS	704.37	705.14	FF	759.51	759.96	TP
353.33	354.06	FF	493.43	503.54	MAS	619.85	620.80	FMAS	705.14	706.66	P	759.96	761.02	FF
354.06	355.37	FF	503.54	504.92	MAS	620.80	621.36	FMAS	706.66	707.60	TP	761.02	762.14	MAS
355.37	358.04	FF	504.92	506.81	FF	621.36	622.53	FMAS	707.60	708.28	TP	762.14	763.76	MAS
358.04	361.95	FF	506.81	507.95	FF	622.53	623.99	FMAS	708.28	709.29	TP	763.76	765.00	MAS
361.95	364.44	FF	507.95	517.00	MAS	623.99	624.92	FF	709.29	710.98	FF	765.00	765.27	FF
364.44	369.00	FF	517.00	523.66	BR	624.92	625.26	FF	710.98	712.60	TP	765.27	766.55	FF
369.00	373.00	FF	523.66	524.55	MAS	625.26	626.30	FF	712.60	713.02	TP	766.55	767.18	TP
373.00	377.00	FF	524.55	530.57	MAS	626.30	629.00	FF	713.02	713.64	TP	767.18	767.45	FF
377.00	381.43	FF	530.57	535.39	BR	629.00	632.11	FMAS	713.64	714.38	P	767.45	769.38	TP
381.43	383.29	BR	535.39	536.89	FF	632.11	633.99	FMAS	714.38	715.17	TP	769.38	769.96	TP
383.29	384.64	BR	536.89	539.58	FF	633.99	635.29	FF	715.17	715.36	FF	769.96	770.60	FF
384.64	386.02	BR	539.58	542.31	BR	635.29	637.72	FF	715.36	715.53	FF	770.60	771.00	FF
386.02	386.99	BR	542.31	543.91	BR	637.72	638.63	FMAS	715.53	716.57	FF	771.00	772.04	FF
386.99	389.00	BR	543.91	547.00	BR	638.63	640.16	FMAS	716.57	717.45	FF	772.04	772.46	FF
389.00	389.90	BR	547.00	549.88	BR	640.16	641.53	FF	717.45	718.50	MAS	772.46	772.92	FF
389.90	390.69	BR	549.88	554.00	FF	641.53	642.00	BR	718.50	719.19	MAS	772.92	774.76	BR
390.69	392.24	BR	554.00	557.08	FF	642.00	644.49	FMAS	719.19	720.00	FF	774.76	775.16	FF
392.24	393.16	BR	557.08	561.39	FF	644.49	646.70	BR	720.00	721.91	FF	775.16	776.67	FF
393.16	395.81	BR	561.39	564.89	FF	646.70	647.63	BR	721.91	723.12	TP	776.67	778.29	FF
395.81	397.58	FF	564.89	568.87	FF	647.63	649.00	FF	723.12	724.05	TP	778.29	780.84	FF
397.58	399.00	BR	568.87	570.78	FF	649.00	650.74	FMAS	724.05	725.07	TP	780.84	781.37	FF
399.00	399.96	BR	570.78	574.46	FF	650.74	652.21	FMAS	725.07	726.56	FF	781.37	783.04	FF
399.96	401.60	BR	574.46	577.29	BR	652.21	653.72	FMAS	726.56	727.18	FF	783.04	784.09	FF
401.60	402.12	FF	577.29	579.52	FF	653.72	655.32	FMAS	727.18	727.95	TP	784.09	785.10	FF
402.12	404.16	FF	579.52	580.66	FF	655.32	655.77	FMAS	727.95	729.31	FF	785.10	786.47	FF
404.16	406.78	MAS	580.66	582.02	TP	655.77	658.13	FMAS	729.31	730.46	FF	786.47	790.67	FF
406.78	407.75	FF	582.02	583.29	FF	658.13	659.84	FMAS	730.46	731.59	TP	790.67	795.04	FF
407.75	409.79	FF	583.29	584.55	FF	659.84	664.57	FMAS	731.59	737.33	FF	795.04	796.11	FF
409.79	411.21	FF	584.55	585.20	TP	664.57	668.47	FMAS	737.33	737.90	TP	796.11	797.12	FF
411.21	411.99	FF	585.20	585.56	FF	668.47	670.74	FMAS	737.90	738.16	TP	797.12	800.29	FF
411.99	413.38	FF	585.56	585.93	FF	670.74	671.54	FMAS	738.16	739.17	TP	800.29	801.96	FF
413.38	415.94	FF	585.93	587.92	FF	671.54	675.60	FMAS	739.17	739.96	FF	801.96	802.71	FF
415.94	417.93	TP	587.92	593.67	FF	675.60	677.71	BR	739.96	740.97	FF	802.71	805.05	FF
417.93	421.41	FF	593.67	594.95	TP	677.71	679.61	BR	740.97	741.85	TP	805.05	806.73	TP
421.41	435.73	BR	594.95	595.89	BR	679.61	682.36	BR	741.85	742.69	TP	806.73	809.58	P
435.73	439.00	FF	595.89	598.62	BR	682.36	683.51	BR	742.69	745.35	FF	809.58	815.95	MAS
439.00	451.66	MAS	598.62	600.71	MAS	683.51	684.72	BR	745.35	745.78	FF	815.95	817.51	ID
451.66	456.09	BR	600.71	604.03	FF	684.72	686.81	BR	745.78	746.64	FF	817.51	823.21	ID
456.09	461.02	BR	604.03	605.05	FF	686.81	687.03	BR	746.64	747.09	FF	823.21	823.52	ID
461.02	465.06	BR	605.05	607.93	FF	687.03	687.48	BR	747.09	748.93	FF	823.52	826.17	ID
465.06	466.53	BR	607.93	609.17	FF	687.48	689.44	BR	748.93	749.45	TP	826.17	828.26	MAS
466.53	467.56	BR	609.17	610.16	FF	689.44	690.52	BR	749.45	750.39	TP	828.26	829.11	MAS
467.56	468.20	BR	610.16	611.46	FF	690.52	698.42	FF	750.39	754.61	P	829.11	833.90	MAS
468.20	471.56	BR	611.46	612.67	FF	698.42	699.13	P	754.61	755.53	TP	833.90	843.23	ID
471.56	472.45	BR	612.67	614.36	FF	699.13	700.61	TP	755.53	756.78	TP	843.23	845.86	FMAS
472.45	477.72	MAS	614.36	615.15	FF	700.61	703.02	P	756.78	757.20	P	845.86	847.23	FMAS

Table 4. Continued.

top	bottom	Flow	top	bottom	Flow	top	bottom	Flow	top	bottom	Flow	top	bottom	Flow
847.23	847.66	FF	943.93	944.80	FF	1063.71	1066.15	VD	1239.44	1243.28	VD			
847.66	848.07	FF	944.80	945.19	FF	1066.15	1067.83	VD	1243.28	1250.67	VD			
847.66	848.98	FF	945.19	945.75	FF	1067.83	1072.82	VD	1250.67	1256.77	VD			
848.98	850.46	FMAS	945.75	947.00	FF	1072.82	1073.22	VD	1256.77	1261.44	VD			
850.46	851.09	FMAS	947.00	949.79	ID	1073.22	1073.55	VD	1261.44	1266.40	VD			
851.09	857.67	FF	949.79	951.77	ID	1073.55	1080.08	VD	1266.40	1270.39	VD			
857.67	859.68	FF	951.77	955.22	ID	1080.08	1080.33	VD	1270.39	1272.63	VD			
859.68	860.70	FF	955.22	956.82	FF	1080.33	1085.56	VD	1272.63	1278.45	VD			
860.70	862.07	FF	956.82	957.81	FMAS	1085.56	1085.68	VD	1278.45	1281.11	VD			
862.07	865.18	FF	957.81	958.71	FMAS	1085.68	1089.29	VD	1281.11	1282.64	VD			
865.18	869.23	FF	958.71	961.03	BR	1089.29	1091.63	VD	1282.64	1285.52	VD			
869.23	871.75	FF	961.03	962.09	BR	1091.63	1093.35	VD	1285.52	1288.66	VD			
871.75	872.48	TP	962.09	964.25	BR	1093.35	1093.99	VD	1288.66	1298.56	VD			
872.48	873.32	FF	964.25	966.46	BR	1093.99	1094.94	VD	1298.56	1301.10	VD			
873.32	874.50	TP	966.46	969.77	ID	1094.94	1098.10	VD	1301.10	1305.47	VD			
874.50	878.64	FF	969.77	971.54	MAS	1098.10	1104.44	VD	1305.47	1308.82	VD			
878.64	880.11	MAS	971.54	975.68	MAS	1104.44	1106.90	VD	1308.82	1314.02	VD			
880.11	883.61	FF	975.68	979.24	MAS	1106.90	1112.72	VD	1314.02	1316.58	VD			
883.61	884.56	TP	979.24	981.72	MAS	1112.72	1115.55	VD	1316.58	1327.06	VD			
884.56	885.98	FF	981.72	983.57	MAS	1115.55	1118.76	VD	1327.06	1329.71	VD			
885.98	886.00	TP	983.57	985.26	MAS	1118.76	1123.94	VD	1329.71	1332.38	VD			
886.00	889.11	FF	985.26	985.77	FMAS	1123.94	1125.84	VD	1332.38	1342.41	VD			
889.11	890.09	TP	985.77	986.50	FMAS	1125.84	1130.87	VD	1342.41	1347.63	VD			
890.09	891.20	TP	986.50	987.33	FMAS	1130.87	1136.36	VD	1347.63	1353.46	VD			
891.20	894.68	FF	987.33	992.96	ID	1136.36	1140.25	VD	1353.46	1357.13	VD			
894.68	895.53	TP	992.96	995.25	BR	1140.25	1143.19	VD	1357.13	1360.78	VD			
895.53	899.22	FF	995.25	996.36	FMAS	1143.19	1147.00	VD	1360.78	1365.09	VD			
899.22	901.47	FF	996.36	999.15	FMAS	1147.00	1155.14	VD	1365.09	1369.51	VD			
901.47	904.01	ID	999.15	999.69	FMAS	1155.14	1158.97	VD	1369.51	1371.00	VD			
904.01	905.11	FF	999.69	1002.66	ID	1158.97	1160.94	VD	1371.00	1375.54	VD			
905.11	906.11	TP	1002.66	1004.67	ID	1160.94	1163.62	VD	1375.54	1379.15	VD			
906.11	906.89	FF	1004.67	1007.96	ID	1163.62	1170.13	VD	1379.15	1382.00	VD			
906.89	907.84	TP	1007.96	1011.68	ID	1170.13	1173.03	VD	1382.00	1390.11	VD			
907.84	908.99	FF	1011.68	1017.84	ID	1173.03	1176.23	VD	1390.11	1393.00	VD			
908.99	910.85	MAS	1017.84	1027.85	ID	1176.23	1178.98	VD	1393.00	1398.69	VD			
910.85	912.40	MAS	1027.85	1029.39	ID	1178.98	1181.25	VD	1398.69	1409.44	VD			
912.40	914.51	MAS	1029.39	1031.70	BR	1181.25	1186.00	VD	1409.44	1410.94	VD			
914.51	914.84	BR	1031.70	1033.82	BR	1186.00	1188.45	VD	1411.00	1417.25	VD			
914.84	919.23	ID	1033.82	1034.44	BR	1188.45	1194.65	VD	1417.25	1419.99	VD			
919.23	920.68	ID	1034.44	1036.16	BR	1194.65	1196.17	VD	1419.99	1423.00	VD			
920.68	922.63	BR	1036.16	1037.08	BR	1196.17	1201.26	VD	1423.00	1425.00	VD			
922.63	923.54	BR	1037.08	1038.10	MAS	1201.26	1208.41	VD						
923.54	926.88	BR	1038.10	1038.91	MAS	1208.41	1215.39	VD						
926.88	930.37	ID	1038.91	1045.25	ID	1215.39	1217.49	VD						
930.37	931.87	ID	1045.25	1046.88	ID	1217.49	1219.63	VD						
931.87	935.68	ID	1046.88	1047.91	ID	1219.63	1223.38	VD						
935.68	938.22	ID	1047.91	1058.07	BR	1223.38	1227.80	VD						
938.22	938.82	FF	1058.07	1061.37	BR	1227.80	1235.32	VD						
938.82	943.93	FF	1061.37	1063.71	FMAS	1235.32	1239.44	VD						

Table 5. Parameters in each lithofacies for qualitative volcanostratigraphy

Lithofacies	Primary Parameters			FMS/UBI Criteria	Secondary Parameters			
	LogLLD	LogLLS	NGR		Den.	Poro.	Vp	PEF
1 Massive Flows	2.0±0.3	2.0±0.3	2.6±0.8	>2 m thick, with almost no developed fractures resulting in featureless, homogeneous textures.	2.9±0.3	8.5±5.8	5.7±0.4	3.9±1.0
1a Massive Off-Axis Ponded Lava	1.9±0.2	1.7±0.2	2.6±1.3	Homogeneous texture, subordinate fractures.	2.9±0.6	6.7±1.8	5.7±0.3	4.5±0.7
2 Fractured massive Flows	1.6±0.2	1.6±0.2	3.8±1.3	Less homogeneous texture due to some fracture development, >2 m thick.	2.8±0.2	12.3±6.0	5.4±0.4	3.7±0.7
3 Pillow Lavas	1.6±0.2	1.5±0.2	4.4±1.1	An oval to subround outline with radial fracture inside, associated with altered inter-pillow materials showing high conductivity.	2.8±0.3	16.4±6.9	5.2±0.3	3.3±0.8
4 Thin Flows or Thick Pillows	1.6±0.2	1.6±0.2	4.3±1.3	Similar to homogeneous texture in massive flows disturbed by distinctive flow boundaries or horizontal fratures, < 2m thick.	2.7±0.3	17.2±9.2	5.2±0.4	3.3±0.9
5 Fragmented Flows	1.4±0.3	1.4±0.3	5.7±2.8	Brecciated and develop meshy fractures but individual blocks are only slightly displaced each other, thickness vary.	2.6±0.3	24.8±13.3	4.9±0.5	2.8±0.8
6 Breccias	1.2±0.3	1.0±0.3	4.9±2.0	Completely fragmented, no morphology preservation, the mixture of extremely fine high and low FMS conductivity patches	2.5±0.4	37.7±23.1	4.8±0.8	2.6±0.8
7a Isolated Dikes	1.8±0.3	1.6±0.4	2.3±1.0	Distinguished by highly conductive, steep dip fractures, most likely representing intrusive contacts against the host extrusive rocks.	2.6±0.4	20.2±18.7	5.6±0.4	2.8±1.1
7 Dikes	2.6±0.6	2.3±0.4	4.3±1.3	Recognized by subpararell, subvertical fractures spaced ~ 0.6 m apart, indicating dike contacts.	2.9±0.1	7.3±4.3	5.8±0.3	2.9±0.2
8 Gabbro	NaN	NaN	2.8±0.4	(data only available from cores)	2.9±0.0	2.9±0.4	6.5±0.1	2.9±0.0

Units are LogLLD and LogLLS in ohm•m, NGR in API counts, Den (Density) = g/cm^3 , Poro (Porosity) = %, Vp (compressional velocity) = m/s, PEF (Photoelectric Factor) = barns/e$^-$. Note that both primary and secondary parameters are calculated from wire-line log during Expedition 312 (see Figure. 3)

Table 6. Summary of the new volcanostratigraphy model (325-1425 mbsf)

Lithology	**Whole Hole %**	**Volcanic Section %**
Massive Flows	10.29	14.3
Ponded Lava	3.23	4.5
Fractured massive Flows	5.17	7.2
Fragmented flows	23.11	32.1
Thin flows or thick pillows	3.42	4.8
Pillows	1.36	1.9
Breccias	13.26	18.6
Dikes in Dike Complex	28.01	
Isolated Dikes	11.93	16.6
Gabbros	0.25	

Proportion of each lithofacies with respect to entire examined depth 325- 1425 mbsf (left) and to only volcanic section (325-1064 mbsf).

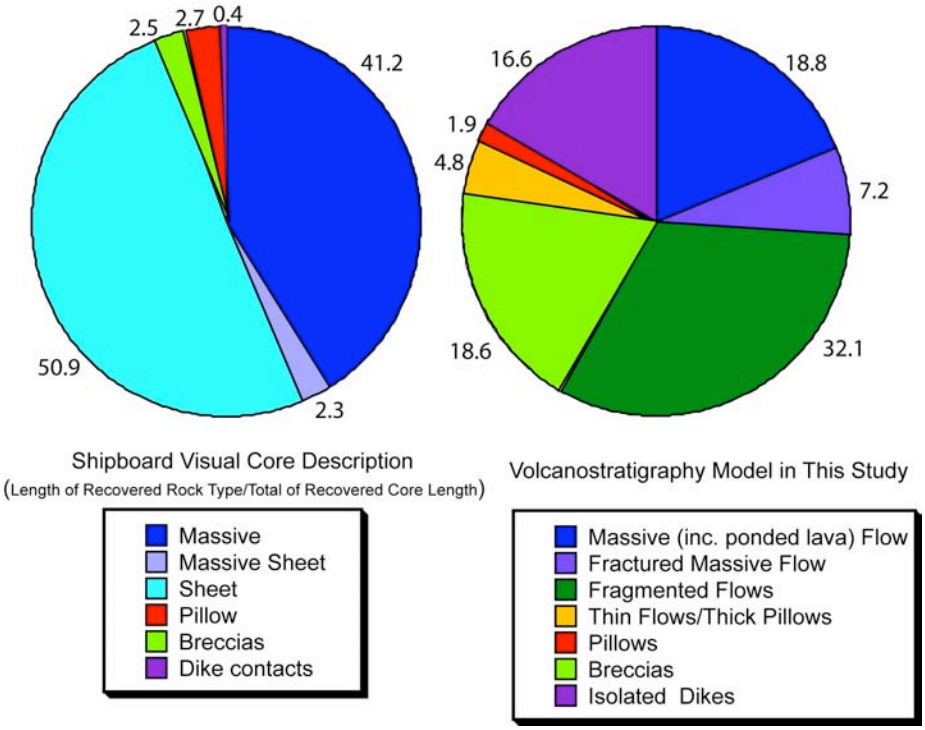

Figure 25. Comparison of rock types in the volcanic section suggested between the shipboard (left) and electrofacies-based (right) igneous stratigraphy. The fraction of each rock type in the shipboard lithostratigraphy was derived from visual core descriptions from Leg 206, Expedition 309 and 312 by calculating a total of recovered core length of a rock type divided by a total of recovered core length. The fraction of each rock type in the electrofacies-based stratigraphy is also shown in Table 3.

Massive Flows

We identified Massive Flows as intervals more than 2 m thick with a homogeneous texture on the FMS and UBI images. These Massive Flows are mainly located between 430 - 530 mbsf and 825-1050 mbsf. Irregularly spaced minor fractures with various orientations are common in these flows. LLD and LLS measurements are typically as high as 1.6±0.4 Log-ohm•m due to the homogeneous texture and with slightly lower values near fractures. NGR counts are relatively low (4.2±2.3 API; Figure 26, Table 5).

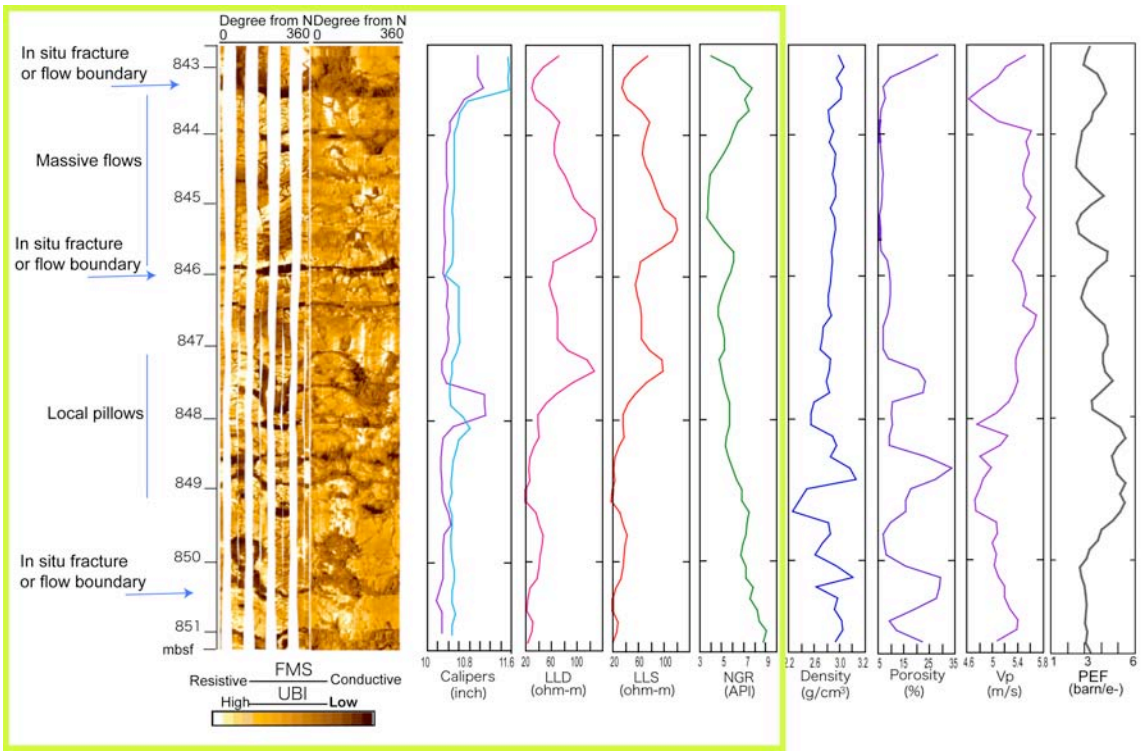

Figure 26. Example of electrofacies analyses over the interval 842- 852 mbsf. These boundaries are listed as lithological boundaries in the table on pages 100-101. FMS and UBI sampling interval were 0.002 and 0.15 m, respectively, and the plot is derived from a dynamically processed 2 m window in GeoFrame. PEF = Photoelectric effect Factor.

Massive Off-axis Ponded Lava

The Massive Off-axis Ponded Lavas, that construct the upper ~100 m of basement in Hole 1256D, are sub-divided from the Massive Flows. Although their electrofacies characteristics are similar, there are strong geological and geophysical criteria for their recognition as a distinctive subgroup [*Teagle et al.*, 2006)] and relatively high core recovery rates give confidence in the shipboard descriptions. LLD and LLS measurements are high 1.9±0.2 Log-ohm•m compared to other electrofacies in

the extrusive section, indicating low porosity structure. NGR counts are low (2.6±1.3 API), indicating relatively few fractures in this formation (Figure 27, Table 5).

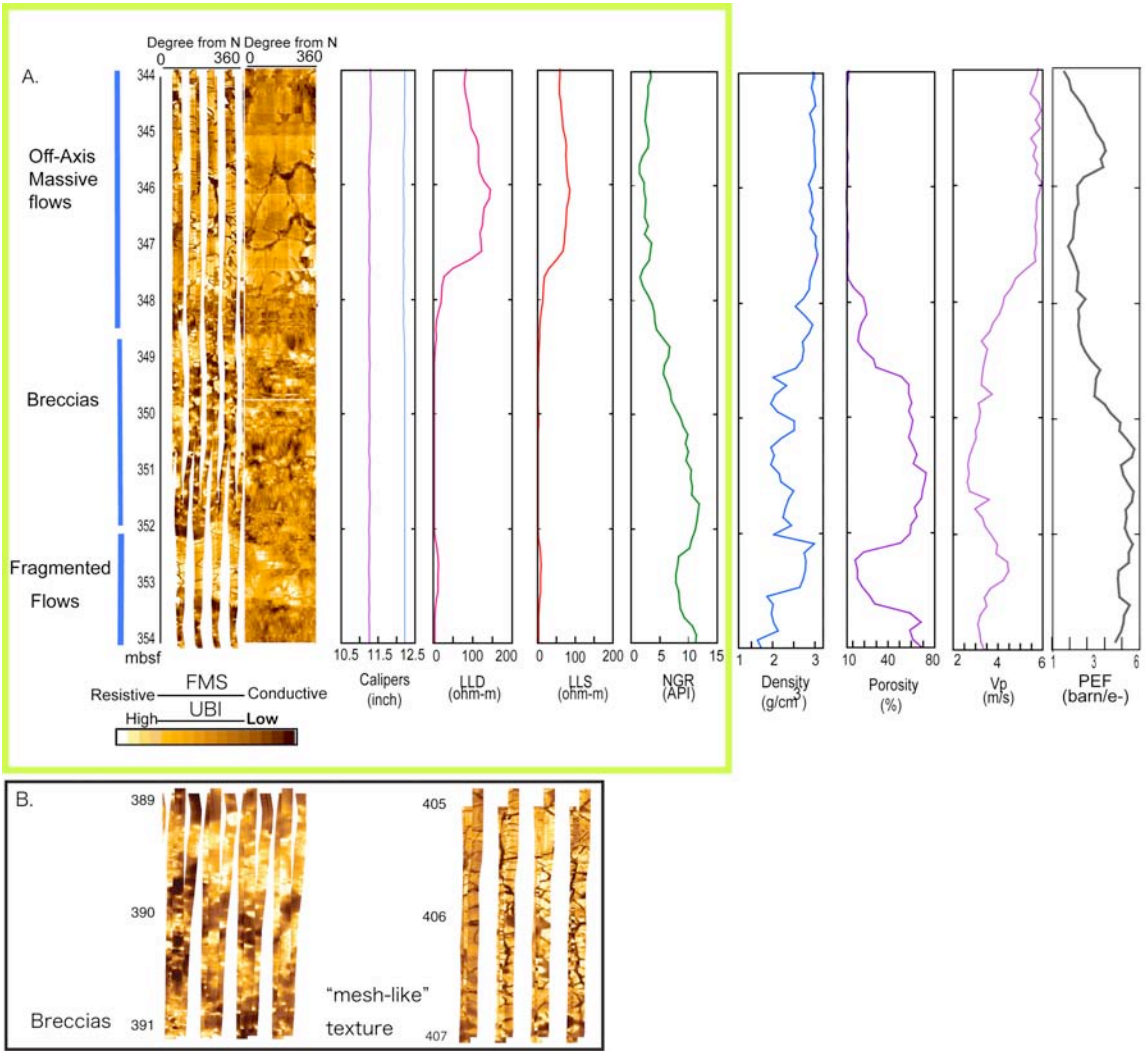

Figure 27. Example of electrofacies analyses over the interval 344 – 354 mbsf. (A) The base of the massive off-axis ponded lava flow underlain by breccias and fragmented flows. Yellow box indicates the main parameters used for the analysis of this section (see detail in text). (B) Magnified version of "mesh-like" texture (left) and brecciation (right).

Fractured Massive Flows

This electrofacies is assigned to flows more than 2 m in thickness with less homogeneous texture than massive flows and commonly rounded-fractures apparent on the FMS and UBI images. The thickest fractured massive flow is located from 650-675 mbsf. We assume that the Fractured Massive Flows are Massive Flows that have been physically altered by fracturing or jointing. Due to the common presence of fractures, LLD and LLS values are slightly lower (1.6±0.3 Log-ohm•m) and NGR counts (4.1±2.6 API) are slightly higher than Massive Flows (Figure 28, Table 5).

Pillow Lavas

We identified Pillow Lavas in the FMS and UBI images as rounded bodies with curved rims, radial fractures, downward drooping tear-drop shapes, relatively highly conductive interstitial material, and irregular patches within the more massive interiors. The Pillow Lavas are localized between 700 – 810 mbsf. Lava pillow sizes measured from the FMS images range from a few tens of centimeters to approximately 1 m in diameter. The estimation of lava pillow sizes is limited by the diameter of the borehole which might lead to an underestimation of the percentage of pillows and overestimation the variability in lava flow types. The relatively low LLD and LLS (1.5±0.3 Log-ohm•m) and high NGR (5.2±2.2 API) are attributed to the highly fractured, porous structure of the pillow sequence (Figure 29, Table 5).

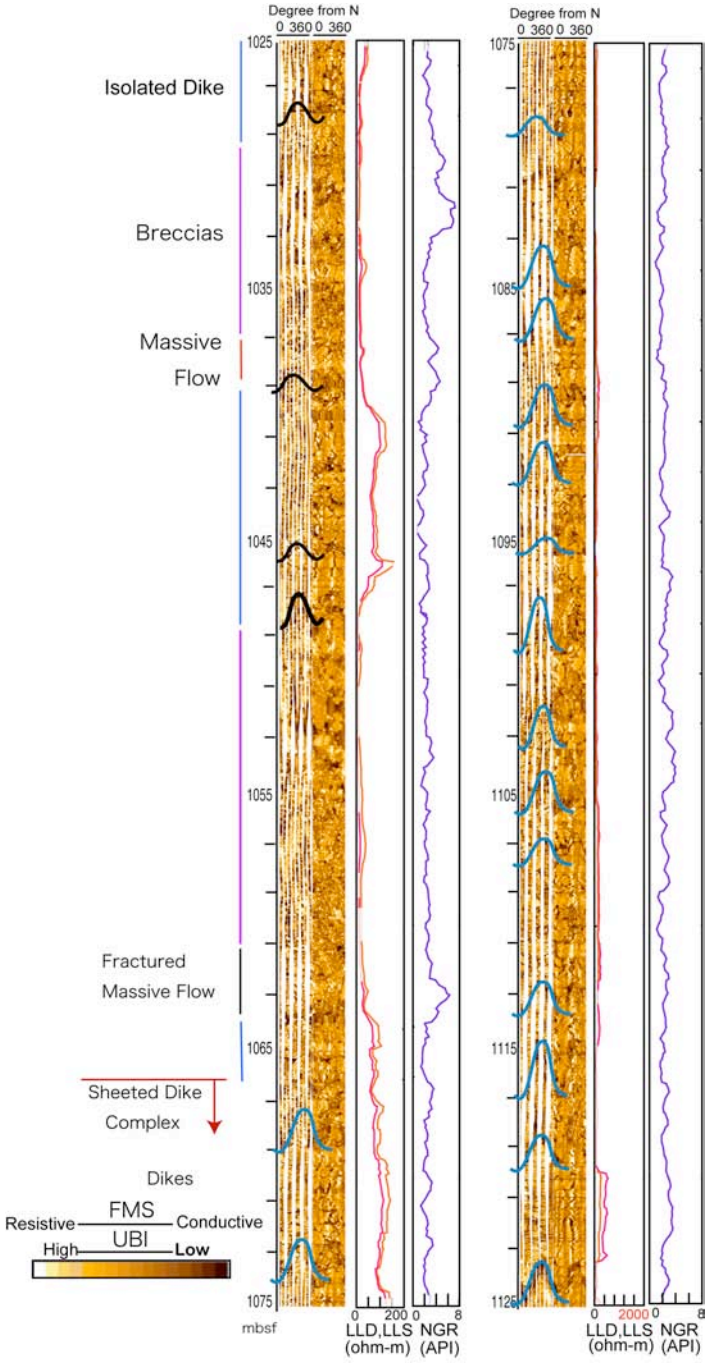

Figure 28. Electrofacies analyses over the interval 1025 - 1125 mbsf with FMS, UBI, LLD and LLS, and NGR wire-line logs. Black and blue sinusoid lines indicate subvertical contacts of Isolated Dikes and Dikes in dike complex, respectively. The red line and arrow indicate the boundary between lowermost fragmented flow and massive flow intervals indicating the bottom of the transition zone. The range of LLD and LLS increases drastically from the upper to lower part of the dike interval due to decreasing porosity in the formation.

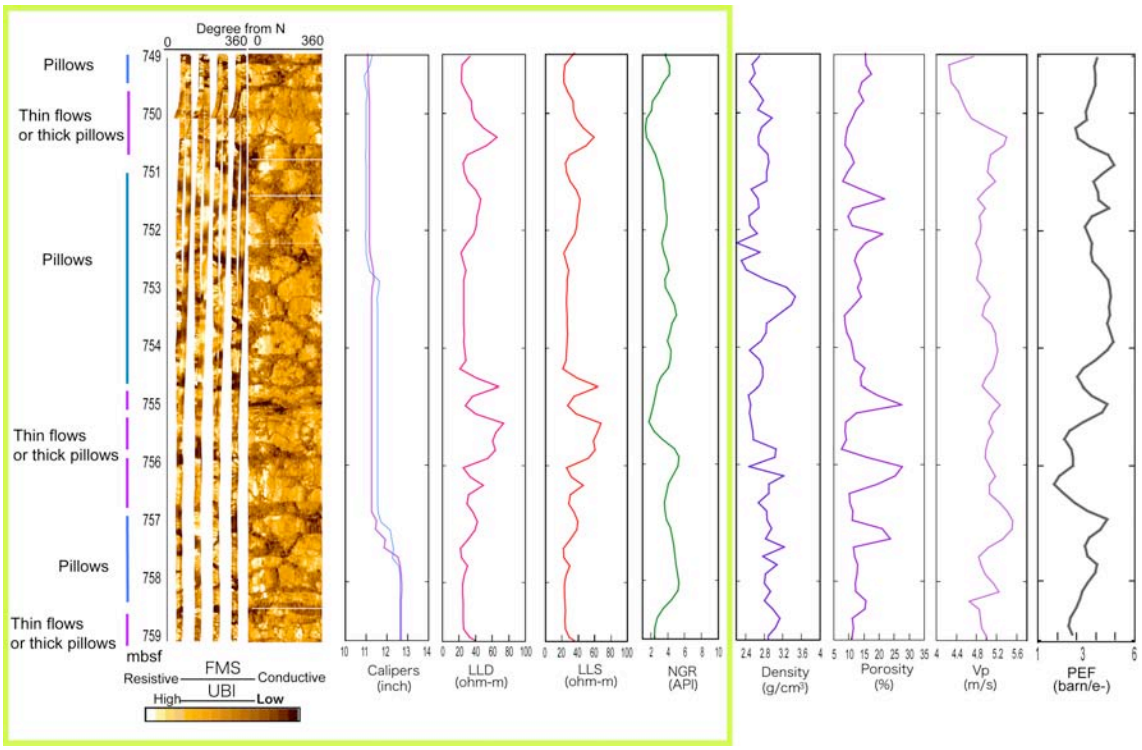

Figure 29. Example of Electrofacies Analyses over the Interval 749-759 mbsf. Possible pillow lavas were observed. Particularly in 751-755 mbsf, curved rims, radiation fractures, highly altered patches, and highly conductive (darker color in this image) interpillows are clearly observed. 755-757 mbsf, two 1 m flows with distinctive flow boundaries are observed, both of which we interpreted as thin flows or thick pillows.

Thin Flows/Thick Pillows

We identified Thin Flows/Thick Pillows as thin, ~1 m thick flows with relatively homogeneous textures in the FMS and UBI images but common rounded boundaries. The occurrence of this electrofacies is confined to between 410 and 910 mbsf and such rocks are most commonly observed between 575-600, 700-810, and 875-910 mbsf. In the interval of 700-801 msbf, these flows appear interbedded with Fragmented Flows and Pillow lavas.

The name of this electrofacies reflects the uncertainty of our determination of this rock type. When the drilling penetrates through the center of a ~1 m-thick lava pillow, the wire-line log responses will be similar to that of a ~ 1 m thick flow with distinctive flow boundaries on the top and bottom, because the curved rims of the pillow may not be intersected by the bore hole or apparent on the FMS images. Hence, it is difficult to unequivocally determine solely from wire-line logs whether this lithofacies type represents sheet flow or relatively thick pillow lava. LLD and LLS measurements are typically higher than the immediately overlying or underlying intervals (1.6±0.4 Log-ohm•m). NGR counts are on average moderate but display a wide range (4.6±2.4 API; Figure 29, Table 5).

Fragmented Flows

Fragmented Flows are intervals with common fractures that appear as diagonal mesh-like textures on the FMS and UBI images. Fragmented Flows are the most abundant electrofacies in the volcanic sequence of Hole 1256D. These flows are located throughout the volcanic section of the hole from 350 to 1064 mbsf and thickness of individual units varies from a few tens of centimeters to >20 meters (e.g., intervals 351-381 and 775-805 mbsf). On the FMS and UBI images, we observe thick intervals displaying the mesh fabric morphology, isolated by highly conductive, flow boundary zones or fractures. We suspect that the Fragmented Flows originate from Massive Flows although pervasive fracturing makes it difficult to discount other origins. A few intervals of Fragmented Flows correspond to recovered samples of breccias. Identifying

exact *in situ* locations of those breccia pieces is challenging because there are multiple high resistivity patches among fragmented, conductive formation on the FMS and UBI images, any of which could be the original sites. LLD and LLS measurements are moderate (1.5±0.4 Log-ohm・m) and NGR is relatively high (4.7±2.4 API; Figure 27, Table 5).

Breccias

We identified Breccias as intervals with completely fragmented textures on the FMS and UBI images, in which the fragments of the original formations appear to be chaotically arranged. The highly fragmented texture of these formations makes it difficult to distinguish lithologic boundaries and conductive fractures. This electrofacies is associated with low LLD and LLS (1.5±0.4 Log-ohm•m) and high NGR (4.4±2.4 API) compared to adjacent formations (Figure 27, Table 5). Breccias are most common in the upper (350 -700 mbsf) and lower (910 – 1060 mbsf) portions of the volcanic sequence.

Breccia intervals in this lower zone correspond to the common breccia samples recovered around the lithologic transition zone between 1000 – 1060 mbsf. We presume that these breccias were rubble formed by collapse of inflated lobate sheet flows or talus rubble in tension fissures and faults. Some breccia zones occur along sub-vertical contacts that may be dike margins (e.g., at 914 mbsf).

Dikes in Sheeted Dike Complex

We identified the Dikes in sheeted dike complex (7) that comprise the ~ 350 m of the Hole 1256D sheeted dike complex (1064 – 1412 mbsf). We identified fractures that are separated by sub-parallel, sub-vertical high conductivity contacts with consistent orientations as individual dike margins. These features indicate the presence of a sheeted dike complex (Figures 28 and 30). Eighty-six sub-vertical contacts were identified in the logs between 1064 - 1412 mbsf. Assuming individual dike thickness is measured between a pair of chilled contacts, the average thickness of dikes is 0.5 ± 0.8 m. The average dip and dip direction of the contacts are ~79° ± 8° and 053 ± 23, respectively, calculated by using statistics of spherical coordinate system [*Fisher et al.*, 1987] (Figures 31A and B). This is in good agreement with dike margin measurements made on the cores recovered from this interval (average dip 76°±16° (N=19), see structure_log and dike_log in *Teagle et al.*, 2006). The dike orientation suggests that the sheeted dike complex at Site 1256 crust is tilted slightly away from the paleo-spreading ridge. The FMS and UBI textures of the Dikes are similar to those of the Massive Flows although dikes are commonly brecciated along subvertical contacts. LLD and LLS values increase dramatically below 1064 mbsf to 2.6±0.6 (Log-ohm•m), which is ten times higher than that of upper volcanic flows, indicative of the paucity of fractures in this formation except the sub-vertical contact zones. NGR values are relatively high on average (4.3±1.3 API) probably due to strong alteration and mineralization along the sub-vertical contacts as evidenced in the recovered cores. The values of LLD and LLS are generally

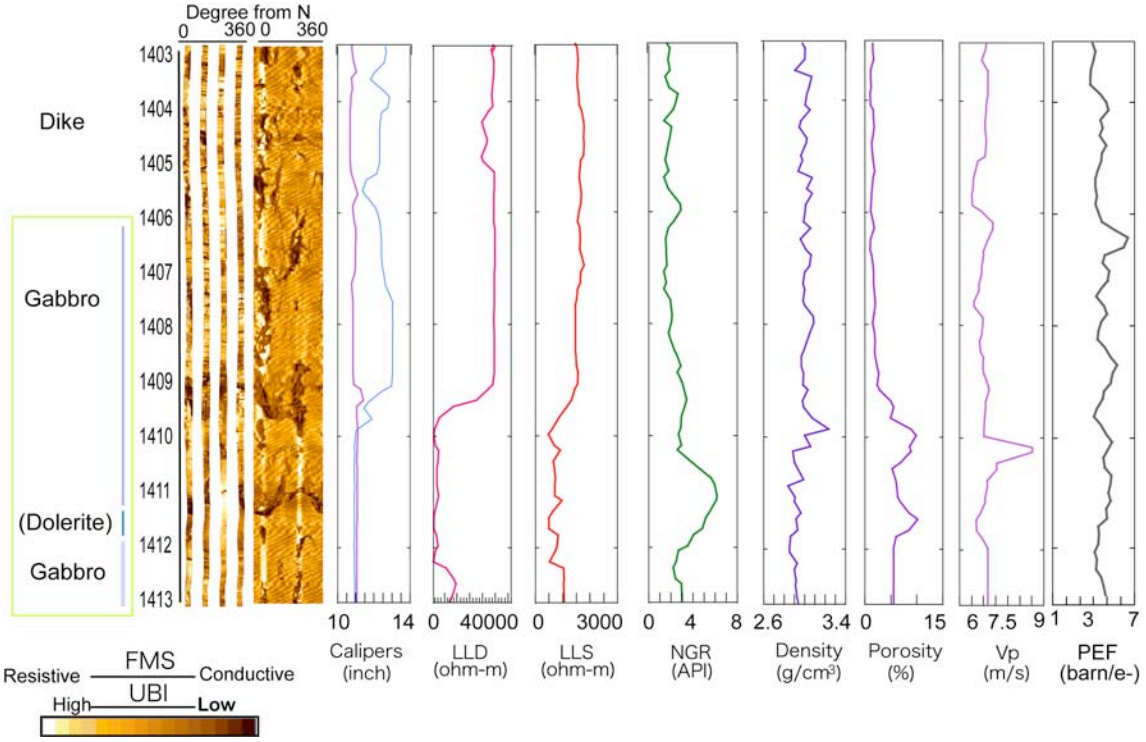

Figure 30. Electrofacies analyses over the interval 1403 - 1413 mbsf. We locate the depth of the gabbro based on the curatorial depths because DualLaterolog tool appears to have reached its detection limit (see LLD values). This may be due to the inappropriate preparation of the borehole prior to logging, resulted in a more than 5 times resistivity contrast between the borehole wall and water-filled borehole. Before future logging of gabbroic intervals the borehole should be flushed with fresh water to reduce the resistivity contrast (e.g., ODP Leg 176 Scientific Party, 1998).

high (> 3.0 Log-ohm•m) in the dike complex. Localized, anomalously high LLD readings (~ 4.0 Log-ohm•m) at 1345 mbsf coincide with the first downhole occurrence of granoblastic dikes (Figure 28, Table 5). Sub-horizontal to moderate dipping, evenly spaced (0.1~1 m) linear features are observed in the cores of dikes (localized around 1119-1124, 1137-1143, 1147-1155, 1226-1227, 1236-1240, 1244-1251, 1258-1261, 1263-1266, 1274-1277, 1279-1295, 1310-1329, 1333-1338, 1343-1345, 1350-1369,

1371-1376, 1383-1409 mbsf) but the origin of these features remains unknown. These features may be open fractures or cooling joints orthogonal to dike margins.

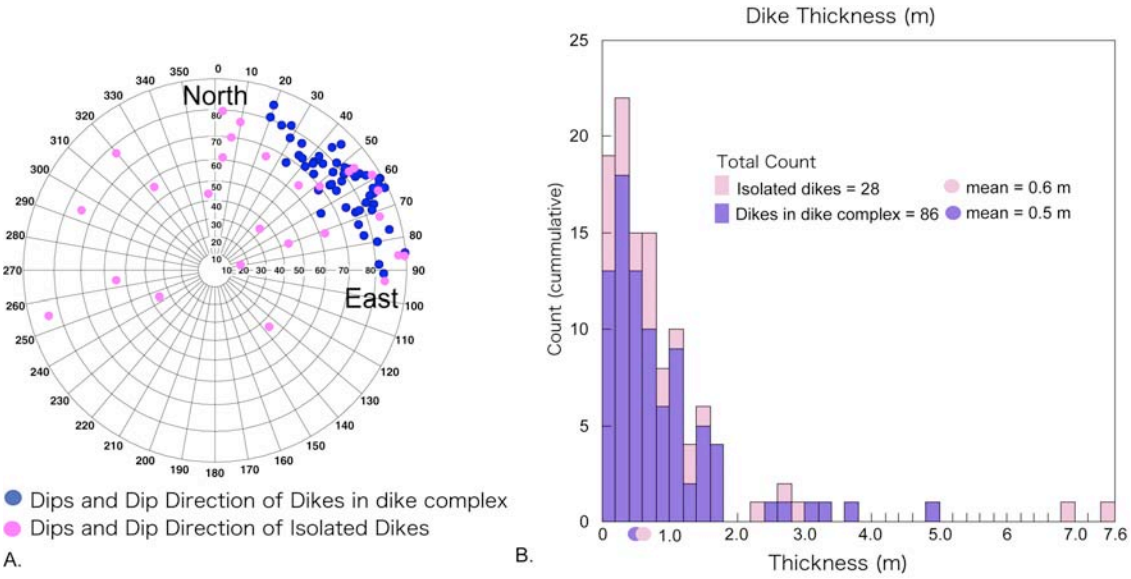

Figure 31. Stereonet (Equal Area, Lower Hemisphere) of Observed Dike Contacts. (A) Blue and pink dots indicate identified subvertical contacts of Dikes in dike complex and Isolated Dikes, respectively, from FMS images. (B) Frequency distribution of dike thicknesses from the Isolated Dikes (blue) and the Dikes in the Sheeted Dike Complex (pink).

Isolated Dikes

We identified Isolated Dikes within the volcanic section (< 1064 mbsf) which exhibit Massive Flow-like textures on the FMS and UBI images sandwiched between pairs of sub-vertical contacts with attitudes of dips similar to margins observed in the underlying sheeted dike complex. These Isolated Dikes observed from the FMS images are reminiscent of the narrow inter-fingered dikes rarely present in the recovered cores

although it is difficult to validate one-to-one correlations (e.g., interfingered dikes in Core 309-1256D-120R-1, 8-26 cm - and Isolated Dikes observed at 1018 mbsf on the FMS image). We found 28 Isolated Dikes between 810 – 1064 mbsf with average thickness of 0.5±1.8 m (Figures 31A and B). The average dip and dip directions of the contacts are ~79° ± 23° and 033 ± 67, respectively, calculated by using statistics of spherical coordinate system (Fisher et al., 1987). LLD and LLS values are slightly higher than that of Massive Flows (1.7±0.4 (Log-ohm•m)) and NGR is low to moderate (3.6±2.9 API)(Table 5). Below 910 mbsf in the lithologic transition zone, Isolated Dikes are commonly associated with brecciated margins.

Gabbros

As discussed previously, the malfunction of the resistivity sensors due to the extreme contrast between highly conductive seawater filling the borehole and highly resistive igneous formation precludes detailed analysis of this section. Gabbros are assigned to our new crustal stratigraphy using the curatorial depths from the recovered core (Figure 30).

DISCUSSION

Pillows or Not Pillows

In previous core-log integration studies, to obtain characteristic logging tool responses for a rock type, comparisons were made among the rock type from core observations, logging tool responses, and a partial cross-sectional view of the

accumulated lava flows as represented by resistivity contrasts on the FMS images. The obtained logging responses become criteria to determine rock types particularly in zones of low and no core recovery [e.g. *Bartetzko et al.*, 2002; *Révillon et al.*, 2002; *Barr et al.*, 2002]. Following this approach, however, we found that the identification of Pillow Lavas is particularly challenging for two reasons. First, pillows can be misidentified in core observations. The traditional pillow determination criteria in recovered core pieces are based on pillows seen in ophiolites [e.g., *Gillis and Sapp*, 1997], such as (a) curved or rounded chilled margins with radial fracturing, (b) changes in grain size from the rim to the center of pillows and the presence of glass and varioles. Although helpful, these criteria are not definitive for identifying pillow lavas in drilled cores. Second, the challenge in core-log integration is to interpret and sub-divide the overlapping ranges of tool responses to establish a representative set of responses for pillows. It is obvious from our FMS images that curved margins of pillows and fractured pillow intgeriors resemble characteristics of fragmented flow formations, making it difficult to use logging tool responses to isolate a rock type (e.g., Fragmented Flow) from others (e.g., pillows). For our analysis, developing methods to confidently identify lava morphologies from wire-line logs, specifically from the FMS images, was necessary.

To explore if a correlation between recovered core pieces and pillow-like FMS images is available, we re-visited the distribution of the cores recovered and FMS images from two other ODP/IODP holes. We first visited IODP Hole U1301B that drilled into intermediate spreading rate crust on the eastern flank of the Juan de Fuca Ridge, from which many apparent pillow lavas were recovered [*Fisher et al.*, 2005].

However, a paucity of good FMS logs precludes similar analysis. Future drilling and logging at this site may provide sufficient FMS borehole coverage to test pillow lava identification and occurrences.

We next examined ODP Hole 801C, whichpenetrated into ocean crust formed at a fast spreading rate [*Plank et al.*, 2000]. At this site, the previous most comprehensive core-log integration study was carried out [*Barr et al.*, 2002]. Their pillows were "characterized by more variable log responses…the average log values are intermediate between those for massive basalts and breccia…FMS images of pillow lavas are characterized by bright, rounded regions of relatively uniform resistivity (pillows) separated by darker, more conductive intervals that represent altered interpillow zones". However, our examination of the Visual Core Descriptions from Hole 801C [*Plank et al.*, 2000] and comparison with the shipboard lithostratigraphy and FMS images as reported by *Barr et al.* (2002) suggest that their core-log integration overestimated pillows and the aforementioned set of log responses for pillows may be erroneous. *Barr et al.* (2002) cite the presence of curved chilled margins as a distinguishing characteristic of pillows in the shipboard core lithostratigraphy, but cooling unit thickness was the only criteria used on shipboard to distinguish pillows from massive flows [*Plank et al.*, 2000]. *Barr et al.* (2002) lumped the shipboard "pillows" and "pillows or flows" units together as pillow. Some pillow units in the shipboard lithostratigraphy of Hole 801C (e.g., those associated with the two hydrothermal deposits) have clear characteristics of pillows in the recovered drill cores, core photographs, and the Visual Core Descriptions, including subvertical and irregular curved glassy margins in addition to subhorizontal curved

chilled margins [*Plank et al.*, 2000] (J. Alt, personal observation). In contrast, Cores 34-36 and 38-39, which in the shipboard lithostratigraphy figures [*Plank et al.*, 2000] and Figure 12 in *Barr et al.* (2002) are plotted as exclusively pillows, contain only horizontal to subhorizontal chilled margins, consistent with thin flows or possibly with pillows. These units lack any hyaloclastite or clear tiny pillow fragments, or subvertical curved chilled glassy margins that would favor their interpetation as pillow basalts. Moreover, in the shipboard Visual Core Descriptions, most of the cooling units in Cores 34-36 and 38-39 are classified as "Flows" and "Pillows or Flows", with only a few cooling units described as "Pillows" on the basis of their thickness less than 0.5m [*Plank et al.*, 2000]. Thus the available evidence suggests that Cores 801C 34-36 and 38-39 are better classified as thin flows than as exclusively pillows. Based on our criteria for FMS image/electrofacies analysis developed for Hole 1256D, many of the purported “pillows” in the Hole 801C volcanostratigraphy would be instead classified as Thin Flows/Thick Pillows or Fragmented Flows.

To explore other indications for the occurrence of pillow lavas, we examined whether the distribution of basaltic glass recovered downhole correlates with our identification of pillow lavas in Hole 1256D. Glass was most commonly recovered from the upper and middle parts of Hole 1256D (350- 1050 and 1150-1250 mbsf) and corresponds to several rock types, such as Fragmented Flows, Breccias, and Pillow Lavas (Figure 24). However, all such flow styles will develop a few centimeters of surficial glass when they interact with cold seawater and hence, glass recovery is not a unique parameter for identifying Pillow Lavas. We also examined the radius of

curvature of curvy textures identified in the FMS images to investigate whether this can be utilized to identify pillows; however, this is also not a definitive parameter as the size of pillows in submarine environments can vary from 0.1 (knobby pillows) to a few meters (elongate/bulbous pillows) [e.g., *Lonsdale and Spiess*, 1980].

We conclude that classifying flow types for a volcanostratigraphy model based on electrofacies analyses better relies on criteria that are principally based on the morphology of FMS images with good lateral coverage of the borehole wall. For pillows these features include closely packed, downward drooping tear-drop shapes, radial fractures, highly conductive inter-pillow materials, and high conductivity irregular alteration patches (Figure 29). Some Fragmented Flows resemble these morphologies, but generally also display smaller scale, mesh-like fracturing systems (scale of fracturing a few ~10 cm) (Figure 27B).

Implementation of the above criteria has led to a thorough revision of the occurrence of Pillow Lavas from that proposed in the Hole 1256D shipboard stratigraphy (364 and 788.8 mbsf) with new intervals of Pillow Lavas being identified and previously recognized intervals being re-classified as other rock types. A number of 1 to 10 m-thick intervals that satisfy our Pillow Lava criteria in the FMS and UBI images occur between 700 – 810 mbsf. These rocks were classified as sheet flows in the onboard observations [*Teagle et al.*, 2006].

Fragmented Flows and Breccias

The porosity and permeability structure of the upper oceanic crust is critically

important to understanding hydrothermal alteration processes [e.g., *Alt et al.*, 1986; *Alt et al.*, 1996; *Alt*, 2004; *Fisher*, 2004; *Fisher et al.*, 2005]. Fluid flow and chemical exchange are tightly linked to the bulk porosity of the crust and the distribution of highly fractured and brecciated rock types. However, such intervals are commonly absent or very poorly represented in cores recovered by ocean drilling and hence their distribution must be determined from wire-line criteria. This is a major hindrance to investigations of seawater-basalt chemical exchange because these intervals endure the most intensive hydrothermal alteration in the oceanic crust. We propose three different physically-altered, fragmented lithofacies in our volcanostratigraphy: Fractured Massive Flows, Fragmented Flows, and Breccias. Overall, these three flow types make up more than 40% of Hole 1256D and more than 50% of the volcanic sequences (Figures 24 and 25, Table 6). We used the term "fragmented" to indicate fractures that may have been physically developed through construction of the upper oceanic crust. From electrofacies analysis, we suggest that the range of fragmented flows observed downhole is best separated, rather than grouped together as "breccias", as in previous studies [e.g., *Barr et al.*, 2002]. This is because the degrees of fragmentation and the volcanic origins of flows can be different, and these are clearly discernible from the wire line images.

Each lithofacies shows a different distribution downhole. The majority of Fractured Massive Flows occurs between 625- 675 mbsf. Fragmented Flows are regularly distributed between 350-950 mbsf and Breccias are concentrated in the upper (350-700 mbsf) and lower (925-1065 mbsf) parts of the extrusive section (Figure 24). Fractured Massive Flows and Fragmented Flows show areas of relatively homogeneous

texture similar to that displayed in intervals of Massive Flows or Thin Flow/Thick Pillows. These flows, hence, may have originally comprised a variety of relatively high effusion-rate flows such as lobate, wrinkled, jumbled, lineated sheet flows as are commonly observed at the EPR ridge crest [*Fornari et al.*, 1998, 2004]. The fragmentation (faulting) could be induced during cooling/quenching, due to lava loading, or local and/or regional tectonics before chemical alteration [e.g., *Escartin et al.*, 2007].

The origin of Breccias appears to be different from other fragmented rock types because brecciated intervals are completely fragmented and any primary volcanic textures, if ever present, are destroyed. We attribute these highly fragmented intervals to such features as shattered pillows caused by landsliding on slopes [*Moore*, 2001], collapsed pits amongst lobe/inflated flows [*Umino et al.*, 2000], collapsed lava pillars [*Perfit et al.*, 2003], and sagged lava channels [*Soule et al.*, 2005].

Lava-Dike Transition Zone

The boundary between lava sequences and the sheeted dike complex in both ophiolites and intact ocean crust is laterally and stratigraphically transitional with a change from <10% to >90% dikes commonly occurring over a vertical distance of ~100 m [e.g., *Gass,* 1960; *Wilson*, 1959, *Hooft et al.*, 1996]. In Hole 504B this transition, as determined by core descriptions, occurs between 572 and 781 msb [*Alt et al.*, 1996] and marks a zone over which there are major changes in crustal physical properties (e.g., permeability) [*Becker*, 1989] and hydrothermal alteration.

In Hole 1256D the upper boundary of the Transition Zone was placed at 1004.2 mbsf (Core 1256D-117R-1, 85 cm) because of the first presence in the cores of isolated dikes and the occurrence of sub-greenschist facies secondary alteration minerals [*Teagle et al.*, 2006]. However, the low recovery rates in Hole 1256D, especially from brecciated intervals and fracture fillings, means that the exact shallowest *in situ* depth of the sub-greenschist facies minerals remains uncertain. Unfortunately, there are not significant changes in the wire-line logs at this level and the precise position of the upper boundary of the Transition Zone in Hole 1256D remains equivocal.

The lower boundary of the Transition Zone at 1061 mbsf was assigned based on shipboard petrological observations of recovered core pieces [*Teagle et al.*, 2006]. Electrofacies analysis suggests that the lowermost Fractured Massive Flow and Massive Flow ccurs at 1064 mbsf. The corresponding recovered core comprises only short core pieces (Core 1256D-128R1 Piece 16-21) consistent with being from the lowermost Fractured Massive Flow (1061-1064 mbsf) (Appendix D, Figure 28). Dikes are observed as the dominant rock type below this depth in both the drill core and the wire-line logs, with gradational changes in wire-line physical properties, particularly increases in LLD and LLS values. Therefore we propose 1064 mbsf as the lower boundary of the Transition Zone in our new crustal stratigraphy.

TOWARDS AN OBJECTIVE, QUANTITATIVE VOLCANOSTRATIGRAPHY

In addition to the qualitative electrofacies analysis above, we carried out an alternate approach to construct a completely objective, quantitative volcanostratigraphy

by using an unsupervised ANN method. An ANN is a computer algorithm designed following the information transportation and interpretation systems of the human brain. The principal abilities of ANN are the adaptive classification, prediction, and correlation of input information. ANN approach has advantages superior to other classification techniques (e.g., K-means clustering, discriminant analysis) as there is no need for pre-screening of outliers or scaling input data sets following theoretical mechanisms. Without prerequisite knowledge of the logic behind a problem or behavior, ANN can act as a nonparametric, nonlinear regression technique so that we do not have to know how the data will be fitted by the modeling before the calculation [*Dowla and Rogers*, 1995]. This nature of ANN makes it possible to sort data into an almost unlimited desired number of classes. In any classification technique, one may wish to determine the number of significant discriminant groups, and in the case of ANN, we determine the number of classes (neurons). ANN technique is potentially of great value for the analysis of multiple parameter observations such as downhole wire-line logs. If successful, a quantitative crustal stratigraphy could be constructed by classifying rock types or eruptive styles based solely on distinctive ranges of numerical logging parameters.

ANN algorithms are broadly classified into two groups: supervised and unsupervised. Supervised ANN requires three steps in the task of classification. The first stage is "training" where a network is trained using input and desired output data sets. Next, the trained network is tested on examples it has not seen. Lastly, the successfully trained network is applied to new data sets and classifies the data into

designated groups [e.g., *Dowla and Rogers*, 1995]. In contrast, unsupervised ANN analyzes input data without predetermined output targets. The unsupervised network classifies input data into designated numbers of classes by finding clusters or similarities within the data based on topological mapping [*Dowla and Rogers*, 1995].

ANN approaches have been used in the petroleum industry to map hydrological properties within reservoirs (e.g., porosity, permeability) or environmental test sites [e.g., *Link and Blundell*, 2003]. ANN have been only rarely applied in scientific ocean drilling [e.g., *Benaouda et al.*, 1999; *Moritz et al.*, 2000; *Goutorbe et al.*, 2006] and only once to examine downhole lithostratigraphy. Hole 792E located in the Izu-Bonin forearc comprises a sequence of volcanoclastic sandstones, conglomerates and claystones [*Taylor and Shipboard Scientific Party*, 1990] drilled on Leg 126 with relatively high rates of recovery (> 50 %). Wire-line data from this site were analyzed using supervised ANN routines where pre-determined combinations of ANN classes had been calibrated against the rock types known from the recovered cores. ANN analysis performed better than other automated classification and feature detection techniques (e.g., discriminant analysis) in constructing a downhole lithostratigraphy [*Benaouda et al.*, 1999].

Previous to our study, there has been no attempt to deploy ANN to analyze wire-line logs of a highly fractured and variable substrate such as oceanic volcanic basement. Here we attempt to establish a quantitative volcanostratigraphy directly from wire-line logs using an unsupervised ANN to test whether such an approach could be applied to rapidly construct a preliminary continuous downhole stratigraphy analysis, as would be useful aboard ship directly following wire-line logging operations.

Application of Artificial Neural Network

The self-organizing feature map (SOFM) [*Kohonen*, 1987] is an unsupervised ANN method and an example of a competitive network in which the number of classes or groups are user-defined input to the ANN system. The ANN classifies data by receiving input data and establishing stable boundaries (the number of boundaries = user-defined number of classes) amongst the input data. Weight vectors that correspond to the number of classes are initially set to random values. Once the boundaries become stable, these can delineate unknown input as the training stage is done [*Hagan et al.*, 1996]. This style of unsupervised network may be useful for constructing a quantitative volcanostratigraphy because it requires little input or bias from the interpreter and should achieve a completely objective output.

Methodology for Building Quantitative Lithostratigraphy

We have employed an unsupervised SOFM to classify logging parameters from Hole 1256D to construct a quantitative volcanostratigraphy model. The calculation subroutines were programmed with the MATLAB® neural network toolbox. An unsupervised approach was used to avoid biasing the lithological classification, as would result if we employed a supervised approach with pre-determined lithologic classifications based on the incomplete information yielded by the recovered cores.

We first re-examined the volcanic section of our qualitative electrofacies analysis of Hole 1256D to build a simplified template lithostratigraphy of the hole for later comparison with our ANN output. We propose two different grouping of the rock types

from our volcanostratigraphy model. In the first grouping the eight electrofacies in the volcanic section are clustered based on Rock types observed from the fast-spreading EPR crust: massive sheet flows, fragmented flows, pillow lavas, and breccias [e.g., *Fornari et al.*, 1998, 2004; *Bartetzko et al.*, 2002] into four major groups (R1) massive flows, massive off-axis ponded lava, and fractured massive flows; (R2) pillow lavas and thin flows; (R3) fragmented flows and breccias; and (R4) isolated dikes (Figure 32-A1). In the second grouping elctrofacies are clustered based on similar textures on the FMS images into four major groups: (T1) massive flows, massive off-axis ponded lava, fractured massive flows, and isolate dikes; (T2) pillow lavas and thick pillow/thin flows; (T3) fragmented flows; and (T4) breccias (Figure 32-A2). The major difference between these two templates is the treatment of isolated dikes (Figure 32-A1) and breccias (Figure 32-A2) as independent subdivisions.

For the input data set to the ANN calculations, we used all the available one-dimensional wire-line logs including LLD, LLS, NGR, density, porosity, Vp, and photoelectric effect factor measurements. We found that the combination of all wire-line logging responses provided the most complete description of the *in situ* physical properties of the crust penetrated by Hole 1256D, following numerous trial-and-error examinations of different combinations of the numbers and types of wire-line logs.

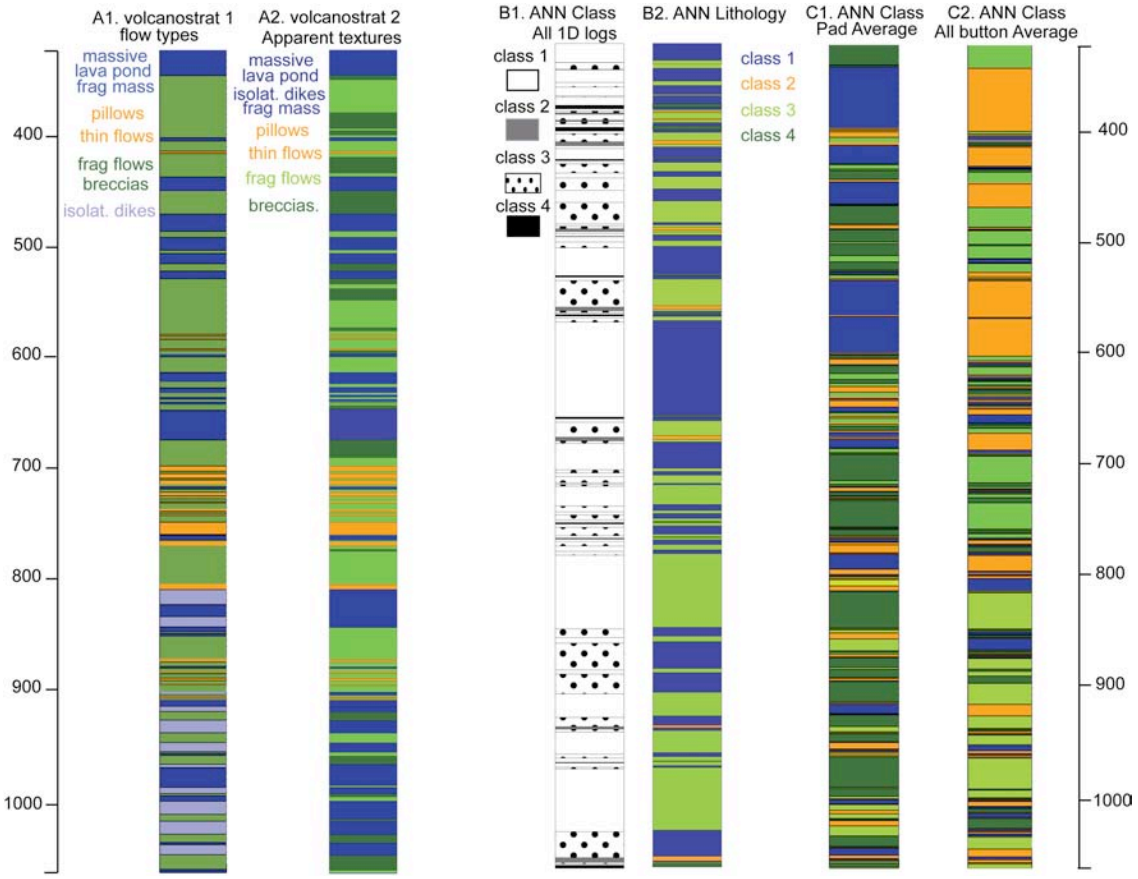

Figure 32. Simplified volcanostratigraphy models from electrofacies analysis and selected plots from ANN analyses. (A1) simplified volcanostratigraphy model following flow types. Colored letters correspond to stratigraphic layers with same color. (A2) simplified volcanostratigraphy model following apparent texture types. Colored letters correspond to stratigraphic layers with same color. (B1) ANN classification results with our choice of parameters (see section 6.2 for details). Class 1 ~ 4 are displayed with different patterns. (B2) ANN lithology based on the comparison between A2 and B1. Color coding follows lithologies in A1 model (see section 6.3 for details about the correlations). (C1) Example of ANN results with FMS pad averages. 16 buttons on one pad were averaged into a pad average value at a sampling depth. (C2) Example of ANN results with FMS button averages. 64 buttons on all (four) pads were averaged in a button average value at a sampling depth. Color coding of C1 and C2 models follows B2.

To use the Hole 1256D wire-line logs, we first interpolated all logs from 312 to 1064 mbsf, to a 0.15 m sampling interval to create common sampling depth profiles. This is necessary because different wire-line tools analyze the borehole walls over

different depth ranges. Since we proposed two different groupings of four rock types or FMS morphologies, the number of classes in the ANN calculation was set for four.

We used a boxcar filter for smoothing and finalizing the ANN classification. Smoothing of the results is an important process in the application of SOFM to problems where fine scale variation is the norm. If a smoothing filter is not applied the SOFM results are dominated by high frequency variations in the input logs that emphasize the gradations from one class to the other, and inhibit interpretation. It should be noted that when larger numbers of output classes are used, the resulting classifications often show smooth gradations from one class to the other [*Link and Blundell*, 2003]. To find the best smoothing filter size, we carried out numerous trial calculations in SOFM in pursuit of the best match between the output classes and our qualitative electrofacies volcanostratigraphy. After trials, we concluded that a sliding window of 33 points (~ 5 m) is most appropriate to evaluate the wire-line logs in the ANN training routine. Use of a sliding window allows the network to look at data before and after each analysis point. A ~5 m window is close to the length of an IODP half-core which was the typical advance during drilling Hole 1256D. This approach is then similar to the observation and comparison techniques used by human interpreters of both cores and wire line logs.

Table 7. Mean values and standard deviations for ANN classes (325-1064 mbsf).

Class	LagLLD (ohm/m)	LogLLS(hm/m)	API(count)	Porosity (%)	Density (g/m^3)	Vp (m/s)	PEF ($barns/e^-$)
1	1.2±0.4	1.1±0.4	4.7±1.8	30.8±19.1	2.5±0.4	4.6±0.8	3.1±0.8
2	1.6±0.4	1.5±0.4	4.0±2.1	20.4±16.0	2.7±0.3	5.3±0.6	3.2±1.0
3	1.5±0.4	1.4±0.5	4.9±2.9	23.4±19.8	2.6±0.4	5.1± 0.6	3.2±1.0
4	1.5±0.5	1.4±0.5	4.0±2.2	30.1±25.4	2.6±0.4	5.2± 0.8	3.1±1.1

Note that these values are calculated from wire-line log from Expedition 312.

Results: Quantitative ANN-based Volcanostratigraphy

The resulting four ANN classes (hereafter Class A1 ~ 4) represent different characteristics of *in situ* rock formation in Hole 1256D. The classification was calculated based on the combinations of all the wire-line logs responses at a given depth by the SOFM program with aforementioned parameters.

The ANN classification that resulted from using our selection of the parameters indicates that the order of the abundance (total thickness) of classes is Class A1 > Class A3 > Class A2 ≈ Class A4 (Figure 32-B1, Table 7). Overall, the distribution of these classes down hole comprises relatively thick intervals of Classes A1 and A3 with thinner layers of Classes A2 and A4. Very thick intervals of Class A1 from 550 to 650, from 750 to 850, and from 950 to 1030 mbsf are distinctive. The thin layers of Class A2 and A4 show two different styles of distribution. Class A4 layers are commonly associated with Classes A3, and Class A2 layers are found in thick Class A1 and A3 layers. A set of logging tool responses of a Class suggests characteristics of the *in situ* formation (Table 7). Class 1 is the formation characterized by low porosity, low NGR, and high Vp, indicating little fractured, less altered formation. In contrast, Class 4 is the formation characterized by high porosity, high NGR, and low Vp, indicating very fractured, highly altered formation. Class A2 and A3 are the formations characterized in between Class 1 and 4 formation types, indicating transitional layers between Classes A1 and A4. Provided the most distinctive difference between Class A2 and A3 are the NGR values, we suggest that Class A2 formation is less altered than Class A3 formation.

Comparing the abundance, distribution, and set of logging responses of the ANN Classes helps determine the representation of each Class in terms of lithology. We tried matching ANN classes with lithologies using the FMS textural (Figure 32-A2) volcanostratigraphy because the distribution of the ANN classes is most similar to the volcanostratigraphy model resulting from the FMS textural style types (T1-T4) as opposed to the flow types (R1-R4). The distribution of thick layering of massive flows (T1) from middle to lower part of the hole is almost identical to the distribution of ANN Class A1. Together with the end-member physical property characteristics of of Class A1 formations, we suggest that Class A1 represents massive flows and less fractured portions of other flows, such as thin flows and fragmented flows. Correlating the ANN classes to lithologies is more challenging for Class A2 that occur as thin layers between the massive flows and breccias or as localized thin layers. We suggest that Class A2 is not a specific lithology but represent zones of anomalous porosity within Class A1 formation. The distribution of Class A3 is roughly the same as that of fragmented flows (T3) and breccias (T4). Together with other characteristics of Class A3 formations, we suggest that Class A3 represents both fragmented flows and breccias. The abundance of Class A4 is very low and the distribution of this class is rare and seen as thin layers within Class A3. Because the other characteristics of Class A3 formations are in opposite sense from that of Class A1, we suggest Class A4 represents no lithology but zones of great degree of fragmentation and alteration within both fragmented flows and breccias.

Some limitations of this approach are illustrated by the assignment of thick intervals of Class 1 (massive flows) around 550-650 and 750-850 mbsf that correspond to significant intervals of fragmented flows as identified by our qualitative electrofacies-derived volcanostratigraphy. The wire-line responses of fragmented flows in this interval do not contrast strongly with those of massive flows and the ANN could not detect Class A3 around these depths. The ANN hence classified these rocks as Class A1 instead, highlighting the difficulties of decision making when the ANN encounters intermediate properties.

Discussion: The Applicability of ANN Modeling

The ANN-based stratigraphy (Figure 32-B2) more closely resembles our simplified electrofacies-derived volcanostratigraphy where rock types were clustered by textural style (Figure 32-A2) as opposed to lava flow type (Figure 32-A1). This points us towards the key properties that our ANN actually classifies. Local fracture systems and other controls on the bulk porosity (e.g., flow boundaries, breccias) have greatest influence on the resistivity distributions that lead to our interpretations of the FMS images. Bulk porosity is the primary parameter for many other crustal physical properties and imparts a major influence on the physical and chemical processes in the basement [*Alt*, 2004], and should have ranges that are distinctive from one rock type to another. There is a progressive increase in porosity from ANN Class A1 to Class A4, indicating that the local wall rock porosity has the strongest influence on our ANN classification.

The distribution of porosity structures, particularly Class A2 with intermediate porosities, may help us decipher lava depositional environments. Thin inter-layers of Class A2 associated with relatively thick intervals Class A1, appear to be porosity transitions from one end member to another. Such porosity transitions are commonly observed at ocean ridges at the top and base of massive flows (Class A1) with associating volcanic breccias (autobrecciation) (Class A2). For example, such structures would be observed at the base of a massive flow that had filled a pre-existing collapse pit or where the termination of lava supply results in the sagging and development of unsupported carapaces likely to collapse at the top of a massive flow.

Deeper in the hole, below 900 mbsf, Classes A2 and A3 occur independently of Classes A1 and A4, the sharp gradients in bulk porosity may be attributed to high effusion eruptions close to the ridge axis, where massive flows are deposited in thick layers but drain-back of lava creates thin lava crusts that can degrade to breccias. Our ANN method is most reliable for classifying rock types when there are sharp contrasts in porosity structures.

Caution is warranted utilizing ANN where there are major irregularities in the borehole walls as is common in ocean basement drilling. Wire-line tools commonly return incorrect readings from zones of extended borehole diameter because sensors are strongly influenced by seawater between the wire-line tools and the borehole wall. Our ANN would interpret such a zone as a highly porous formation, resulting in a mismatch between the ANN results and our electrofacies analysis. During the manual electrofacies analysis cross-sectional irregularities in Hole 1256D can be carefully monitored by

eyeball comparison of several wire-line logs and affected data disregarded. Prerequisite quality control thresholds on the caliper log could be set in the ANN to exclude certain data in the wire-line logs in zones of large borehole diameter. However, if we use the caliper logs to exclude too many of the irregularities in the borehole wall prior to ANN analysis, our classification outcomes become biased towards flow or porosity structures that correspond to the undisturbed borehole wall and more robust rock types. Nevertheless, we propose that ANN modeling improves our overview of porosity structure of the basement section, which can not be reconstructed from piecemeal core data, particularly in highly altered or fragmented formations that typically have very low recovery rates.

To explore other possible quantitative ANN models, we experimented with the quantitative use of FMS data. The FMS tool has four pads each with 16 resistivity sensor buttons. We have calculated continuous down hole average values for each pad and a button average value where the readings of all 64 buttons are averaged. The former represents the four different resistivity paths and the latter represents the cross sectional average of resistivity in Hole 1256D at a given depth. ANN stratigraphies calculated using only these averages are shown in Figures 32-C1 and C2 respectively. These models are very different from our qualitative electrofacies stratigraphy. FMS data are most useful when they are processed for the visualization purposes; otherwise, they just provide multiple pass measurements of resistivity along various paths similar to that returned by the 1 dimensional resistivity tools. Using only one input parameter or multiple measures of the basically same parameters (FMS-pads average) did not improve

the ANN adaptability because the resulting classes are only dependent on changes in that parameter so the weight functions that require multiple parameters can not be appropriately tuned.

CONCLUSIONS

Conclusions we draw from this study are:

(1) The electrofacies analysis in this study indicated that continuous wire-line log data linked with multiple FMS passes is imperative to compensate the low recovery in basement drilling. Multiple types of wire-line logs can be combined to discern different flow types, rock formations, flow boundaries and fracture geometries. Good borehole coverage with FMS images is particularly helpful for identifying the distribution of basement lithologies and structures. Assuming that bore holes are relatively circular and that tool passes follow different paths, whenever possible multiple runs of the FMS tool string should be attempted during ocean drilling expeditions, as increased borehole wall coverage provides major gains for the integration of recovered drill core and the wire line logs, and the development of representative basement volcanostratigraphies.

(2) Our electrofacies analysis suggests the upper oceanic crust in Hole 1256D (325-1425 mbsf) can be classified into zones of massive flows, massive off-axis ponded lava, fractured massive flows, fragmented flows, sheet flows or thick pillows, pillows, breccias, isolated dikes, dikes in sheeted dike complex, and gabbros. Each rock type can be attributed to an original flow or unit morphology but commonly these have been physically altered by fracturing and/or chemically altered by hydrothermal circulation.

(3) Evenly spaced sub-vertical contacts in dike section are observed in FMS images between 1100 and 1410 mbsf. This indicates that the dikes are "dikes in sheeted dike complex" as observed in ophiolites.

(4) From our volcanostratigraphy, the lower boundary of the transition zone was determined at 1064 mbsf.

(5) ANN methods primarily classify the basement with respect to its bulk porosity structures downhole. ANN modeling can improve our overview of the basement porosity structure which is not possible to reconstruct from the piecemeal information provided by the recovered cores, particularly in intervals of high fracturing and hydrothermal alteration that are typically poorly recovered.

CHAPTER V

EAST PACIFIC RISE LAVA DEPOSITION HISTORY: THE HIGH RESOLUTION CROSS SECTION VIEW OF THE SUPERFAST SPREADING UPPER OCEANIC CRUST

OVERVIEW

Detailed, high-resolution volcanic stratigraphy of Ocean Drilling Program (ODP) Hole 1256D, built on the integration of downhole wire-line logs and core data, makes it possible to provide the first vertical cross-sectional view of the *in situ* East Pacific Rise (EPR) upper crust. The model is mainly based on ten electrofacies identified from high-resolution Formation MicroScanner (FMS) images. The electrofacies within extrusive rocks are correlated with commonly observed EPR lava flow types, such as sheet flows and breccias, and subordinate pillows. Combined with well-studied EPR surface geology, this volcanostratigraphic model sheds new light on *in situ* EPR upper oceanic crust construction processes that have been detected only indirectly from subsurface geophysical data. The formation of a ~100 m of pillow section observed in Hole 1256D can be deposited on the slopes of the ridge based on the observation on the EPR lava flow types. Assuming paleo spreading rate was constant, 50 % of the extrusive rocks in Hole 1256D crust was formed within ~2 km of the ridge axis whereas nearly all of the rest of the extrusives was formed within ~3 km of the ridge axis.

INTRODUCTION

The architecture of the upper oceanic crust is the product of the magmatic and volcanic processes at the mid-ocean ridges and the physical and chemical evolution of the oceanic crust. To date, many terrestrial and marine surveys have attempted to describe this architecture accurately. The stratification of extrusives with abundant pillows, dike complex, lower crust, and mantle rocks from the Oman ophiolite sequence has long been considered as an analogue model of the structure of modern day fast spreading mid-ocean ridge crusts [*Penrose Conference Participants*, 1972]. Numerous submersible investigations, seismic experiments, and several basement drilling legs on the East Pacific Rise (EPR) crust have contributed in characterizing the topmost crustal construction processes and subsurface crustal structures [e.g., *Alt et al.*, 1996; *Hooft et al.*, 1996; *Karson et al.*, 2002; *Fornari et al.*, 2004]. These efforts have suggested the compatibility of the ophiolite-based oceanic crust model to *in situ* fast spreading oceanic crust [*Alt et al.*, 1996; *Wilson et al.*, 2006], yet our current view of the architecture of fast spreading crusts lacks detailed lithological description due largely to the paucity of first order, *in situ* data from the intact upper oceanic crust. Moreover, relatively few studies have attempted tying the crustal construction processes to the *in situ* crustal architecture [e.g., *Hooft et al.*, 1996].

ODP Leg 206 and Integrated Ocean Drilling Program (IODP) Expeditions 309 and 312 were the first successful drilling legs that recovered intact upper oceanic EPR crust at Hole 1256D. Although the coring suffered from low recovery rates, wire-line logs provided continuous *in situ* physical property data in Hole 1256D with excellent

quality. In particular, multi-dimensional wire-line tool strings, such as Formation MicroScanner (FMS), a resistivity logging tool, and Ultrasonic Borehole Imager (UBI), an acoustic logging tool, provide the high-resolution images of *in situ* borehole wall, providing a foundation for the reconstruction of an accurate volcanostratigraphy model [*Tominaga et al.*, 2007]. This model ties the predicted EPR crustal construction processes to the *in situ* crustal architecture. In this study, we describe how this volcanostratigraphy model complements surface geology of the EPR and elucidates upper oceanic crustal construction processes.

ODP/IODP HOLE 1256D

ODP Hole 1256D (6º 44.2' N, 91º 56.1' W) is located in the Guatemala Basin on the northeastern flank of the EPR (Figure 21). Surface magnetic anomalies suggest that the crust is 15 Ma and accreted at super-fast spreading rates (full rates ~220 km/m.y.) [*Wilson et al.*, 2006]. The total drilled sequence is 1507.1 meters beneath the seafloor (mbsf) and is composed of 751 m of extrusive lavas, 346 m of dike complex, 54 and 24 m of gabbros embedded in 24 m of dike screen, and a few meters of basaltic dikes at the bottom of the hole [*Teagle et al.*, 2006]. The ~ 50 m difference in the bottom depth of the off-axis ponded massive lava in the top of extrusives in Hole 1256D and that of Hole 1256C suggests that the flow was deposited at this site after the initiation of abyssal hill development [*McDonald et al.*, 1996]. The drilled sequence has normal mid-ocean ridge basalt composition and is similar to, and slightly more depleted than, modern EPR basalts [*Teagle et al.*, 2006]. Basaltic flows and dikes show a wide range of magmatic

fractionation, and primitive and evolved compositions are closely juxtaposed [*Teagle et al.*, 2006]. The lava sequence is much less hydrothermally altered than other basement sites (e.g. Hole 504B) [*Alt et al.*, 1996]. Isolated dikes in the extrusive rocks and the dikes in the sheeted dike complex are typically ~ 0.6 m thick and dip ~ 75º toward the NE paleo-spreading direction [*Tominaga et al.*, 2007]. The lower 60 m of the dike complex shows recrystallized, distinctive granoblastic textures that indicate contact metamorphism by gabbro intrusions. Two gabbro intervals have chilled margins against the underlying granoblastic dikes [*Teagle et al.*, 2006].

VOLCANIC STRATIGRAPHY OF HOLE 1256D UPPER OCEANIC CRUST

A downhole lithostratigraphy from drilled crustal site is necessary to understand the architecture of ocean crust. It has been challenging, however, to build an accurate lithostratigraphy model due to low recovery rates (~30 %) and the scarcity of long, continuous recovered core pieces through basement drilling. Shipboard stratigraphy is, hence, subjective due to biased recovery of rock types, fractures, and alteration types (e.g. loss of highly altered breccia materials and fracture fillings). Consequently, the shipboard volcanostratigraphy may lead to erroneous classifications of lithologic types, interpretations of crustal construction processes, and calculations of chemical fluxes from seawater-rock alteration.

As an important alternative to such shipboard stratigraphy, Tominaga et al. (2007) reconstructed a volcanostratigraphy model of Hole 1256D by analyzing electrofacies that are pseudo *in situ* images of borehole wall represented by two-

dimensional resistivity contrasts from a total of seven FMS runs. One-dimensional resistivity data (Dual LateroLog deep and shallow penetrations), Natural Gamma Ray counts, and recovered core data were used to complement the interpretation of the FMS images. Because it is continuous, the resulting volcanostratigraphy overcomes the aforementioned subjectivities while providing a detailed geophysical classification with a spatial resolution of 0.1 m. A total of ten electrofacies were suggested and named after morphologies observed in the FMS images (Table 4, Figure 24).

Morphologies on FMS images are indicative of *in situ* physical propertis which relate to extrusive morphology, fracture patterns, and alterations. For example, fractured massive flows are massive flow textures with some fracturing; fragmented flows are flows with high density of mesh-like fractures; breccias are highly brecciated rocks with a mixture of high and low resistivity patches. Pillows in FMS records show clear round rims and radial fractures similar to those observed at terrestrial outcrops. "Thin flows or thick pillows" are two classes that are difficult to differentiate because the termination (flow front) of thin flows can have a round pillow-like shape and a large (~ 1 m) pillow can appear similar to a single flow with subround boundaries at the borehole. Isolated dikes are identified based on the relative absence of fractures as massive flows with subvertical fractures that orient to the dip direction of dikes in the sheeted dike complex [*Tominaga et al.*, 2007].

The resulting volcanostratigraphy provides the first cross-sectioned view of the intact EPR upper oceanic crust, and represents the lava accumulation history at the drilled site as this part of crust moved away from the ridge axis. Lava depositions

generally follow the law of superposition. Directly atop the dike complex (at 1064 mbsf), thick layers of massive flows and breccias, intruded by isolated dikes, are observed an interval of ~100 m. Around 950 mbsf, layers of fragmented flows and thin flows become dominant, and this sequence is terminated by thick massive flows around 850 mbsf. Localized pillows accumulated for ~ 100 m between 700 – 810 mbsf with thin fragmented flow layers in between. The upper part of the hole (< 700 mbsf) is composed of thick layers of massive flows, fragmented flows, breccias, and a single off-axis massive flow (Figure 33).

WHY PILLOWS ARE LOCALIZED IN HOLE 1256D CRUST AND IMPLICATIONS FOR CRUSTAL FORMATION

The section of thick, localized pillows in Hole 1256D is a striking feature because pillows are relatively minor lava types at the EPR. We think this pillow section indicates a unique stage of crustal construction processes. How are ~100 m of pillows formed in the superfast spreading EPR crust? Why are pillows confined to the localized region among many massive flows and breccias in Hole 1256D?

The formation of pillows in the EPR crust is controlled by several factors. Broadly, lava morphology depends on spreading rate, and lobate and sheet flows are dominant flow types in fast spreading crust [*Bonatti and Harrison*, 1988; *Perfit and Chadwick*, 1998]. Pillows are ubiquitously observed in any spreading environment, suggesting that spreading rate could be one of the control parameters to determine the abundance of pillows but not the parameter to determine their formation. In detail, what

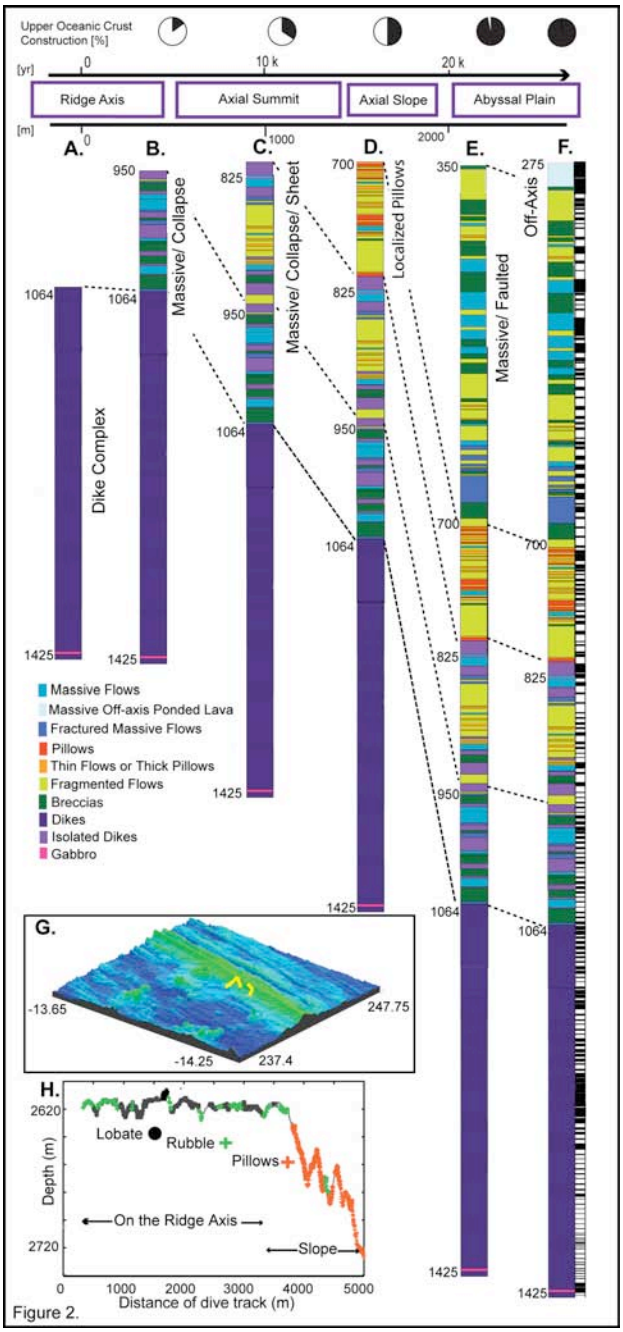

Figure 33. Hole 1256D volcanostratigraphy (A-F) and lava deposition history models. For the volcanostratigraphy model, we used "logging depth". A color code for each lithofacies is shown in the left side of the panel. Distance and age scales for lava deposition history are located atop of the stratigraphy, for which we refer the changes in morphology at the EPR 14° S. Typical axial morphology (in square) and proportion of how much of layer 2 was formed (with circle) are also shown along the scales. (A-F) Each panel shows how volcanic layer in Hole 1256D was formed. (G) Multibeam topography of the EPR 14°S with two Shinkai-6500 dive tracks in yellow lines. (H) The observations of lava flows along the two dive tracks. Solid black circles show lobate flows, green crosses show rubbles, and red crosses show pillows.

controls the formation of pillows is the combination of effusion rate, changes in lava viscosity, and slope angle [*Gregg and Fink*, 1995; *Griffiths*, 2000]. The former two parameters are strongly correlated to lava cooling during eruption and transportation. The slope angle enhances viscous/gravity flow that transport lavas [*Griffiths*, 2000]. The formation of pillow lava in the EPR is commonly interpreted as a result of the combination of low effusion rate, high viscosity, and low slope angle [*Gregg and Fink*, 1995]. Among these parameters, however, 'low slope angle' resulted from observations focused on the EPR axial summit region, and we argue that this is not applicable to the entire ridge environment. Considering the construction processes of the upper crust, the formation of pillows are associated with changes in local topography, such as rise slopes [*Francheteau and Ballard*, 1983], faults near the ridge axis [*Auzende et al.*, 1996] and other subaqueous slopes [*Umino et al.*, 2000]. If this is true for the crust of Hole 1256D, the ~ 100 m accumulation of pillows in Hole 1256D could be explained by developed faults or continuous slopes located within the on-axis environment.

To further investigate how changes in local topography form pillows, we refer to the two dives by Shinkai 6500 of the Japan Marine Science and Technology that were carried out at the western flank of the EPR at 14° S where the half spreading rates are 68 and 75 km/m.y. to the west and east, respectively (YK04-07 Dive 829, Figure 33G). We assume that this area has similar spreading conditions to the crust of Hole 1256D, where the magma supply is sufficient to suggest super-fast spreading rates, and there is a narrow axial trough, and smooth axial summit topography without caldera. These dives covered from the ridge axis to the bottom of the axial slope, where most of the upper

oceanic crust is formed. Lava flow types observed along the dive tracks (2640 – 2740 m water depth, ~ 2000 m from the ridge axis) suggest that the formation of pillows is strictly confined to the slope with > 6° inclination, such as on the axial slope (Figure 33H). Presumably, sheet flows reached the edge of the axial slope, and the lava 'dripped' down the slope forming these (elongated and knobby) pillows.

Assuming a portion of the crust recovered at Hole 1256D is analogous to the axial slope at EPR 14° S, we propose that the localized pillows in Hole 1256D were formed when the drilled site was located at the axial slope.

EPR LAVA DEPOSITION HISTORY

The volcanostratigraphy provides detailed subsurface information that represents compact, chronological records of the construction processes of the oceanic crust in this locality. We think that Hole 1256D volcanostratigraphy represents a robust model of the architecture of super fast spreading EPR crust, and hence the model makes it possible to reconstruct lava deposition history in the upper oceanic crust by compiling observational results from the drilled hole at 1256D and comparing them to surface observation at 14° S.

Surface observations have been extensively used to study how the upper part of the EPR crust was formed by the on- and off-axis volcanism. The seismic images showed a ubiquitous pattern of thickening extrusives along the EPR; the thickening occurs drastically with accumulation of lava flows within a few kilometers of the axial summit as the crust moves away from the ridge axis [*Hooft et al.*, 1996]. Late stage off-

axis eruptions also contribute to the thickening. Surface geology on the EPR provides detailed information about the topmost layer 2A construction processes, such as how lavas flow, are deposited, and are transported via lava tubes and channelized lavas within on- and off-axial environments [*Soule et al.*, 2005]. As for physical alteration within the crust, postdepositional lava burial or overlapping collapse pits are thought to start at the axial region as lavas deposit [*Fornari et al.*, 1998], and eventually the accumulated lavas were disturbed by magmatic and tectonic faulting [*Escartin et al.*, 2007].

Following these observations, we interpret the Hole 1256D volcanostratigraphy regarding where and when a lithology was formed with respect to the ridge axis (Figure 33A-F). We here use the EPR 14° S topography and Hole 1256D half spreading rate for a time-distance reference frame. The intrusive-extrusive boundary is marked by the lowermost fragmented flow at the ridge axis (1064 mbsf, Figure 33A). Thick layers of massive flows and breccias directly atop this boundary are attributed to the accumulation of high eruption rate flows and collapsed pits that may be induced by drain back or drainage of lavas (Figure 33B) [*Gregg and Chadwick*, 1996; *Sims et al.*, 2003]. Layers of fragmented flows, thinner flows, and breccias from 850 - 950 mbsf might have been tectonized by late stage faulting and/or collapsed flow lobes around the axial summit (Figure 33C). Localized pillows between 710- 800 mbsf are thought to be formed at the axial slope (1000 ~ 2000 m from the ridge axis). The crust moved from the ridge axis to the bottom of the axial slope over a period of 10 ~ 20 kyr, during which nearly 50 % of the extrusive sequence in the hole is constructed (Figure 33D). The rest of the extrusives, the sequence of thick layers of massive flows, fragmented flows, and breccias (350 -710

mbsf), were presumably formed within 2000 ~ 3000 m from the ridge axis where the long lava flows are terminated and ponded by inward facing faults [*Escartin et al.*, 2007] (Figure 33E). This location estimate is augmented by the presence of inflation cracks (subvertical veins filled by hyaloclastite; Core 1256D-21R-1, 85-140 cm at 397.6-398.2 mbsf) and seal zone (recrystallized fine-grained chilled margins of flow lobes; Core 1256D-37R-2, 12-15 cm at 501.7 mbsf) of coalesced flow lobes [*Teagle et al.*, 2006] that characterize inflated lobate sheets. These observations suggest that nearly 100% of the layer 2A construction, except for the contribution from late stage eruptions (Figure 33F), is completed within ~ 3000 m or so of ridge axis, which is consistent to the results from the latest near bottom surveys around the EPR 9° N [*Escartin et al.*, 2007] and is consistent with inferences from seismic layer 2A observations.

CHAPTER VI

CONCLUSIONS

The compilation of the Pacific M-anomalies provides a foundation of the construction of a new Pacific wide geomagnetic polarity reversal time scale (GPTS) model. This model is superior to previously suggested GPTS that is based only on the Hawaiian lineation set and statistically the most robust to date. The comparison amongst the Pacific, Atlantic, and Indian M-anomalies and polarity block models confirm the global validity of the new GPTS model (Chapter II).

The origin of the Atlantic M-anomaly smooth zone (AMSZ) was investigated based on the comparison of the synthetic anomaly profiles from the Pacific composite, Keathley, and Canary polarity blocks, the analyses of the global M-anomaly amplitudes, and previous geophysical data. Major causes of the AMSZ could be (1) the reduction of the geomagnetic field intensity, or (2) the reduction in the spreading rates resulting in non-basaltic magnetic source layer perhaps in the form of oceanic core complexes (Chapter III).

Logging data from Ocean Drilling Program Hole 1256D were analyzed qualitatively and quantitatively and used to construct a igneous stratigraphy model. This model revealed that the Hole 1256D crust largely consists of massive flows and other flows in various states of fracture along with brecciated sections. The identification of isolated dikes in the extrusive section suggests that the intrusive-extrusive transition is gradual. The steeply NE dipping, sub-parallel dike margins in the dike complex

suggested that the dikes are representation of the “sheeted dikes” typically observed in ophiolites. A quantitative volcanostratigraphy model derived from Artificial Neural Network modeling can provide a measure of the enhanced porosity and alteration structures of the Hole 1256D crust, and this modeling can be utilized for investigating alteration processes in the intact upper oceanic crust (Chapter IV).

The new volcanostratigraphy model in Hole 1256D implies the upper crustal construction processes at the East Pacific Rise, is well-represented by the evolution of lava deposition from on-axis to off-axis environments. Six constructional stages with approximate horizontal distances from the ridge axis and time scale are suggested. According to the results, 50 % of the extrusive section is formed within a few km and more than 90 % of the extrusive construction is completed within ~ 5 km from the ridge axis. This observation is consistent to the construction processes previously suggested from the seismic data (Chapter V).

REFERENCES

Abrams, L. J., R. L. Larson, T. H. Shipley, and Y. Lancelot, (1992), The seismic stratigraphy and sedimentary history of the East Mariana and Pigafetta Basins of the western Pacific, *Proc. ODP Sci. Res.*, *129*, College Station, TX (Ocean Drilling Program), 551-569.

Alt, J. C., J. Honnorez, C. Laverne, and R. Emmermann, (1986), Hydrothermal alteration of a 1 km section through the upper oceanic crust, Deep Sea Drilling Project Hole 504B: Mineralogy, chemistry, and evolution of seawater-basalt interactions, *J. Geophys. Res.*, *91*, 10309-10336.

Alt., J. C., C. Laverne, D. A. Vanko, P. Tartarotti, D. A. H. Teagle, W. Bach, E. Zuleger, J. Erzinger, J. Honnorez, P. A. Pezard, K. Becker, M. H. Salisbury, and R. H. Wilkens, (1996), Hydrothermal alteration of section of upper oceanic crust in the eastern equatorial Pacific: A synthesis of results from Site 504 (DSDP Legs 69, 70 and 83, and ODP Legs 111, 137, 140, and 148) in *Proc. ODP Sci. Res.*, *148*, edited by J. C. Alt, Kinoshita, H., Stokking, L. B., and P. J. Michael, pp. 417-434, College Station, TX (Ocean Drilling Program).

Alt, J. C. and D. A. H. Teagle, (1999), The uptake of carbon during alteration of ocean crust mineralogy and chemistry, *Geochim. Cosmocim. Acta*, *63*, 1527-1535.

Alt, J. C., (2004), Alteration of the upper oceanic crust: Mineralogy, chemistry, and processes, in *Hydrogeology of the Oceanic Lithosphere*, edited by E. E. Davis and H. Elderfield, pp. 495-533, Cambridge University Press, Cambridge, UK.

Auzende, J., V. Ballu, R. Batiza, D. Bideau, J. Charlow, M. Coprmier, Y. Fouquet, P. Geistdoerfer, Y. Lagabrielle, J. Sinton, and P. Spadea, (1996), Recent tectonic, magmatic, and hydrothermal activity on the East Pacific Rise between 17°S and 19°S: Submersible observations, *J. Geophys. Res.*, *101*, 17995-18010.

Barr, S. R., S. Revillon, T. S. Brewer, P. K. Harvey, and J. Tarney, (2002), Determining the inputs to the Mariana Subduction Factory: Using core-log integration ot reconstruct basement lithology at ODP Hole 801C, *Geochem. Geophys. Geosys.*, *3*, doi:10.1029/2001GC000255.

Bartetzko, A. R., R. Pechnig, and J. Wohlenberg, (2002), Interpretation of well-logging data to study lateral variations in young oceanic crust: DSDP/ODP Holes 504B and 896A, Costa Rica Rift, *Geological Applications of Well Logs: AAPG Methods in Exploration*, *13*, 213-228.

Bartetzko, A., H. Paulick, G. Iturrino, and J. Arnold, (2003), Facies reconstruction of a hydrothermally altered dacite extrusive sequence: Evidence from geophysical downhole logging data (ODP Leg 193), *Geochem. Geophys. Geosyst., 4*, 1087, doi:10.1029/2003GC000575.

Bartetzko, A., N. Klitzsh, G. Iturrino, S. Kaufhold, and J. Arnold, (2006), Electrical properties of hydrothermally altered dacite from the PACMANUS hydrothermal field (ODP Leg 193), *J. Volcano. Geotherm. Res.*, *152*, 109-120.

Becker, K., (1989). Measurement of the permeability of the sheeted dikes in Hole 504B, ODP Leg 111. in *Proc. ODP Sci. Res.*, *111*, edited by K. Becker, H. Sakai, C. B. Sancetta, R. B. Merrill, pp. 317-328, College Station, TX (Ocean Drilling Program).

Benaouda, D., G. Wadge, R. B. Whitmarsh, R. G. Rothwell, and C. MacLeod, (1999), Inferring the lithology of borehole rocks by applying neural network classifiers to downhole logs: An example from the Ocean Drilling Program, *Geophys. Journ. Int.*, *136*, 477-491.

Besse, J., and V. Courtillot, (2002), Apparent and true polar wander and the geometry of the geomagnetic field over the last 200 Myr, *J. Geophys. Res., 107*, doi:10.1029/2000JB000050.

Bird, D. E., S. A. Hall, K. Burke, J. F. Casey, and D. S. Sawyer, (2007), Early Central Atlantic Ocean seafloor spreading history, *Geosphere*, *3*, 283-298.

Bonatti, E., and C. G. A. Harrison, (1988), Eruption styles of basalt in oceanic spreading ridges and seamounts: Effect of magma temperature and viscosity, *J. Geophys. Res.*, *93*, 2967-2980.

Bowles, J., L. Tauxe, J. Gee, D. McMillan, and S. Cande, (2003), Source of tiny wiggles in Chron C5: A comparison of seimentary relative intensity and marine magnetic anoamlies, *Geochem. Geophys. Geosys.*, *4*, doi:10.1029/2002GC000489.

Cande, S. C., and D. V. Kent, (1976), Constraints imposed by the shape of marine magnetic anomalies on the magnetic source, *J. Geophys. Res.*, *81*, 4157-4162.

Cande, S. C., R. L. Larson, and J. L. Labrecque, (1978), Magnetic lineations in the Pacific Jurassic quiet zone, *Earth Planet. Sci. Lett*, *41*, 434-440.

Cande, S. C., and D. V. Kent, (1992a), A new geomagnetic polarity time scale for the Late Cretaceous and Cenozoic, *J. Geophys. Res.*, *97*, 13917-13951.

Cande, S. C., and D. V. Kent, (1992b), Ultrahigh resolution marine magnetic anomaly profiles- A record of continuous paleointensity variations? *J. Geophys. Res.*, *97*, 15075-15083.

Cande, S. C., and D. V. Kent, (1995), Revised calibration of the geomagnetic polarity timescale for the Late Cretaceous and Cenozoic, *J. Geophys. Res.*, *100*, 6093-6095.

Cannat, M., (1996), How thick is the magnetic crust at slow spreading oceanic ridges, *J. Geophys. Res.*, *191,* 2847-2857.

Channell, J. E. T., E. Erba, M. Nakanishi, and K. Tamaki, (1995a), Late Jurassic-Early Cretaceous time scales and oceanic magnetic anomaly block models, in *Geochronology,Time Scales, and Global Stratigraphic Correlation, SEPM Special Publication, 54*, 51-63, Soc. Econ. Mineral. Petrol., Tulsa, OK.

Channell, J. E. T., E. Cecca, and E. Erba, (1995b), Correlations of Hauterivian and Barremian (Early Cretaceous) stage boundaries to polarity chrons, *Earth Planet. Sci. Lett*, *134*, 125-140.

Channell, J. E. T., E. Erba, G. Muttoni, and F. Tremolada, (2000), Early Cretaceous magnetic stratigraphy in the APTICORE drill core and adjacent outcrop at Cismon (Southern Alps, Italy), and correlation to the proposed Barremian-Aptian boundary stratotype, *Geol. Soc. Amer. Bull.*, *112*, 1430-1443.

Cooper, A. K., M. S. Marlow, and D. W. Scholl, (1976), Mesozoic magnetic lineations in the Bering Sea marginal basin, *J. Geophys. Res., 81*, 1916-1934.

Denham, C. R., and H. Shouten (1979), On the likelihood of mixed polarity in oceanic basement drill cores, in *DSDP Results in the Atlantic Ocean: Ocean Crust, Maurice Ewing Symp.*, *2,* edited by M. Talwani, C. G. A. Harrison, D. E. Hayes, pp.160-165, AGU, Washington DC.

Dick, J., B., M. A. Tivey, and B. E. Tucholke, (2008), Plutonic foundation of a slow-spreading ridge segment: Oceanic core complex at Kane Megamullion, 23º 30'N, 45º 20'W, *Geochem. Geophys. Geosys.*, *Q05014*, doi:10.1029/2006GC001533.

Dowla, F. U., and L. L. Rogers, (1995), Solving Problems in *Environmental Engineering and Sciences with Artigicial Neural Networks*, Massachusetts Institute of Technology Press, Boston.

Dyment, J., S. C. Cande and J. Arkani-Hamed, (1994), Skewness of marine magnetic anomalies created between 85 and 40 Ma in the Indian Ocean, *J. Geophys. Res.*, 99, 24121-24134.

Escartin, J., S. A. Soule, D. J. Fornari, M. A. Tivey, H. Schouten, H., and M. R. Perfit, (2007), Interactions between faults and lava flows along the East Pacific Rise crest (9°10'-50'N): Implications for upper oceanic crust construction, *Geochem. Geophys. Geosys.*, *Q06005*, doi:10.1029/2006GC001399.

Escartin, J., D. K. Smith, J. Cann, H. Schouten, C. H. Langmuir, and S. Escrig, (2008), Central role of detachment faults in accretion of slow-spreading oceanic lithosphere, *Nature*, *455*, 790-794.

Fisher, A. T., (2004), Rates of flow and patterns of fluid circulation, in *Hydrogeology of the Oceanic Lithosphere,* edited by E. Davis and H. Elderfield, 337-375, Cambridge University Press, Cambridge, UK.

Fisher, A. T., and R. P. Von Herzen (2005), Models of hydrothermal circulation within 106 Ma seafloor: Constraints on the vigor of fluid circulation and crustal properties, below the Madeira Abyssal Plain, *Geochem. Geophys. Geosys.,* doi: 10.1029/2005GC001013.

Fisher, N. I., T. Lewis, and B. J. J. Embleton, (1987), *Statistical Analysis of Spherical Data*, Cambridge University Press, Cambridge, UK.

Fornari, D. J., R. M. Haymon, M. R. Perfit, T. K. P. Gregg, and M. H. Edwards, (1998), Geological characteristics and evolution of the axial zone on fast spreading mid-ocean ridges: Formation of an axial summit trough along the East Pacific Rise, 9°-10° N, *J. Geophys. Res.*, *103*, 9827-9855.

Fornari, D., M. Tivey, H. Schouten, M. Perfit, D. Yoerger, A. Bradley, M. Edwards, R. Haymon, D. Scheirer, K. Von Damm, T. Shank, and A. Soule, (2004), Submarine lava flow emplacement at the East Pacific Rise 9°50N: Implications for uppermost ocean crust stratigraphy and hydrothermal fluid circulation, in *Mid-Ocean Ridges : Hydrothermal Interactions between the Lithosphere and Oceans, Geophysical Monograph Series*, *148*, edited by German C. R., J. Lin, and L. M. Parsons, pp. 187-218, American Geophysical Union, Washington DC.

Francheteau, J., and R. D. Ballard, (1983), The East Pacific Rise near 21ºN, 13ºN, and 20ºS: Inferences for along-strike variability of axial processes of the Mid-Ocean Ridge, *Earth Planet. Sci. Lett.*, *64*, 93-116.

Fullerton, L. G., W. W. Sager, and D. W. Handschumacher, (1989), Late Jurassic-Early Cretaceous evolution of the eastern Indian Ocean adjacent to northwest Australia, *J. Geophys. Res., 94*, 2937-2953.

Gass I. G., (1960), The geology and mineral resources of the Dhali area. *Mem. Cypru Geol. Surv. Dept,. 4*, 116.

Gillis, K. M., and K. Sapp, (1997), Distribution of porosity in a section of upper oceanic crust exposed in the Troodos Ophiolite, *J. Geophys. Res.*, *102*, 10133-10149.

Gladczenko, T. P., K. Hinz, O. Eldholm, H. Meyer, S. Neben, and J. Skogseid, (1997), South Atlantic volcanic margins, *J. Geol. Soc. London., 154,* 465-470.

Gradstein, F. M., J. G. Ogg, and A. G. Smith, (2005), *A Geological Time Scale 2004*, Cambridge University Press, Cambridge, UK.

Goutorbe, B., F. Lucazeau, and A. Bonneville, (2006), Using neural networks to predict thermal conductivity from geophysical well logs, *Geophys. J. Int., 166,* 115-125.

Gregg, T. K. P., and J. H. Fink, (1995), Quantification of submarine lava-flow morphology through analog experiments, *Geology*, *23*, 73-76.

Gregg, T. K. P., and W. W. Chadwick, (1996), Submarine lava-flow inflation: A model for the formation of lava pillars, *Geology*, *24*, 981-984.

Griffiths, R. W., (2000), The dynamics of lava flows, *Ann. Rev. Fluid Mech.*, *32*, 477-518.

Grow, J. A., and R. G. Markl, (1977), IPOD-USGS multichannel seismic reflection profile from Cape Hatteras to the Mid-Atlantic Ridge, *Geology*, *5*, 625-630.

Gubbins, D., (2004), *Time Series Analysis and Inverse Theory for Geophysicists*, Cambridge University Press, Cambridge, UK.

Gurevich, N. I., S. A. Merkur'ev, and A. A. Sbel'skaya (2006), Evolution of the Southern part of the Canada Basin (Arctic Ocean) based on magnetometric data, *Doklady Earth Sciences (Doklady Akademii Nauk)*, *407*, 308-311.

Haggas, A. L., T. S. Brewer, P. K. Harvey, and G. I. Iturrino, (2001), Relocating and orientating cores by the integration of electrical and optical images: a case study from Ocean Drilling Program Hole 735B, *J. Geol. Soc. Lond.*, *158*, 615-623.

Haggas, S. L., T. S. Brewer, and P. K. Harvey, (2002), Architecture of the volcanic layer from the Costa Rica Rift, constraints from core-log integration, *J. Geophys. Res.*, *107*, doi:10.1029/2001JB000147.

Hagan, M. T., H. B. Demuth, and M. Beale, *Neural Network Design*, (1996), PWS Publishing Company, Boston.

Handshumacher, D. W., W. W. Sager, T. W. C. Hilde, and D. R. Bracey, (1988), Pre-Cretaceous tectonic evolution of the Pacific plate and extension of the geomagnetic polarity reversal time scale with implications for the origin of the Jurassic Quiet Zone, *Tectononphysics*, *155*, 365-380.

Harland, W. B., A. V. Cox, P. G. Llewellyn, C. A. G. Pickton, A. G. Smith, and R. Walters, (1982), *A Geologic Time Scale*, Cambridge University Press, Cambridge, UK.

Harland, W. B., R. L. Armstrong, A. V. Cox, L. E. Craig, A. G. Smith, and D. G. Smith, (1989), A Geologic Time Scale, Cambridge University Press, Cambridge, UK.

Hayes, D. E., and P. D. Rabinowitz, (1975), Mesozoic magnetic lineations and the magnetic quiet zone off Northwest Africa, *Earth Planet. Sci. Lett*, *28*, 105-115.

Heirtzler, J. R., G. O. Dickson, E. M. Herron, W. C. Pitman, and X. Pichon, (1968), Marine magnetic anomalies, geomagnetic field reversals, and motions of the ocean floor, *J. Geophys. Res.*, *73*, 2119-2136.

Hooft, E. E. E., H. Schouten, and R. S. Detrick, (1996), Constraining crustal emplacement processes from the variation in seismic layer 2A thickness at the East Pacific Rise, *Earth Planet. Sci. Lett.*, *142*, 289-309.

Hosford, A., M. A. Tivery, T. Matsumoto, H. Dick, H. Schouten, and H. Kinoshita, (2003), Crustal magnetization and accretion at the Southwest Indian Ridge near the Atlantis II fracture zone, 0-25 Ma, *J. Geophys. Res.*, *108*, doi:10.1029/2001JB000604.

Johnson, H. P., and P. E. Pariso (1993), Variations in oceanic crustal magnetization: Systematic changes in the last 160 million years, *J. Geophys. Res.*, *98*, 435-445.

Karson, J. A., E. M. Klein, S. D. Hurst, C. E. Lee, P. A. Rivizzigno, D. Cureqitz, A. R. Morris, D. J. Miller, R. G. Verga, G. L. Christeson, B. Cushman, J. M. O'Neill, J. G. Brophy, K. M. Gillis, M. A. Stewart, and A. L. Sutton, (2002), Structure of uppermost fast-spread oceanic crust exposed at the Hess Deep Rift: Implications for subaxial processes at the East Pacific Rise, *Geochem. Geophys. Geosys.*, *3*, 2001GC000155

Kent, D. V., and B. M. Honnerez, N. D. Opdyke, and J. P. Fox (1978), Magnetic properties of dredged oceanic gabbros and the source of marine magnetic anomalies, *Geophys. J. Royal. Astron.*, *55*, 513-537.

Klitgord, K. D., and H. Schouten, (1986), Plate kinematics of the central Atlantic, in *The Geology of North America, Volume M., The Western North Atlantic Region,* edited by P. R. Vogt and B. E. Tucholke, pp. 351-378, Geological Society of America, Boulder, CO.

Kohonen, T., (1987), Adaptive, associative, and self-organizing functions in neural computing, *Applied Optics*, *26*, 4910-4918.

Koppers, A. P., H. Staudigel, and R. A. Duncan, (2003), High-resolution $^{40}Ar/^{39}Ar$ dating of the oldest oceanic basement basalts in the western Pacific Basin, *Geochem. Geophys. Geosys.*, doi.10.1029/2003GC000574.

Larson, R. L., and W. C. Pitman, (1973), World-wide correlation of Mesozoic magnetic anomalies, and its implications, *Geol. Soc. Amer. Bull.*, *83*, 3645-3661.

Larson, R. L., (1975), Late Jurassic sea floor spreading in the eastern Indian Ocean, *Geology*, 69-71.

Larson, R. L., and T. W. C. Hilde, (1975), A revised time scale of magnetic reversals for the Early Cretaceous and Late Jurassic, *J. Geophys. Res.*, *80*, 2586-2594.

Larson, R. L., (1977), Early Cretaceous breakup of Gondwanaland off western Australia, *Geology*, *5*, 57-60.

Larson, R. L., and W. W. Sager, (1992), Skewness of magnetic anomalies M0 to M29 in the northwestern Pacific, *Proc. ODP Sci. Res.*, 129, College Station, TX (Ocean Drilling Program), 471-481.

Link, C. A., and S. Blundell, (2003), interpretation of shallow stratigraphic facies using a self-organizing neural network, *Modern Appr. in Geophys.*, *21*, 215-230.

Lizarralde, D., J. B. Gaherty, J. A. Collins, G. Hirth, and S. D. Kim, (2004), Spreading-rate dependence of melt extraction at mid-ocean ridges from mantle seismic refraction data, *Nature*, *432,* 744-747.

Lonsdale, P., and F. N. Spiess, (1980), Deep-tow observations at the East Pacific Rise, 8° 45 N, and some interpretations, *Deep-Sea Res.*, *54*, 43-62.

Ludden, J. N., (1992), Radiometric age determinations for basement from Sites 765 and 766, Argo Abyssal Plain and northwestern Australian margin, *Proc. ODP Sci. Res.*, *123*, 557-559.

Macdonald, K. C., P. J. Fox, R. T. Alexander, R. Pockalny, and P. Gente, (1996), Volcanic growth faults and the origin of Pacific abyssal hills, *Nature, 380*, 125-129.

McCarthy, J., J. C. Mutter, J. L. Morton, N. H. Sleep, and G. A. Thompson, (1988), Relic magma chamber structures preserved within the Mesozoic North Atlantic crust? *Geol. Soc. Amer. Bull.*, *100*, 1423-1436.

McElhinny, M., and R. L. Larson (2003), Jurassic dipole low defined from land and sea data, *EOS*, *84*, 362-366.

Milner, S. C., A. P. Le Roex, and J. M. O'Connor, (1995), Age of Mesozoic igneous rocks in northwestern Namibia, and their relationship to continental breakup, *J. Geol. Soc., London*, *152*, 97-104.

Moore, J. G., (2001), Density of basalt core from Hilo drill hole, Hawaii, *J. Volc. Geothrm. Res.*, *112*, 221-230.

Moritz, E., S. Bornholdt, H. Westphal, and M. Meschede, (2000), Neutral network interpretation of LWD data (ODP Leg 170) confirms complete sediment subduction at the Costa Rica convergent margin, *Earth Planet. Sci. Lett.*, *174*, 301-312.

Morris, E., R. S. Detrick, T. A. Minshull, J. C. Mutter, R. S. White, W. Su, and P. Buhl, (1993), Seismic structure of oceanic crust in the western North Atlantic, *J. Geophys. Res.*, *98*, 13879-13904.

Müller, D., W. R. Roest, and J-Y. Royer, (1998), Asymmetric sea-floor spreading caused by ridge plume interactions, *Nature*, *396*, 455-459.

Nakanishi, M., K. Tamaki, and K. Kobayashi, (1989), Mesozoic magnetic anomaly lineations and seafloor spreading history of the northwestern Pacific, *J. Geophys. Res.*, *94*, 15437-15462.

Nakanishi, M., K. Tamaki, and K. Kobayashi, (1992), Magnetic anomaly lineations from late Jurassic to Early Cretaceous in the west-central Pacific Ocean, *Geophys. J. Int*, *109*, 701-719.

Nakanishi, M., W. W. Sager, and A. Klaus., (1999), Magnetic lineations within Shatsky Rise, northwest Pacific Ocean: Implications for hot spot-triple junction interaction and oceanic plateau formation, *J. Geophys. Res.*, *104*, 7539-7556.

Nielsen, S. G., M. Rehkämper, D. A. H. Teagle, D. A. Butterfield, J. C. Alt, and A. N. Halliday, (2006), Hydrothermal fluid fluxes calculated from the isotopic mass balance of thallium in the oceanic crust, *Earth Planet Sci. Lett., 251*, 120, 133.

ODP Leg 176 Scientific Party, (1998), Logging Summary, http://www.ldeo.columbia.edu/BRG/ODP/ODP/LEG_SUMM/176/leg176.html

Ogg, J. G., and J. Gutowski, (1995), Oxfordian Magnetic Polarity Time Scale, in *Proceedings of the 4th International Congress on Jurassic Stratigraphy and Geology, Geo. Res. Forum* vols. 1-2, edited by A.C. Riccardi, pp. 406-414, Trabs-Tec Publ. Ltd., Zurich, Switzerland.

Oufi, O., M. Cannat, H. Horen, (2002), Magnetic properties of variably sepentinized abyssal peridotites, *J. Geophys. Res.*, *107*, doi:10.1029/2001JB000549.

Palfy, J., P. L. Smith, and J. K. Mortensen, (2000), A U-Pb and $^{40}Ar/^{39}Ar$ time scale for the Jurassic, *Can. J. Earth Sci*, *37*, 923-944.

Parker, R. L., and S. P. Huestis, (1974), The inversion of magnetic anomalies in the presence of topography, *J. Geophys. Res.*, *79*, 1587-1593.

Penrose Conference Participants, (1972), Penrose field conference on ophiolites, *Geotimes*, *17*, 24 – 25.

Perfit, M. R., and W. W. Chadwick, (1998), Constraints from volcanological and geochemical investigations, in *Faulting and Magmasitsm at Mid-Ocean Ridges, Geophysical Monograph Series, 106*, edited by R. W. Buck, P. T. Delaney, J. A. Karson, and Y. Lagabrielle, pp. 59-115, American Geophysical Union, Washington DC.

Perfit, M. R., J. R. Cann, D. J. Fornari, J. Engles, D. K. Smith, W. Ian Ridley, and M. H. Edwards, (2003), Interaction of sea water and lava during submarine eruptions at mid-ocean ridges, *Nature*, *426*, 62-65.

Petronotis, K. E., R. G. Gordon, and G. D. Acton, (1992), Determining paleomagnetic poles and anomalous skewness from marine magnetic anomaly skewness data from a single plate, *Geophys. J. Int*, *109*, 209-224.

Pezard, P. A., (1990), Electrical properties of Mid-ocean Ridge basalt and implications for the structure of the upper oceanic crust in Hole 504B, *J. Geophys. Res.*, *95*, 9237-9264.

Plank, T., Ludden, J.N., Escutia C., et al., (2000), Proc. ODP, Init. Repts., *185*, College Station, TX (Ocean Drilling Program), doi:10.2973/odp.proc.ir.185.2000.

Plessis, A. D., and E. S. W. Simpson, (1974), Magnetic anomalies associated with the southeastern continental margin of south Africa, *Marine Geophys. Res.*, *2*, 99-110.

Pockalny, R. A., and R. L. Larson, (2002), Implications for crustal accretion at fast spreading ridges from observations in Jurassic oceanic crust in the western Pacific, *Geochem. Geophys. Geosys.*, *3*, doi:10.1029/2001GC000274.

Pringle, M. S., H. Staudigel, R. A. Duncan, D. M. Christie, and ODP Leg 143 and 144 Science Staff, (1993), Ar^{40}/Ar^{39} ages for basement lavas at Resolution, MIT, and Wodejebato Guyots compared with magneto- and bio-stratigraphic results from ODP Legs 143/144: *EOS Trans. AGU, 73,* 353.

Pringle, M., L. Chambers, and J. G. Ogg, (2003), Synchronicity of volcanism on Ontong Java and Manihiki Plateau with global oceanographic events?, EGS-AGU-EUG Joint Assembly, Abstract #13768.

Pryzbyiski, P. A., and J. G. Ogg, (2007), Calibration of pre-M25 marine magnetic anomalies: magnetic polarity composite of Late Callovian through Kimmerdigdian, *EOS Trans. AGU, 88,* Abstract T13A-1130.

Purdy, G. M., L. S. Kong, G. L. Christeson, and S. C. Solomon, (1992), Relationship between spreading rate and the seismic structure of mid-ocean ridges, *Nature*, *355*, 815-817.

Rabinowitz, P. D., M. F. Coffin, and D. Falvey, (1983), The separation of Madagascar and Africa, *Science*, *220*, 67-69.

Ramana, M. V., R. R. Nair, K. V. L. N. S. Sarma, T. Ramprasad, K. S. Krishna, V. Subrahmanyan, M. D'Cruz, C. Subrahmanyam, C. Paul, A. S. Sunrahmanyam, and D. V. Chandra Sekhar, (1994), Mesozoic anomalies in the Bay of Bengal, *Earth Planet Sci. Lett.*, *121*, 469-475.

Ramana, M. V., T. Ramprasad, and M. Desa, (2001), Seafloor spreading magnetic anomalies in the Enderby Basin, East Antarctica, *Earth Planet Sci. Lett.*, *191*, 241-255.

Ranero, C. R., E. Banda, and P. Buhl, (1997), The crustal structure of the Canary Basin: Accretion processes at slow spreading centers, *J. Geophys. Res.*, v. *102*, 10185-10201.

Ranero, C. R., and T. J. Reston, (1999), Detachment faulting at ocean core complexes, *Geology*, 11, 983-986.

Révillon, S., S. R. Barr, T. S. Brewer, P. K. Harvey, and J. Tarney, (2002), An alternative approach using integrated gamma-ray and geochemical data to estimate the inputs to subduction zones from ODP Leg 185, Site 801, *Geochem. Geophys.Geosys*, *3*, doi :10.1029/2002GC000344.

Rider, M. H., (1996), *The Geological Interpretation of Well Logs*, Gulf Publishing, Houston, TX.

Robb, M. S., B. Taylor, and A. M. Goodlife, (2005), Re-examination of the magnetic linations of the Gascoyne and Cuvier Abyssal Plains, off NW Australia, *Geophys. J. Int*, *163*, 42-55.

Roeser, H. A., C. Steiner, B. Schreckenberger, and M. Block, (2002), Structural development of the Jurassic Magnetic Quiet Zone off Morocco and identification of Middle Jurassic magnetic linations, *J. Geophys. Res.*, *107*, doi:10.1029/2000JB000094.

Roest, W. R., J. J. Danobeitia, J. Verhoef, and B. J. Collette, (1992), Magnetic anomalies in the Canary basin and the Mesozoic evolution of the central north Atlantic, *Mar. Geophys. Res.*, *14*, 1-24.

Rybakov, M., V. Goldshmidt, L. Fleischer, and Y. Ben-Gai, (2000), 3-D gravity and magnetic interpretation for the Hifa Bay area (Israel), *J. Appl. Geophys.*, *44*, 353-367.

Sager, W. W., L. G. Fullerton, R. T. Buffler, and D. W. Handschumacher, (1992), Argo Abyssal Plain magnetic lineations revisited: Implications for the onset of seafloor spreading and tectonic evolution of the eastern Indian Ocean, *Proc. ODP Sci. Res.*, *123*, College Station, TX (Ocean Drilling Program), 659-669.

Sager, W. W., C. J. Weiss, M. A. Tivey, and H. P. Johnson, (1998), Geomagnetic polarity reversal model of deep-tow profiles from the Pacific Jurassic Quiet Zone, *J. Geophys. Res.*, *103*, 5269-5286.

Sauter, D., M. Cannat, and V. Mendel, (2008), Magnetization for 0-26.5 Ma seafloor at the ultraslow spreading Southwest Indian Ridge, 61-67E, *Geochem. Geophys. Geosys.*, *9*, Q04023, doi:04010.01029/02007GC001764.

Schouten, H., and S. C. Cande, (1976), Paleomagnetic poles from marine magnetic anomalies, *J. Geophys. Res.*, *44*, 567-575.

Schouten, H., and K. D. Klitgord, (1977), Map showing Mesozoic magnetic anomalies: Western North Atlantic: U. S. Geol. Surv. Misc. Field Studied Map MF-195, Scale 1:2000000.

Schouten, H., and K. D. Klitgord, (1982), The memory of the accreting plate boundary and the continuity of fracture zones, *Earth Planet. Sci. Lett.*, *59*, 255-266.

Sims, K. W. W., J. Blichert-Toft, D. J. Fornari, M. Perfit, S. J. Goldstein, P. Johnson, D. J. DePaolo, S. R. Hart, M. T. Murrell, P. J. Michael, G. D. Layne, and L. A. Ball, (2003), Aberrant youth: Chemical and isotopic constraints on the origin of off-axis lavas from the East Pacific Rise, 9° -10° N, *Geochem. Geophys. Geosys.*, 4, doi:10.1029/2002GC000443.

Smith, D. K., J. Escartin, H. Schouten, and J. R. Cann, (2008), Fault rotation and core complex formation: Significant processes in seafloor formation at slow-spreading mid-ocean ridges (Mid-Atlantic Ridge, 13°-15°N), *Geochem. Geophys. Geosysys.*, *Q03003, doi:10.1029/2007GC001699*.

Smith, G. M. (1990), The magnetic structure of the marine basement, *Aquatic Sciences*, *2*, 205-227.

Smith, W. H. F., and D. T. Sandwell, (1997), Global seafloor topography from satellite altimetry and ship depth soundings, *Science*, *277*, 1957-1962.

Soule, S. A., D. J. Fornari, M. R. Perfit, M. A. Tivey, W. I. Ridley, and H. Schouten, (2005), Channelized lava flows at the East Pacific Rise crest 9° -10° N: The importance of off-axis lava transport in developing the architecture of young oceanic crust, *Geochem. Geophys. Geosys.*, 6, doi:10.1029/2005GC000912.

Speranza, F., S. Satolli, E. Mattioli, and F. Calamita, (2005), Magnetic stratigraphy of Kimmeridgian-Aptian sections from Umbria-Marche (Italy): New details on the M polarity sequence, *J. Geophys. Res.*, *110*, doi:10.1029/2005JB003884.

Sundvik, M. T., and R. L. Larson, (1988), Seafloor spreading history of the western North Atlantic Basin derived from the Keathley sequence and computer graphics, *Tectononphysics*, *155*, 49-71.

Talwani, M., and J. R. Heirtzler, (1964), Computation of magnetic anomalies caused by two-dimensional structures of arbitrary shape, in *Computers in the Mineral Industries,* edited by G. A. Parks, Stanford Univ. Press, Stanford, CA.

Taylor, B., and Shipboard Scientific Party, 1990, Introduction, in *Proc. ODP, Init. Repts.*, *126*, edited by Taylor, B. and K. Fujioka, pp. 5-11, College Station, TX (Ocean Drilling Program).

Tauxe, L., (2006), Long-term trends in paleointensity: The contribution of DSDP/ODP submarine basaltic glass collections, *Phys. Earth Planet Int.*,156, 223-241.

Teagle, D. A. H., J. C. Alt, and A. N. Halliday, (1998), Tracing the chemical evolution of fluids during hydrothermal recharge: Constraints from anhydrite recovered in ODP Hole 504B, *Earth Planet. Sci. Lett.,155*, 167-182.

Teagle, D. A. H., M. J. Bickle, and J. C. Alt, (2003), Recharge flux to ocean-ridge black smoker systems: A geochemical estimate from ODP Hole 504B, *Earth Planet. Sci. Lett., 210*, 81-89.

Teagle, D.A.H., J. C. Alt, S. Umino, S. Miyashita, N. R. Banerjee, D. S. Wilson, and the Expedition 309/312 Scientists, (2006), *Proceedings of the Integrated Ocean Drilling Program, 309/312*: Washington, DC (Integrated Ocean Drilling Program Management International, Inc.), doi:10.2204/iodp.proc.309312.101.2006.

Tivey, M. A., and H. P. Johnson (1987), The central anomaly magnetic high: Implications for ocean crust construction and evolution, *J. Geophys. Res.*, *92*, 12685-12694.

Tominaga, M., D. A. H. Teagle, J. C. Alt, and S. Umino, Determination of the volcanostratigraphy of oceanic crust ormed at superfast spreading ridge: Electrofacies analyses of ODP/IODP Hole 1256D, *Geochem. Geophys. Geosys., in press.*

Tominaga, M., D. A. H. Teagle, J. C. Alt, and S. Umino, (2007), Determination of volcanostratigraphy of ODP/IODP Hole 1256D: Quantitative and qualitative core-Log integration, [abs.]: Eos Transactions, American Geophysical Union, *88*, 52.

Tominaga, M., W. W. Sager, M. A. Tivey, and S.-M. Lee, (2008), Deep-tow magnetic anomaly study of the Pacific Jurassic Quiet Zone and implications for the geomagnetic polarity reversal timescale and geomagnetic field behavior, *J. Geophys. Res.*, 113, doi:10.1029/2007JB005527.

Umino, S., P. W. Lipman, and S. Obata, (2000), Subaqueous lava flow lobes, observed on ROV KAIKO dives off Hawaii, *Geology*, *28*, 503-506.

Umino, S., S. Obata, P. Lipman, J. R. Smith, T. Shibata, J. Naka, and F. Trusdell, (2002), Emplacement and inflation structures of submarine and subaerial Pahoehoe lavas from Hawaii, *Geophys. Monog.*, *128*, 85-101.

Verhoef, J., and R. D. Scholten, (1983), Cross-over analysis of marine magnetic anomalies, *Marine Geophys. Res.*, *5*, 421-435.

Vine, F. J., and D. H. Matthews, (1963), Magnetic anomalies over oceanic ridges, *Nature*, *199*, 47-949.

Vogt, P. R., O. E. Avery, E. D. Schneider, C. N. Anderson, and D. R. Bracey, (1969), Discontinuities in sea floor spreading, *Tectonophysics*, *8*, 285-317.

Vogt, P. R., C. N. Anderson, and D. R. Bracey, (1971), Mesozoic magnetic anomalies, sea-floor spreading, and geomagnetic reversals in the southwestern North Atlantic, *J. Geophys. Res.*, *76*, 4796-4923.

Vogt, P. R., G. L. Johnson, T. L. Holcombe, J. G. Gilg, and O. E. Avery, (1971), Episodes of sea-floor spreading recorded by the North Atlantic basement, *Tectonophysics*, *12*, 211- 234.

Williams, C. M., M. A. Tivey, B. E. Tucholke, and H. J. B. Dick (2005), The nature of a magnetic polarity boundary in the lower crust and upper mantle at kane Megamullion, *EOS Trans. AGU 86 (52), Fall Meet. Suppl.,* Abstract T-T30.

Williams, T., and C. Broglia, (2006), Hole U1256D, Exp 309/312 (re-entry, phase 3 logging): FMS Processing Report. Available at IODP Log database http://iodp.ldeo.columbia.edu/DATA/

Wilson, D. S., (1996), Fastest known spreading on the Miocene Cocos-Pacific plate boundary. *Geophys. Res. Lett.,* 23, 3003-3006.

Wilson, D. S., D. A. H. Teagle, J. C. Alt, N. R. Banerjee, S. Umino, S. Miyashita, G. D. Acton, R. Anma, S. R. Barr, A. Belghoul, J. Carlut, D. M. Christie, R. M. Coggon, K. M. Cooper, C. Cordier, L. Crispini, S. R. Durand, F. Einaudi, L. Galli, Y. Gao, J. Geldmacher, L. A. Gilbert, N. W. Hayman, E. Herrero-Bervera, N. Hirano, S. Holter, S. Ingle, S. Jiang, U. Kalberkamp, M. Kerneklian, J. Koepke, C. Laverne, H. L. Lledo Vasquez, J. Maclennan, S. Morgan, N. Neo, H. J. Nichols, S. Park, M. K. Reichow, T. Sakuyama, T. Sano, R. Sandwell, B. Scheibner, C. E. Smith-Duque, S. A. Swift, P. Tartarotti, A. A. Tikku, M. Tominaga, E. A. Veloso, T. Yamazaki, S. Yamasaki, and C. Ziegler, (2006), Drilling to gabbro in intact ocean crust, *Science*, *312*, 1016-1020.

Wilson, R. A. M., (1959), The geology and mineral resources of the Xeros-Troodos area. *Mem. Cyprus Geol. Surv. Dept.* 1, 135 p.

Zhou, W., R. Van der Voo, D. R. Peacor, D. Wang, and Y Zhang (2001), Low-temperature oxidation in MORB of titanomagnetite to titanomaghemite: A gradual process with implications for marine magnetic anomaly amplitudes, *J. Geophys. Res., 106*, 6409-6421.

APPENDIX A

Appendix A. Atlantic magnetic profiles and magnetization parameters

Keathley lineations

NGDC#	Cruise ID	Anomaly	Index	site lat	site lon	pole lat	pole lon	PI	PD	sli
09100001	Keathley	M2	k2	32.7	297.0	71.9	193.5	45.3	-19.8	190
		M5	k2	32.7	295.0	69.5	193.5	44.9	-22.6	190
		M15	k2	32.7	293.0	71.0	181.0	41.7	-19.3	190
		M22	k2	32.7	290.0	73.7	158.7	37.8	-13.1	190
		M2	k4	33.0	297.0	71.9	193.5	45.7	-19.9	190
		M5	k4	33.0	295.0	69.5	193.5	45.3	-22.7	190
		M15	k4	33.0	293.0	71.0	181.0	42.1	-19.4	190
		M22	k4	33.0	290.0	73.7	158.7	38.3	-13.1	190
		M2	k5	33.3	297.0	71.9	193.5	46.1	-20.0	190
		M5	k5	33.3	295.0	69.5	193.5	45.7	-22.7	190
		M15	k5	33.3	293.0	71.0	181.0	42.5	-19.4	190
		M22	k5	33.3	290.0	73.7	158.7	38.7	-13.2	190
		M2	k6	34.0	297.0	71.9	193.5	46.9	-20.1	190
		M5	k6	34.0	295.0	69.5	193.5	46.4	-22.9	190
		M15	k6	34.0	293.0	71.0	181.0	43.4	-19.5	190
		M22	k6	34.0	290.0	73.7	158.7	39.6	-13.2	190
		M2	k7	33.7	297.0	71.9	193.5	46.5	-20.0	190
		M5	k7	33.7	295.0	69.5	193.5	46.1	-22.8	190
		M15	k7	33.7	293.0	71.0	181.0	42.9	-19.5	190
		M22	k7	33.7	290.0	73.7	158.7	39.2	-13.2	190
03030005	TAG71	M2	kr1	33.0	297.0	71.9	193.5	45.7	-19.9	190
		M5	kr1	33.2	295.0	69.5	193.5	45.6	-22.7	190
		M15	kr1	33.4	293.0	71.0	181.0	42.7	-19.5	190
		M22	kr1	34.0	290.0	73.7	158.7	39.6	-13.2	190
03030015	TAG70	M2	kr2	32.7	297.0	71.9	193.5	45.3	-19.8	190
		M5	kr2	32.9	295.0	69.5	193.5	45.2	-22.6	190
		M15	kr2	33.0	293.0	71.0	181.0	42.1	-19.4	190
		M22	kr2	33.7	290.0	73.7	158.7	39.2	-13.2	190
Canary lineations										
3030005	TAG71	M2	m9	22.0	332.0	52.0	261.6	48.1	-41.6	10
		M5	m9	21.5	335.0	47.9	263.3	46.6	-46.1	10
		M15	m9	21.0	337.0	49.3	262.6	44.0	-44.2	10
		M22	m9	20.5	340.0	54.0	260.3	39.5	-38.7	10
		M2	m10	23.0	332.0	52.0	261.6	49.0	-42.0	10
		M5	m10	22.5	335.0	47.9	263.3	47.5	-46.5	10
		M15	m10	22.0	337.0	49.3	262.6	44.9	-44.6	10
		M2	m12	24.0	332.0	52.0	261.6	49.8	-42.4	10
		M5	m12	23.5	335.0	47.9	263.3	48.3	-46.9	10
		M15	m12	23.0	337.0	49.3	262.6	45.8	-44.9	10
		M22	m12	22.5	340.0	54.0	260.3	41.6	-39.3	10
3030015	TAG70	M2	m8	21.5	332.0	52.0	261.6	47.7	-41.4	10
		M5	m8	21.0	335.0	47.9	263.3	46.2	-45.9	10
		M15	m8	20.5	337.0	49.3	262.6	43.5	-44.1	10
		M22	m8	20.0	340.0	54.0	260.3	39.0	-38.6	10

NGDC # = NGDC archive number, ID = survey ID in NGDC archive; Anomaly = a chron number in which approximately an anomaly profile starts; Index = profile ID indicated on Figure 15; site lat = latitude of a middle point on a given magnetic profile segment; site lon = longitude of a middle point on a given magnetic profile segment; pole lat = paleo pole latitude; pole lon =paleo pole longitude; PI = paleo inclination of a given profile; PD = paleo declination of a given profile; slin = track line azimuth from north toward young direction of the lienation.

APPENDIX B

Appendix B. Standard deviations of Atlantic polarity model chron boundaries (in kilometer)

Chron	Age	Canary	std (km)	n	block(%)	Keathley	std(km)	n	block(%)
M0r	124.14	0.00	0.00	4	0.00	0.00	0.00	7	0.00
M1n	125.00	23.27	4.99	3	4.98	28.80	4.48	5	4.99
M1r	127.15	30.87	6.20	3	6.60	70.38	14.77	5	12.19
M3n	127.57	40.55	7.78	4	8.67	80.90	9.65	4	14.01
M3r	128.05	60.95	6.26	4	13.04	99.19	16.24	7	17.18
M4	129.80	77.10	9.72	4	16.49	131.30	17.79	5	22.74
M5r	130.84	119.77	15.54	3	25.62	146.30	9.79	4	25.33
void	131.42	136.75	23.47	4	29.25	175.38	13.76	5	30.37
M16n	141.83	222.83	8.09	4	47.66	269.86	17.85	5	46.73
M16r	143.20	236.23	8.17	4	50.53	283.18	18.95	4	49.03
M17n	143.72	245.93	7.73	3	52.60	299.54	23.37	5	51.87
M17r	143.97	250.05	9.63	4	53.48	301.75	22.03	4	52.25
M18n	145.21	261.10	6.58	4	55.85	329.48	20.35	4	57.05
M18r	145.61	269.73	14.68	4	57.69	334.72	24.18	5	57.96
M19n	146.00	283.58	11.61	4	60.65	339.84	24.38	5	58.85
M19r	146.82	291.88	14.57	4	62.43	356.52	26.42	5	61.74
M20n	147.50	297.68	13.16	4	63.67	369.18	28.07	4	63.93
M20r	147.90	310.98	13.00	4	66.51	374.15	24.84	4	64.79
M21n	148.54	326.53	16.33	4	69.84	386.68	25.74	4	66.96
M21r	148.98	342.78	34.61	4	73.32	402.40	27.86	4	69.68
M22n	149.37	356.00	36.42	4	76.14	411.90	27.57	4	71.32
M22r	151.44	388.68	42.46	4	83.13	456.37	25.75	3	79.02
M23n	151.68	401.70	36.36	4	85.92	477.98	25.94	5	82.77
M23r	152.24	421.68	33.50	4	90.19	506.36	31.54	5	87.68
M24n	152.61	431.73	33.78	3	92.34	529.74	28.99	5	91.73
M24r	152.83	443.38	33.17	4	94.83	546.43	32.76	4	94.62
M25n	153.81	451.40	34.16	4	96.55	551.15	24.69	4	95.44
M25r	154.08	467.53	28.80	4	100.00	577.50	26.26	5	100.00

Chron = chron identified in the north Atlantic M-anomalies, Age = ages of the polarity boundaries determined from the Pacific compilation block model, Canary = averaged locations of polarity boundaries in Canary lineation set in km. std (km) = standard deviation of the locations of polarity boundaries in km, n = number of profiles used to calculate the average and standard deviation, block (%) = normalized distance at each polarity boundary from M0r, Keathley = averaged locations of polarity boundaries in Keathley lination set in km.

APPENDIX C

Appendix C. Magnetic profiles and magnetization parameters (northwest Australia)

NGDC#	Cruise ID	Anomaly	Index	site lat	site lon	pole lat	pole lon	PI	PD	sli
23060036	ODP123	M0	NWA1	-15.0	108.0	51.7	330.3	-59.4	-33.1	190
01030204	V3308	M0	NWA2	-19.0	108.5	51.7	330.3	-62.5	-34.9	190
		M0	NWA3	-20.0	108	51.7	330.3	-62.9	-35.9	190
		M0	NWA4	-21.0	107.5	51.7	330.3	-63.3	-36.5	190
01030201	V3305	M0	NWA5	-22.0	107	51.7	330.3	-65.8	-37.3	190
02020079	A2093	M17	NWA6	-13.0	116.5	47.7	342.8	-57.6	-38.3	190
		M17	NWA7	-14.0	115.5	47.7	342.8	-57.8	-39.2	190

NGDC # = NGDC archive number, ID = survey ID in NGDC archive; Anomaly = a chron number in which approximately an anomaly profile starts; Index = profile ID indicated on Figure 15; site lat = latitude of a middle point on a given magnetic profile segment; site lon = longitude of a middle point on a given magnetic profile segment; pole lat = paleo pole latitude; pole lon =paleo pole longitude; PI = paleo inclination of a given profile; PD = paleo declination of a given profile; slin = track line azimuth from north toward young direction of the lienation.

APPENDIX D

Appendix D. Estimated intervals for recovered cores.

Interval (mbsf)	core	interval (mbsf)	core	interval (mbsf)	core
312.120	7R7-12R8	750.392	75R-76R X309	1085.563	134R
348.016	13R	759.505	77R	1085.677	134R
358.043	14R	763.757	78R	1089.291	135R
361.953	15R	767.184	78R-79R	1093.990	136R
364.439	16R	770.597	79R1-3	1094.940	137R
373.000	17R	776.673	80R	1104.440	138R
377.000	18R	784.085	80R-81R	1112.715	139R
386.989	19R1-20R1	785.103	81R-82R	1115.547	140R-141R
395.808	21R1	795.042	82R2	1118.760	142R1-2
397.576	21R1-2	800.285	83R1	1125.842	143R
404.162	22R1	801.961	83R2-84R1	1130.866	144R
406.784	22R2	809.579	85R	1136.355	145R
407.746	22R3-23R2	817.509	85R-86R	1140.249	146R1
417.927	24R	823.208	86R	1143.193	146R2-147R
421.413	25R	829.114	87R	1146.998	148R-149R
435.729	26R1-2	833.902	88R	1155.138	149R
439.000	26R2-29R1	847.659	89R	1158.969	150R
456.092	29R1-30R1	871.750	92R	1163.619	151R1
461.015	30R1	873.320	93R	1170.134	152R
472.445	31R2-32R1	878.641	94R	1173.025	153R
477.720	32R2-33R1	886.000	94R-95R	1178.981	154R
482.963	33R2-35R1	889.111	95R	1185.997	155R
488.000	35R1-36R1	890.089	96R	1188.453	156R
493.433	36R1-37R3	899.218	96R-97R	1194.648	156R-157R
503.544	37R3-38R1	901.468	98R	1196.167	158R
504.916	38R1-3	906.886	99R	1201.257	159R
507.954	39R1-2	912.398	100R	1208.412	160R-161R1
517.000	40R1	914.839	101R	1215.392	161R1-162R
524.548	41R1-3	923.542	102R	1217.485	163R
530.573	42R1-42R2	935.680	102R-103R	1223.380	164R
535.394	43R	943.925	103R-104R	1227.800	165R-166R1
543.910	44R	945.748	104R-105R	1235.316	166R2-167R2
549.885	45R	946.998	105R	1239.443	167R3-168R1
561.393	46R	949.787	106R	1243.281	168R2-169R
564.890	47R1	955.220	107R	1250.673	170R
570.781	47R2	961.026	108R	1256.769	172-173R X312
574.459	48R1	966.459	109R1	1261.437	174R
582.018	49R1-2	969.772	110R	1270.393	175R
587.921	49R2-50R1	975.680	111R	1278.448	176R-177R
595.891	51R	979.241	112R	1281.110	177R
605.048	52R	983.571	113R	1282.644	178R
609.170	53R	987.333	114R	1288.658	179R-180R
617.844	54R	992.964	115R	1301.099	181R
626.300	55R	995.253	115R-116R	1305.466	182R
635.287	56R	999.147	116R	1308.818	183R
644.489	57R1-57R2	1007.960	117R-118R	1314.023	184R-185R
649.003	57R2-57R4	1011.684	118R	1316.583	185R-187R
653.722	58R1	1012.889	119R	1327.061	188R

658.126	58R2-59R1	1015.538	120R	1332.377	189R-190R
659.841	59R1-4	1017.839	121R	1342.412	191R
668.469	60R1-2	1027.846	122R	1347.632	192R
689.439	61R-62R	1031.699	122R-123R	1353.464	193R-194R
698.418	63R	1036.160	123R-124R	1360.784	195R-196R
699.133	64R	1038.095	124R1	1369.514	197R-198R
705.139	65R	1038.910	125R	1371.000	202R-203R
709.289	66R	1045.248	125R-126R	1375.537	204R
714.375	67R	1046.881	126R	1382.000	205-206R
718.500	68R	1047.910	127R	1390.106	207R
723.117	69R	1058.070	128R	1393.000	208R-209R
729.310	70R	1061.369	129R	1398.691	211R-213R
731.588	70R-71R	1066.147	130R	1409.440	214R
738.164	72R	1072.822	130R-131R	1417.246	215R-216R
742.685	73R	1080.084	132R	1419.987	217R
749.447	74R	1080.333	133R		

Interval = top of an interval with logger's depth (mbsf). Core = corresponding cores that are relocated within the interval.

VITA

Name: Masako Tominaga

Address: 3146 TAMU, College Station, TX 77843-3146.

Email Address: masako.tominaga@gmail.com

Education: B.E., School of Science and Engineering, Waseda University, 2002
M.S., Department of Oceanography, Texas A&M University, 2005
Ph.D, Department of Oceanography, Texas A&M University, 2009